UNIVERSITÀ DELLA CALABRIA

UNIVERSITA' DELLA CALABRIA

Dipartimento di Fisica

Dottorato di Ricerca in

SCIENZE E TECNOLOGIE FISICHE, CHIMICHE E DEI MATERIALI

CICLO

XXIX

Dielectric and Resonant Gain Singularities in Multilayered Nanostructures

Settore Scientifico Disciplinare FIS/03 – FIS/07

Coordinatore: Ch.mo Prof. (Vincenzo Carbone)

Firma _Vincenzo Carbone_

Supervisore/Tutor: Ch.mo Prof. (Antonio De Luca)

Firma _Antonio de Luca_

Dottorando: Dott. (Vincenzo Caligiuri)

Firma _Vincenzo Caligiuri_

UNIVERSITÀ DELLA CALABRIA

UNIVERSITA' DELLA CALABRIA

Dipartimento di Fisica

Dottorato di Ricerca in

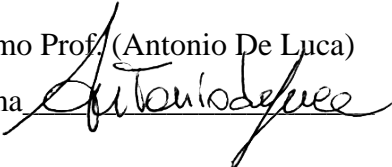SCIENZE E TECNOLOGIE FISICHE, CHIMICHE E DEI MATERIALI

CICLO

XXIX

Dielectric and Resonant Gain Singularities in Multilayered Nanostructures

Settore Scientifico Disciplinare FIS/03 – FIS/07

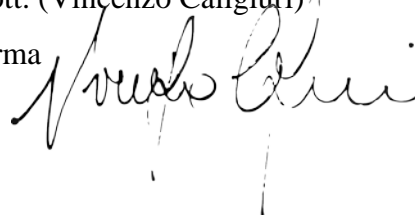**Coordinatore:** Ch.mo Prof. (Vincenzo Carbone)

Firma _____

Supervisore/Tutor: Ch.mo Prof. (Antonio De Luca)

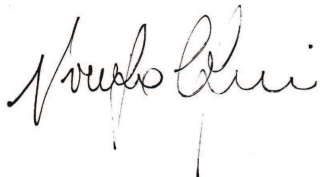Firma _____

Dottorando: Dott. (Vincenzo Caligiuri)

Firma _____

UNIVERSITÀ DELLA CALABRIA
DIPARTIMENTO DI
FISICA

UNIVERSITY OF CALABRIA

DOCTORAL THESIS

Dielectric and Resonant Gain Singularities in Multilayered Nanostructures

---

Author:

Vincenzo CALIGIURI

Supervisor:

Prof. Antonio DE LUCA

Dottorato in Scienze Fisiche, Chimiche e dei Materiali

February, 2017

Contents

iv

To Laszlo. Caught in the crossfire of childhood and stardom, blown on the steel breeze, flying lightly as three hay-bales over a field of daisies.

Dielectric and Resonant Gain Singularities in Multilayered Nanostructures

Abstract

In this thesis work, the dielectric and gain singularity regimes in *Hyperbolic Metamaterials* (HMM) have been conceived and both theoretically and experimentally studied. For the first one it has been demonstrated how, in order to induce a dielectric singularity in the dielectric permittivities of an HMM specific conditions on both the geometry and optical properties of the fundamental metal/dielectric components have to be fulfilled. An HMM respecting these constrains is named *Epsilon-Near-Zero-and-Pole* (ε_{NZP}). Such a system manifests both the so-called *Type I* and *Type II* within the visible range and, noticeably, allows to cancel the usually found effective dielectric (or metallic) frequency gap betwen them, showing a inversion point of these two coexisting anisotropies, called *Canalization Wavelength* or *Transition Wavelength*. It has been demonstrated how a light wave propagating inside the ε_{NZP} HMM, remains perfectly subwavelength collimated, proceeding as a straight soliton for more than 100 Rayleigh lengths. Many fascinating new properties are unlocked in such regime, among which the supercollimation and the perfect lensing have been theoretically studied as well as experimentally demonstrated. Due to the specific stringent conditions to be respected, it has been demonstrated that with a classic two-component HMM it is not possible to tune the ε_{NZP} wavelength and a

new configuration has to be adopted based on three components: a high index dielectric, a low index dielectric and a metal. By means of this new configuration, a full visible range design range of the ε_{NZP} wavelength has been demonstrated, keeping the same three fundamental materials and only acting on their thickness. The possibility of introducing thermal tunability of the optical features of a classic HMM has been demonstrated, thus overcoming the well known lack of tunability such structures usually are affected by. Basing on a sol-gel TiO_2 matrix, a new material has been conceived, embedding a low index dielectric (Polyvinylpyrrolidone, PVP) and an organic fluorescent medium (Coumarin C500). It has been found that the unsintered sol-gel TiO_2 remains extremely sensitive to any temperature change, endowing the HMM embedding such new mixture with thermally tunable features. The possibility to thermally reversibly reconfigure the most significant properties of an HMM embedding such a new dielectric has been both theoretically and experimentally demonstrated as well those one of a complete reconfiguration of the system, irreversibly switching from an effective metal to an effective dielectric, when exposed to high temperatures. In the end, it has been possible to theorize and study a new propagation regime called *Resonant Gain*, occurring in specifically modified ε_{NZP} HMMs. In order the resonant gain singularity to occur in the perpendicular dielectric permittivity of the ε_{NZP} HMM, a fluorescent medium has to embedded in the dielectric layers. Conditions to fulfil are very stringent but, once reached, it has been demonstrated that light propagating in such a regime is extremely subwavelength confined and amplificated inside the HMM, giving rise to a self-amplifying perfect lens and leading this system to configure as a promising candidate for LASER effect at the nanoscale. The same phenomenon has been verified in the framework of newly conceived system consisting in dye embedding metal/dielectric multishell nanoparticle, configuring as promising candidates for SPASER effect.

Sintesi

Sintesi del lavoro di tesi

Il lavoro di tesi dal titolo *"Dielectric and Resonant Gain Singularities in Multi-layered Nanostructures"* è consistito nella progettazione, simulazione e realizzazione di particolari strutture anisotrope con periodicità monodimensionale consistenti in multistrati nanometrici alternanti film sottili ($\approx 20nm$) di metallo e film sottili ($\approx 20nm$) di un mezzo dielettrico. Mostrando proprietà non presenti in natura, e comunque differenti da quelle dei singoli componenti, le strutture oggetto della tesi rientrano nel campo dei cosiddetti Metamateriali. Data la loro specifica relazione di dispersione, più in particolare si configurano come Metamateriali Iperbolici (MMI). La prima parte del lavoro ha visto la progettazione di particolari MMI, la cui anisotropia estrema va incontro a un punto di singolarità e inversione ad una precisa lunghezza dŠonda detta di "canalizzazione" o di "transizione". Sono state verificate sperimentalmente e simulate alcune fra le più notevoli proprietà tipiche di questo regime (ribattezzato *"Epsilon Near Zero and Pole"* ε_{NZP}), tra cui la possibilità di raggiungere confinamento ottico su scala molto inferiore alla lunghezza d'onda di interesse, nano-waveguiding, super-risoluzione e funzionamento del MMI come lente perfetta. In seguito è stato progettato un MMI di nuova concezione, basato su tre componenti fondamentali (metallo, dielettrico a basso indice di rifrazione e dielettrico ad alto indice di rifrazione) per colmare la mancanza di possibilità di scelta della lunghezza dŠonda di canalizzazione dei classici MMI. In questo modo è stato dimostrato come sia possibile progettare strutture ε_{NZP} con possibilità di scelta della lunghezza dŠonda di canalizzazione in tutto il range del visibile. La mancanza di tunabilità delle caratteristiche salienti di queste strutture è stata superata introducendo un mezzo dielettrico

progettato ad hoc. Basandosi su una matrice di titania non sinterizzata e ottenuta per deposizione sol-gel, sono stati aggiunti due componenti fondamentali: un dielettrico a basso indice (polivinilpirrolidone, PVP) e un mezzo organico fluorescente (Cumarina C500). Il primo permette di accordare finemente lŠindice di rifrazione della mistura, abbassandolo in funzione della sua concentrazione e favorendo, al contempo, lŠinglobamento del mezzo fluorescente, il quale fornisce al nuovo dielettrico (e chiaramente a tutto il MMI su di esso basato) significative proprietà fotoemissive. Il dielettrico così ottenuto, risulta tunabile in temperatura grazie allŠelevata sensibilità della titania ottenuta per sol-gel e mostra notevoli proprietà fotofisiche. Il suo inglobamento nel MMI completo ne garantisce la tunabilità in temperatura e conferma la capacità del MMI di velocizzare il rate di decadimento dei fluorofori contenuti nel mezzo di guadagno grazie al suo intrinsecamente elevato effetto Purcell. Il MMI così realizzato permette di accordare con un margine di 10 nm le sue caratteristiche peculiari, tra cui la cosiddetta lunghezza dŠonda "Epsilon Near Zero", alla quale la luce si propaga nel mezzo senza alcuna alterazione di fase, indipendentemente dalla sua forma. La possibilità di riconfigurare completamente il MMI, passando da un mezzo effettivamente metallico ad un altro effettivamente dielettrico, irreversibilmente, è stata dimostrata per temperature sensibilmente più alte di quelle tipicamente operative. Infine è stato possibile teorizzare e studiare un regime di propagazione completamente nuovo, ribattezzato "Resonant Gain Epsilon Near Zero and Pole" (RG-ε_{NZP}). Al fine di raggiungere tale condizione, è necessario non solo rispettare la propedeutica condizione Epsilon Near Zero and Pole precedentemente descritta, ma anche inglobare nel MMI un mezzo di guadagno le cui proprietà e concentrazione devono essere finemente progettate così da generare un comportamento risonante nel MMI. Si è dimostrato come, in questo regime, una singolarità nella parte immaginaria della permittività dielettrica inerente allŠasse ottico del MMI è generata, grazie alla quale la luce si propaga nel MMI come un solitone confinato alla nanoscala nel bulk della struttura. La luce risulta grandemente amplificata così come lŠeffetto di super-risoluzione estremamente migliorato. Per tali ragioni, il MMI

in regime RG-ε_{NZP} costituisce un ottimo candidato per fenomeni LASER intrinse-camente supercollimati. Il medesimo fenomeno è stato studiato anche in sistemi di nanoparticelle multishell metallo/dielettrico che, per gli stessi motivi, possono essere considerate ottime candidate per fenomeni SPASER.

Chapter 1

Introduction

Metamaterials are a class of artificial materials having structural parameters much smaller than the operative wavelength, being usually nanostructured for optical frequencies. Nonetheless, their effective response to ligth waves shows extraordinary and fascinating properties. Many promising physical behaviors can arise from materials with such unusual electromagnetic response, among which negative refraction, optical cloacking, super resolution imaging, ultra compact optical circuits, plasmonic nanolasers, inversion of the Cherenkov radiation are only few examples.[1, 2, 3, 4, 5, 6, 7, 8, 9, 10, 11, 12, 13, 14, 15] Recently, a new branch of the metamaterial class is receiving an increasing attention in the scientific panorama, which holds an ultra anisotropic behavior not yet found in nature for optical frequencies. The so-called "*Hyperbolic Metamaterials*" (HMMs), are nanostrucutred materials whose XY dielectric permittivity (the one parallel to the HMM surface that, in this manuscript, will be called $\varepsilon_{\parallel}$) is opposite in sign to the Z one (those one perpendicular to the HMM surface that, from hereafter, will be called $\varepsilon_{\perp}$). Such prerequisites identify a so-called "hyperbolic dispersion" (a concept that will be explained in chapter 2) and to which HMMs due their name. In order to ensure a hyperbolic dispersion in the visible frequency range, a metallic fundamental component is necessary, as well as a dielectric one. They can be arranged in two main geometries in order to reach a hyperbolic dispersion. The so-called "*type II*" anisotropy, in which $\varepsilon_{\parallel} < 0$ and $\varepsilon_{\perp} > 0$ is usually found in subwavelength metal/dielectric multilayers while the opposite case known as "*type I*", in which $\varepsilon_{\parallel} > 0$ and $\varepsilon_{\perp} < 0$ is usually present in HMMs made of

metallic nanowires immersed in a dielectric host. The coexistence of the two inverse anisotropies in the same HMM is a common fact but, usually, the two anisotropies are separated by broad effective dielectric gaps (frequency ranges in which $\varepsilon_\parallel \neq \varepsilon_\perp$ but they are both positive) of effective metallic gaps (frequency ranges in which $\varepsilon_\parallel \neq \varepsilon_\perp$ but they are both negative).

Reducing (and eventually cancelling) these dielectric or metallic gaps at a precise wavelength (called *Transition Wavelength*) represents an experimental challenge.

In chapter 3, the design, fabrication and characterization of an epsilon near zero and pole (ε_{NZP}) multilayer HMM, showing simultaneously $\varepsilon_\parallel \approx 0$ and $\varepsilon_\perp \approx \infty$ within the visible range is reported. The system is able to overcome all of the above mentioned challenges. The realized structure, due to the careful choice of its fundamental building blocks, manifests a type I behavior covering about 90nm range until the transition wavelength (414nm) at which the extreme anisotropy completely reverses, passing to a more common type II HMM. Experimental demonstrations of the most important behaviors of such a metamaterial are investigated as well. An ellipsometric analysis reveals that, at the transition wavelength between type I and type II, a dielectric singularity called ε-Near-Zero-and-Pole (ε_{NZP}) in the optical constants occurs and the material undergoes a dramatic phase change, which opens the way to fascinating physical phenomena. Indeed, in order to show the potential of the presented configuration, the supercollimation effect at the type I/type II transition wavelength is verified by means of a confocal microscopy study. It is also demonstrated the possibility to exploit this effect to realize an ultra-subwavelength waveguide in the metamaterial bulk, being able to keep the light beam extremely confined inside the structure for more than 100 Rayleigh lengths. As an application, a near field perfect lens based on the supercollimation effect is designed by means of numerical simulations corroborated by an experimental proof of concept of the phenomenon.

Unfortunately, once the materials are selected, there is no way to move the transition (canalization) wavelength by keeping the same components, thus limiting both the design process and the possibility to actively interact with the HMM (*e.g.* tune

its optical properties and/or induce light emission with specific characteristics). In Chapter 4 it will be shown how to overcome the design limitations for the ε_{NZP} condition and open a whole visible wide design window for the ε_{NZP} condition by introducing a HMM based on a building block made by three different materials, without the need to change them and just by carefully engineering their fill fractions. Moreover, in Chapter 5, the possibility to endow the HMM with a reversible thermally tunable response. Such a property is ensured by the adoption of a specifically designed dielectric layer, embedded in the HMM as the constitutive dielectric, made of a high index semiconductor, a low index polymer and a fluorescent dye. By using such a new medium and thanks to the specific HMM configuration, an overall increasing of the decay rate of a fluorophore embedded inside the constitutive dielectric layer is reached as well. The possibility of irreversibly reconfigure the HMM is demonstrated as well, opening the way to cheap, anti-counterfeit nano-tags.

In the end, it is demonstrated in Chapter 6 how the ε_{NZP} singularity can be reached also with respect to the imaginary parts of Equation 2.8 and 2.9, a condition called *Resonant Gain* ε_{NZP} HMM (RG-ε_{NZP} HMM). By means of appropriate simulations, it is demonstrated how, within such a regime, The RG-ε_{NZP} HMM becomes a promising candidate for self collimated nano-lasers and self amplifying perfect lenses.

Chapter 2

Effective Medium Theory based Modeling of HMM optical behaviour

As described in the introduction, HMMs are characterized by a uniaxial hyperbolic dispersion determined by their effective dielectric tensor $\bar{\bar{\varepsilon}} = [\varepsilon_{xx}, \varepsilon_{yy}, \varepsilon_{zz}]$. Considered as the ultra-anisotropic limit of traditional uniaxial crystals,[16] they possess one of the principal components of their permittivity tensor that is opposite in sign to the other two; in particular the in-plane isotropic components are $\varepsilon_{xx} = \varepsilon_{yy} = \varepsilon_{\parallel}$, the out of plane component is $\varepsilon_{zz} = \varepsilon_{\perp}$ and $\varepsilon_{\parallel} \neq \varepsilon_{\perp}$. This means that the same material can interact with the radiation behaving as a metal or as a dielectric depending on the orientation of the radiation wavevector $\vec{k} = [k_x, k_y, k_z]$. HMMs unique properties result from the isofrequency surface of an extraordinary wave (TM polarized) propagating into the structure; in this case the dispersion relation can be easily recovered starting from Maxwell's equations in the harmonic frequency domain:

$$\vec{k} \times \vec{E} = \omega\mu_0\vec{H} \tag{2.1}$$

$$\vec{k} \times \vec{H} = -\omega\varepsilon\vec{E} \tag{2.2}$$

applying $\vec{k}\times$ to the first equation:

$$\vec{k} \times \vec{k} \times \vec{E} = \omega\mu_0\vec{k} \times \vec{H} \tag{2.3}$$

$$\vec{k} \times \vec{k} \times \vec{E} - k_0^2 \leftrightarrow \varepsilon \vec{E} = 0 \qquad (2.4)$$

This can be expressed in a matrix form as follows:

$$
\begin{bmatrix}
\varepsilon_{xx}k_0^2 - (k_y^2 + k_z^2) & k_x k_y & k_x k_z \\
k_x k_y & \varepsilon_{yy}k_0^2 - (k_x^2 + k_z^2) & k_y k_x \\
k_x k_z & k_y k_z & \varepsilon_{zz}k_0^2 - (k_x^2 + k_y^2)
\end{bmatrix}
\begin{bmatrix}
\vec{E}_x \\
\vec{E}_y \\
\vec{E}z
\end{bmatrix}
= 0
$$

As said before, the HMMs uniaxial nature imposes $\varepsilon_{xx} = \varepsilon_{yy} = \varepsilon_{\parallel}$ and $\varepsilon_{zz} = \varepsilon_{\perp}$. Solving the matrix by imposing the aforementioned identities, it follows that:

$$\frac{(k_x^2 + k_y^2)}{\varepsilon_{\perp}} + \frac{k_z^2}{\varepsilon_{\parallel}} = (\frac{\omega}{c})^2 \qquad (2.5)$$

Equation 2.5 is the dispersion relation for a general uniaxial crystal. Therefore HMMs represent one of the most promising way to practically engineer bulk devices with the desired anisotropy. By properly managing the constitutive parameters, $\varepsilon_{\parallel}$ and $\varepsilon_{\perp}$ can become either positive or negative, opening the way to a wide design flexibility. The anisotropy of the HMM depends, in general, on the sign of the product $\varepsilon_{\parallel} \cdot \varepsilon_{\perp}$, that can be > 0 or, more interestingly, < 0. In the latter case two scenarios can occur: (i) *type I* - HMM and (ii) *type II* - HMM. In the case of *type I* - HMM ($\varepsilon_{\parallel} > 0$ and $\varepsilon_{\perp} < 0$), the stack behaves as a dielectric in the *xy* plane and as a metal in the *z* direction and the isofrequency surfaces deriving from Equation 2.5 assume the shape of an open bounded hyperboloid. The behavior is completely reversed in the case of *type II*-HMM, where the isofrequency surface becomes a continuous hyperboloid. The two inverse anisotropic regions are generally separated by an effective dielectric or metallic gap region. Two geometries have been found to show the aforementioned properties: the first one is a nanometric metal/dielectric stack, usually showing the type II anisotropy in the visible range, while the second one, usually showing the type I anisotropy in the visible range, consists of an ordered array of metallic nano-wires, immersed in a dielectric host.
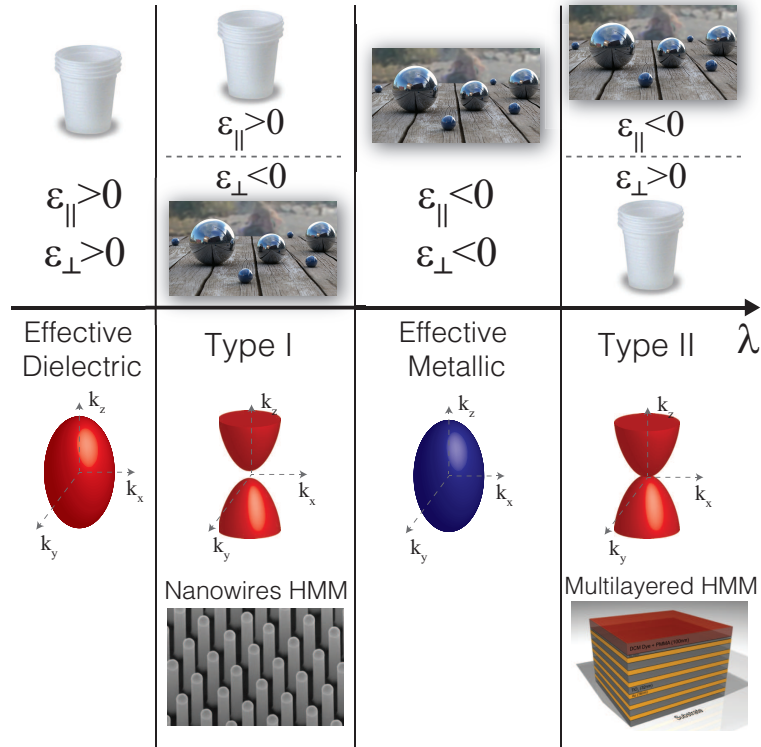
FIGURE 2.1: All of the possible anisotropies in a metal/dielectric multilayer, together with each respective dispersion relation. All of the anisotropies have placed as a function of the wavelength in the order in which they usually occur in a multilayered HMM.

Referring to the multilayered HMM, if the size of the constitutive unitary cell (a single metal/dielectric bilayer) is designed to be deeply subwavelength and the total number of bilayers is high enough, then the complex optical constants of the overall effective HMM can be approximated by the well accepted Effective Medium Theory (EMT), as shown in equation 2.6 and 2.7.

$$\tilde{\varepsilon}_{\parallel} = \frac{t_m \tilde{\varepsilon}_m + t_d \tilde{\varepsilon}_d}{t_d + t_m} \tag{2.6}$$

$$\tilde{\varepsilon}_{\perp} = \frac{\tilde{\varepsilon}_m \tilde{\varepsilon}_d (t_d + t_m)}{t_d \tilde{\varepsilon}_m + t_m \tilde{\varepsilon}_d} \tag{2.7}$$

Here subscripts *m* and *d* refer to the metal and dielectric layers, respectively. In the case losses cannot be neglected, the explicit form of equations 2.6 and 2.7 have to be considered (see equations 2.8 and 2.9), in which the real and imaginary parts of the overall optical constants are considered:

$$\tilde{\varepsilon}_{\parallel} = \frac{\varepsilon_d' t_d + \varepsilon_m' t_m + i(\varepsilon_d'' t_d + \varepsilon_m'' t_m)}{t_d + t_m} \tag{2.8}$$

$$\tilde{\varepsilon}_{\perp} = \frac{\varepsilon_m' t_m D + \varepsilon_d' t_d M + i\left(\varepsilon_m'' t_m D + \varepsilon_d'' t_d M\right)}{(\varepsilon_d' t_m + \varepsilon_m' t_d)^2 + (\varepsilon_d'' t_m + \varepsilon_m'' t_d)^2}(t_d + t_m) \tag{2.9}$$

Here superscripts prime and double-prime refer to real and imaginary parts of $\tilde{\varepsilon}_m$ and $\tilde{\varepsilon}_d$, while t_d and t_m are their thicknesses, respectively, whereas $D = (\varepsilon_d')^2 + (\varepsilon_d'')^2$ and $M = (\varepsilon_m')^2 + (\varepsilon_m'')^2$.

Chapter 3

Dielectric Singularity in Hyperbolic Metamaterials: the inversion point of coexisting anisotropies

3.1 The ε Near zero and Pole condition

One of the strengths of HMMs lies in their extremely easiness of design. As expressed before, in the case of multilayered HMMs, if deeply subwavelength building blocks (metal/dielectric thin layers) are selected, the overall optical response of the HMM can be modelled with acceptable precision in the framework of the effective medium theory. Due to the particular geometrical 1D arrangement, an optical anisotropy arises with the optical axis oriented parallel to the bulk of the structure. The two dielectric permittivities manifested by the structure are expressed in Equation 2.8 and 2.9. As it is well known, multilayer stacks show a *type II* behavior only, and it is needed a metallic nanowire array immersed in a dielectric host to obtain a *type I* behavior, anyway, it is clear that Equation 2.8 can manifest a zero while Equation 2.9 a pole. If singularly taken, these two conditions are of great interest. In the former case, the occurring of a zero in the parallel dielectric permittivity determines a so called *effective dielectric/type II* transition. At the ε near zero wavelength, the HMM manifests the typical properties of a so called ε near-zero medium (ε_{NZ}).

As a consequence, it follows that the second Maxwell equation $\nabla \times \vec{H}$ is equal to zero, bringing to a curl-free magnetic field. The phase variation of a plane wave propagating through an arbitrary shaped ε_{NZ} is nearby zero [17]. This means that, independently on the geometric shape of the ε_{NZ} path, the components of a plane wave propagating through it arrive perfectly preserved at the exit interface, opening to the possibility to realize non-distorting optical connections of arbitrary shapes. In the second case, ε assumes enormously high absolute values, determining the so called ε Near Pole (ε_{NP}) condition. When this occurs, the HMM usually undergoes an *effective dielectric/type I* transition. Among the other properties, it has been demonstrated that such a condition can open to ultra-subwavelength imaging. In this chapter it will be demonstrated that HMMs can manifest a zero in $\varepsilon_{\parallel}$ and a pole in $\varepsilon_{\perp}$, simultaneously.

Recently, Shekhar et. al. theoretically reported a multilayer system presenting both the anisotropies, either separated by a dielectric gap or adjacent each other, showing that an experimental result with a simultaneous type I/type II behavior at the same frequency in the visible range would be not easy to achieve.[18] In the same work, an Ag/TiO_2 multilayer is theoretically investigated as a structure able to eliminate the dielectric gap between the type I and type II regions, enabling novel phenomena and applications. Anyway the amorphous phase of a real layer of TiO_2 possesses optical constants drastically lower than in the birefringent phase, thus pushing the experimental transition wavelength deep in the UV and limiting the possibility of an effective implementation of such a structure in the experimental framework. A similar behavior has been observed even in the field of semiconductors. Hoffman et. al.[19] realized a semiconductor multilayer working at the transition wavelength of typeI/type II in the microwave range, while Silveirinha et. al.[20] found a comparable mechanism governing the propagation of electron waves inside a semiconductor hypergrating. In that case the coexistence of ultra-anisotropies is referred to the overall effective mass of electrons instead of the homogenized optical constants of the metastructure.

Here, the design, fabrication and characterization of an epsilon near zero and pole (ε_{NZP}) multilayer HMM is reported, showing simultaneously $\varepsilon_{\parallel} \approx 0$ and $\varepsilon_{\perp} \approx \infty$ within the visible range, able to overcome all of the above mentioned challenges. The realized structure, due to the careful choice of its fundamental building blocks, manifests a type I behavior covering about 90nm range until a wavelength at which the extreme anisotropy completely reverses (414nm), giving rise to a more common type II HMM. The experimental demonstrations of the most important behaviors of such a metamaterial are carried out as well. An ellipsometric analysis reveals that, at the transition wavelength between type I and type II, a dielectric singularity in the optical constants occurs and the material undergoes a dramatic phase change, which opens the way to fascinating physical phenomena. Indeed, in order to show the potential of the presented configuration, we experimentally study the supercollimation effect at the type I/type II transition wavelength by means of a confocal microscopy study. We demonstrate the possibility to harness this effect by realizing an ultra-subwavelength waveguide in the metamaterial bulk, being able to keep the light beam extremely confined inside the structure for more than 100 Rayleigh lengths. We further demonstrate the near field perfect lens behavior by means of numerical simulations corroborated by an experimental proof of concept of the proposed phenomenon.

For a multilayer structure, the effective dielectric permittivities are complex quantities and, in order to evaluate their complete expressions, we refer to an extended Effective Medium Theory (EMT). This permits to include the imaginary parts of the permittivities of the main HMM building blocks.

In this case, the simultaneous ε_{NZP} condition occurs when the numerator in Eq. 2.6 and denominator in Eq. 2.7 result simultaneously zero. The constrains to be fulfilled can be find by solving the following system:

$$\begin{cases} t_d = t_m \\ \varepsilon_d = -\varepsilon_m \end{cases} \tag{3.1}$$

These conditions can be achieved by selecting materials whose dielectric permittivity values are equal but opposite in sign for a given frequency. Apparently, this condition is verified for many metal-dielectric pairs, nevertheless when losses are included in the analysis, satisfying this condition becomes challenging. Due to its high losses, gold has to be excluded and, in order to move the desired condition within the visible range, a high index dielectric has to be chosen, thus excluding the most commons SiO_2 and Al_2O_3. Also TiO_2 cannot represent a valid alternative, even though this material has been theoretically proposed as a good candidate due to its high index [18]. This because the widely used Palik optical constants for TiO_2 in its birefringent form, greatly decrease after real deposition processes (thermal, sputtering, etc.) from amorphous target or pellets. Then as metal we selected silver because of its low losses at visible frequencies, whereas ITO (Indium Tin Oxide) constitutes an interesting alternative to a common dielectric, due to its wide utilization in everyday technology, fabrication processes and transparency in most of the visible range and suitably high refractive index. For all these reasons, ITO/Ag pair constitutes the selected fundamental bilayer.

3.2 Fabrication of the Epsilon Near Zero and Pole HMM

As a first step, 20 nm thick layers of ITO and Ag have been alternatively deposited on a glass substrate up to 5 bilayers, by means of a DC Magnetron technique (see methods). The optical constants of each layer have been separately evaluated by means of spectroscopic ellipsometry and results have been used in the EMT calculations (see Fig. 3.1**b**) for a precise simulation of the final metamaterial behavior including optical losses.
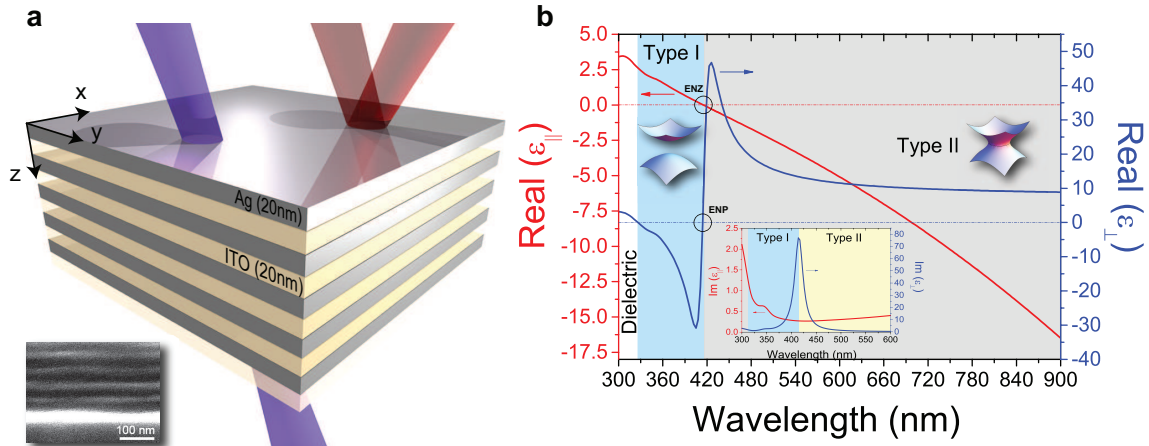
FIGURE 3.1: **a** Sketch of the obtained HMM structure made of 5 bilayers of Ag (20nm) and ITO (20nm). The two laser beams in the sketch represent the different behavior of the obtained material, that is almost trasparent in the UV range, whereas is reflective above 450nm. Inset is a SEM image of the transversal section of the obtained sample. **b** Effective Medium Theory (EMT) of an ITO/Ag multilayer. Real part of epsilon parallel (red curve) and epsilon perpendicular (blue) of the entire structure. In the inset we present the imaginary parts of parallel and perpendicular permittivities. It is evident that the type I/type II transition wavelength occurs at 414nm.

As shown in Fig. 3.1**b**, the medium behaves as a dielectric up to 327 nm because both $\varepsilon_{\parallel}$ and $\varepsilon_{\perp}$ are positive. Between 327 nm and 414 nm, $\varepsilon_{\parallel} > 0$ while $\varepsilon_{\perp} < 0$, opening a *type I* - HMM window. At $\lambda = 414$nm the ε_{NZP} behavior clearly manifests a strong discontinuity in $\varepsilon_{\perp}$, passing from a very high negative value (virtually $-\infty$) to a very high positive one (virtually $+\infty$) while, simultaneously, $\varepsilon_{\parallel} = 0$. In the inset of Fig. 3.1**b**, the imaginary parts of $\varepsilon_{\parallel}$ and $\varepsilon_{\perp}$ are plotted, showing a very sharp Lorentzian shape for $\varepsilon_{\perp}$, peaked exactly at the transition wavelength. HMM exhibits a *type II* behavior at $\lambda > 414$nm. A Scanning Electron Microscopy (SEM) image (inset of Fig. 3.1**a**) shows the obtained layer by layer disposition with a fill fraction of almost 50%.

3.3 Brewster Angle

Moreover, we have investigated the presence of the "pseudo-Brewster angle"[21] for two incident wavelengths such as 341 nm (in the middle of the *type I* region) and 750

nm (*type II* region), both for *s−* and *p−* polarization. A clear signature of the *type I* behavior is due to the presence of a pseudo-Brewster angle,[18] while the highly metallic response of the device makes it impossible for the reflectance at any angle to reach values close to zero in the *type II* region. Pseudo-Brewster angle has been theoretically calculated by using a scattering matrix method (SMM) analysis and then the results have been compared with experimental curves obtained by means of variable angle spectroscopic ellipsometry (see Fig. 3.2).
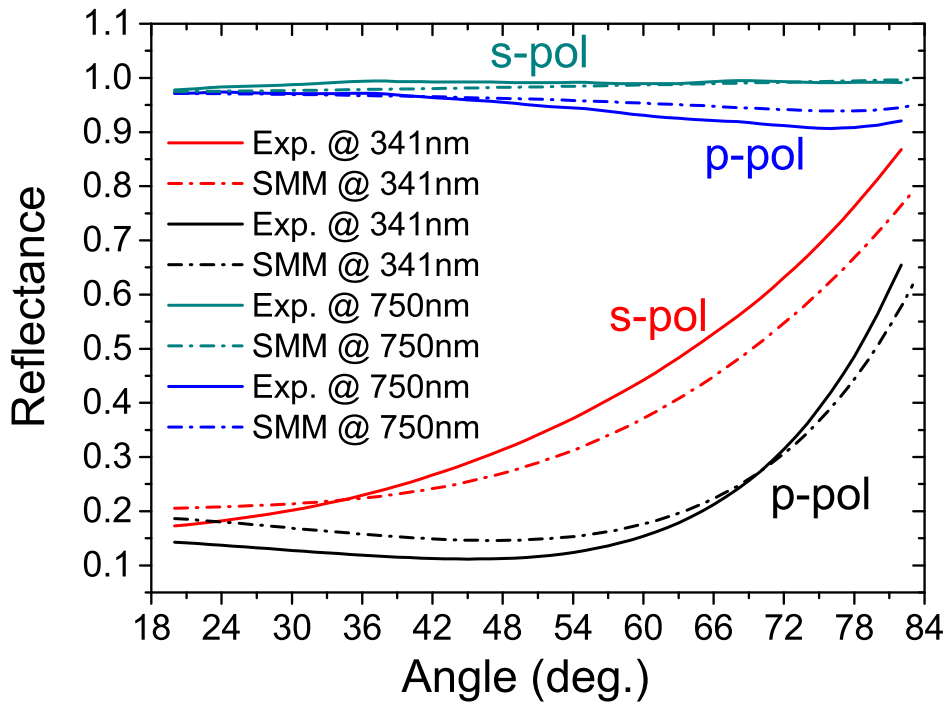
FIGURE 3.2: Experimental (solid) and Theoretical (SMM, dash-dot) pseudo-Brewster angle for *s−* and *p−* polarization at two different wavelengths (type I and type II regions). In type II region (at 750nm), a metallic behavior in *x, y* directions causes both the *s − pol* and *p − pol* to be completely reflected. In type I region (at 341 nm), the behavior is reversed: a dielectric response with low losses in *x, y* directions allows the appearance of a Preudo-Brewster angle for p-polarized lightwave, as expected.

Numerical simulation results (dash-dot curves) are found to be in a very good agreement with experimental results (solid curves). For 341 nm, a pseudo-Brewster

angle is clearly visible around 46 degrees for $p-$polarization, while the pseudo-Brewster angle is neither detected nor predicted for $s-$polarization. For 750 nm, reflectance remains extremely high (above 90%) at any angle, for both the polarizations, confirming the high metallic response of the multilayer structure in the *xy* plane.

3.4 Transmission and Reflection

As predicted by Shekhar et al.,[18] *type I* - HMMs are more transmissive than *type II*. Indeed, a high transmission window is expected in *type I* region, while high reflectance in *type II*. Theoretical transmission and reflectance behaviors have been calculated by means of a classic Transfer Matrix Method (TMM) and Scattering Matrix Method (SMM) analysis. In order to verify the expected behavior, we performed transmission and reflection measurements by using a V-VASE (J. A. Woollam) spectroscopic ellipsometer. Acquired transmission and reflectance spectra (both experiment and simulation) are shown in Fig. 3.3**a** and 3.3**b**, respectively. Transmission has been acquired at two different angles, just below and above the observed pseudo-Brewster angle. For both angles (40 and 50 degrees), a highly transmissive window is clearly visible throughout *type I* region, as predicted by theory. Reflectance has been measured ellipsometrically at two different angles, far below ($25°$) and close to ($55°$) the pseudo-Brewster angle, for both $p-$ and $s-$ polarizations, confirming the low reflectivity of *type I* region in contrast with the high reflectance measured in *type II*. It is worth noting the accordance between simulations and experiments. In the inset of Fig. 3.3**a** we report an experiment for the potential application of the metamaterial as a HMM-based selective filter. This application crucially improved our confocal setup while conducting the supercollimation experiment.

Following the experiments proposed by Hoffman et. al.,[19] we investigated the *dielectric/type I* transition by analyzing the reflection spectrum of both s- and p-polarized plane waves (Fig. 3.3**b**). As expected, for an s-polarized impinging light

wave, no dip is detected in reflection, while, for a p-polarized light wave, impinging at an angle close to the Brewster one, a dip close to zero is present at this wavelength. When moving away from the Brewster angle, this dip red shifts and, at the same time, moves far from zero, confirming the behaviour described by Hoffman et. al.[19] On the other hand, it is possible to detect the *dielectric/type I transition* even more accurately, by investigating the transmission spectrum as well (Fig. 3.3**a**). It is worth noting that the narrow dip present in transmission exactly at 327nm has to be attributed to the so-called *Ferrel-Berreman mode*[22]. Indeed, being a radiative mode, this dip does not shift in wavelength when changing the investigation angle. Furthermore, in reference [22] it is clarified how this mode appears in correspondence to an *epsilon near zero* medium. The realized system assumes this property exactly at the *dielectric/type I* transition wavelenght, at which $\varepsilon_\perp = 0$. This behaviour is also confirmed by the *Pseudo-Epsilon* measurement (see $\langle \varepsilon \rangle$ in equation 3.5), where the $\langle \varepsilon \rangle$ crosses zero exactly at this wavelength. This implies that the occurrence of the *Ferrel-Berreman mode* represents a clear signature of the *dielectric/type I* transition.
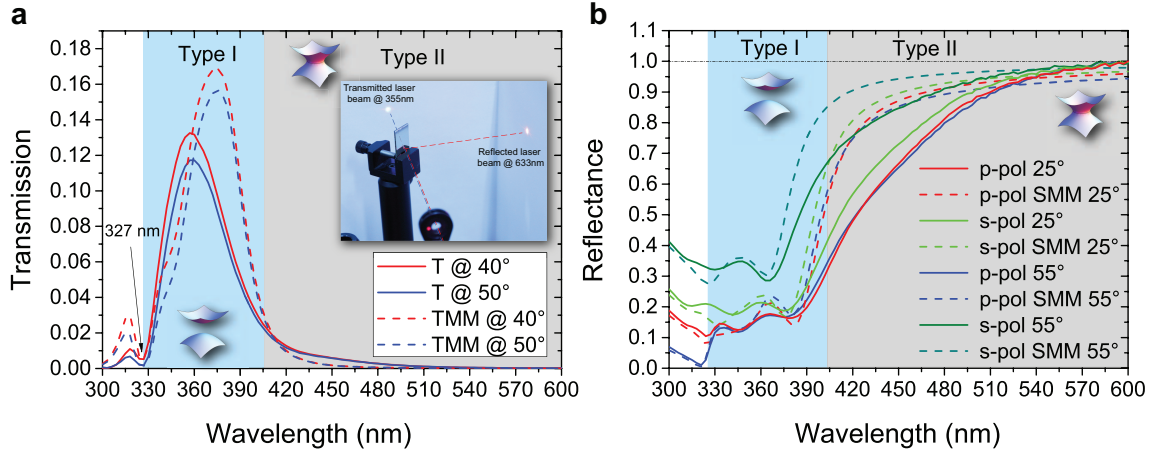
FIGURE 3.3: **a** Experimental (solid) and transmission simulation (using TMM - dashed) at two different incident angles (40 and 50 degrees). Inset represents the utilization of the obtained device as a HMM-based selective filter. It is well evident the high transmissive behavior in type I region (355*nm*) with respect the high reflectivity in type II region (633*nm*). The zero transmission dip, occurring exactly at 327nm, does not shift when changing the impinging angle, configuring this as a *Ferrel-Berreman mode*. As reported in [22] this dip is a characteristic of the *epsilon-near-zero* medium, for this it can be used as a signature of the *dielectric/type I* transition. **b** Reflectance curves for $s-$ and $p-$ polarization at angles 25 and 55 degrees (solid lines). Dashed curves have been calculated by means of the SMM model. The zero reflection dip occurring for a p-polarized lightwave at 55°, is a clear evidence of the $\varepsilon_{\perp} = 0$ condition [19], confirming the dielectric/type I transition.

3.5 Ellipsometry and Pseudo-Epsilon

Optical constants of realized thin films have been characterized by using spectroscopic ellipsometry. This analysis consists in the evaluation of the ratio $\rho = r_p/r_s$ between the p-polarized and the s-polarized waves reflected from a thin film, deposited on a known substrate. Starting from this measurement, it is possible to evaluate the ellipsometric angles Ψ and Δ by simply applying the well known relation $\rho = tan(\Psi)exp(i\Delta)$. The construction of an optical model for each deposited layer, and the consequent fit of the experimental data for Ψ and Δ, permits to extract the precise optical constants of the analysed layers.
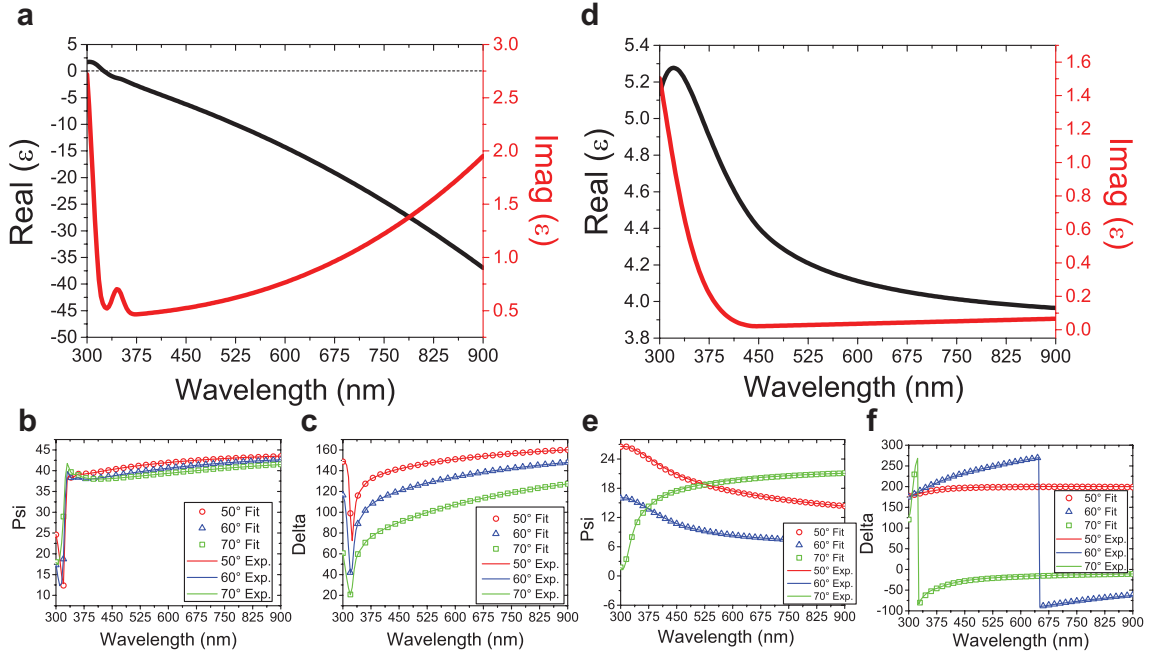
FIGURE 3.4: Real and Imaginay parts of optical costants for Ag and ITO. **a** and **d** represent the optical constants of Ag and ITO layers, respectively, found after a fit of the ellipsometrical angles Ψ and Δ reported in **b** and **c** for Ag, and **e** and **f** for ITO, respectively. The ellipsometrical angles Ψ and Δ measured (solid lines) and fitted (scattered data) for Ag and ITO layers are reported for three different incident angles, 50 (cirlces), 60 (triangles) and 70 (squares) degrees, respectively.

The optical constants obtained for each Ag and ITO layer of the HMM are shown in Fig. 3.4a and 3.4d, where the values of Ψ and Δ used to find them are reported in Fig. 3.4(b-c) and 3.4(e-f) for Ag and ITO, respectively. The best fit for thicknesses extracted from the optical model, as well as the optical constants, are used to perform an accurate EMT design of the entire HMM device. The ellipsometrical angles Ψ and Δ have been measured and fitted also for the final Ag/ITO multilayered HMM. Results are plotted in Fig. 3.5a.
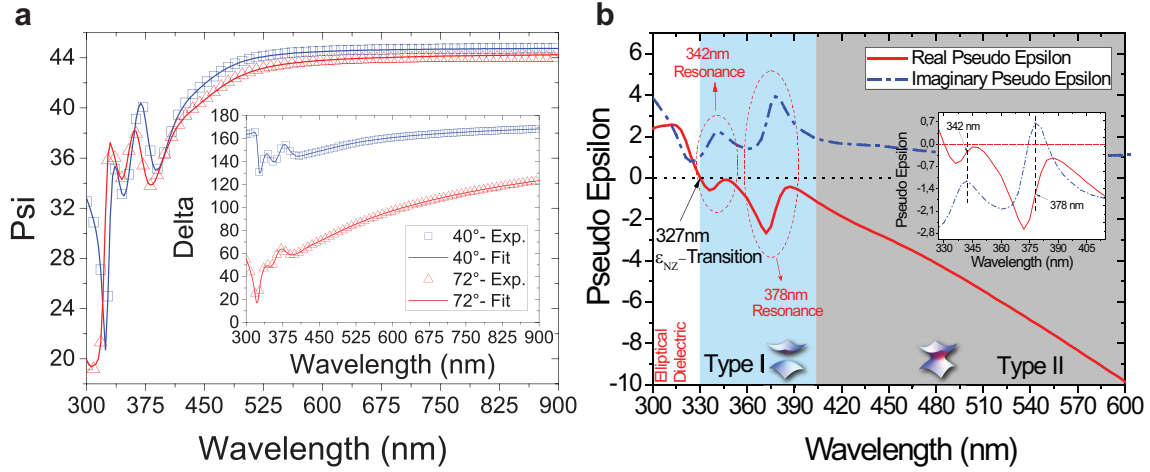
FIGURE 3.5: **a** Ellipsometrical constants Ψ and Δ measured (scattered data) and fitted (solid lines) of the whole hyperbolic metamaterial. It is worth noting the good accordance between measures and fitted data. **b** Pseudo Epsilon measured ellipsometrically for the final HMM.

This procedure gives us precious information upon the optical behaviour of the hyperbolic metamaterial. In particular the so called "*Pseudo Epsilon*" can be extracted. This quantity, strictly connected to $\varepsilon_\parallel$ and $\varepsilon_\perp$, is expressed as:

$$\langle \varepsilon \rangle = sin(\theta)^2 \left[1 + tan(\theta)^2 \left(\frac{1 - tan(\Psi)}{1 + tan(\Psi)} \right)^2 \right] \qquad (3.2)$$

Measured Pseudo Epsilon for the whole multilayer is reported in Fig. 3.5b. Many useful information can be extracted from this quantity. First of all, it becomes negative exactly at 327nm, confirming the transition from pure dielectric to Type I - HMM. Then, two resonances are clearly visible at $\lambda = 342nm$ and $\lambda = 378nm$, corresponding to two flexes in the real part of $\langle \varepsilon \rangle$, and two lorentzian shaped peaks in the imaginary part. It is worth noting that the maximum of transmission (obtained in the Type I region) occurs exactly in the middle of these two resonances.

3.6 Light Propagation Inside the Epsilon Near Zero and Pole HMM and Supercollimation

The optical properties of a general photonic structure can be described by means of its tensor Green function [23]. In its general form the Green function may present, in the hyperbolic frequency region, singularities responsible of many important properties of such materials, like diverging density of states and Purcell factor. Moreover, in both the two hyperbolic regions, Type I and II, the electric field propagates along a typical cone shaped pattern[24, 25, 26, 23, 27], respecting the condition $\varepsilon_\parallel sin^2(\theta) + \varepsilon_\perp cos^2(\theta) > 0$, where θ is the half angle between the two lobes of the resonance cone (θ_{RC}). The values θ_{RC} assumes in the proposed ε_{NPZ} HMM for the whole visible range can be calculated straightforwardly from the previous relation, as follows:

$$\theta_{RC} = atan\left(\sqrt{-\frac{Re(\varepsilon_\parallel)}{Re(\varepsilon_\perp)}}\right) \qquad (3.3)$$

and are plotted in Fig. 3.6. In particular, θ_{RC} becomes rapidly smaller, converging to zero exactly at the ε_{NZP} wavelength above which they start growing again, assuming the typical type-II values.
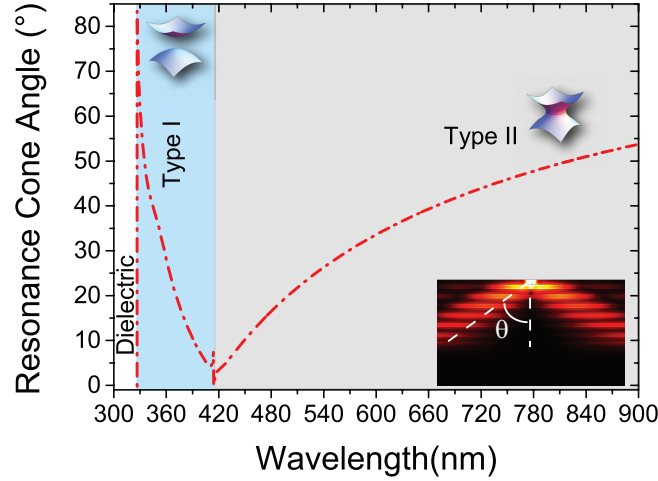
FIGURE 3.6: Resonance cones angle theta plotted versus wavelengths. Theta reaches zero exactly in the canalization region occurring at 414 nm. In the inset it is shown the electric field propagation coming from a vertical oriented electric point dipole source at 532nm (Type II region). Electric field inside the HMM splits into two well distinguishable lobes, forming the typical resonance cone pattern exactly at the calculated angle.
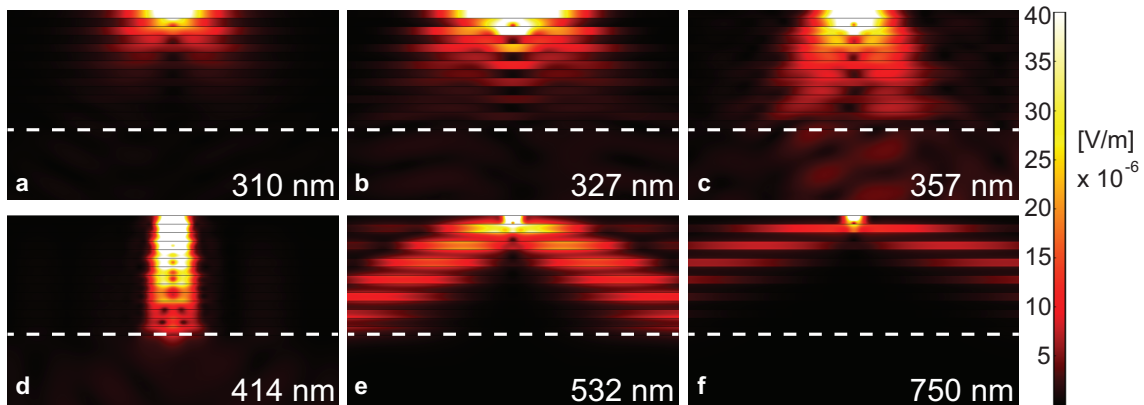
FIGURE 3.7: Electric Field propagation inside the HMM for different wavelengths. Simulations have been performed by means of a sophisticated Finite Element Method based code, considering a vertical oriented dipole positioned just at the top of the HMM. Excitations wavelengths lie respectively: **a** In the effective dielectric region. **b** At $\lambda = 327nm$ corresponding to the $\varepsilon_\parallel$ near zero condition. **c** In the type I region. **d** In the canalization regime. **e-f** Within the type II region.

In Fig. 3.7 (a-f) propagation of the electric field emitted by a vertically oriented point dipole inside the proposed ε_{NPZ} HMM is shown for all the characteristic wavelengths. In Fig. 3.7d the propagation of the electric field inside the HMM at the canalization regime is reported. From equation 3.3, it is clear that if $\varepsilon_\parallel \approx 0$, or

$\varepsilon_\perp \approx \infty$, then θ_{RC} is equal to zero and the wave propagates as a single straight beam, highly confined inside the structure (see Figure 3.7). This condition is known as *canalization regime*[24, 28, 29], and can bring to a supercollimation effect.

In order to verify the supercollimation properties of the presented HMM configuration, we performed confocal microscopy experiments. Acquired images at three different incident wavelengths, together with simulations, are reported in Fig. 3.8.
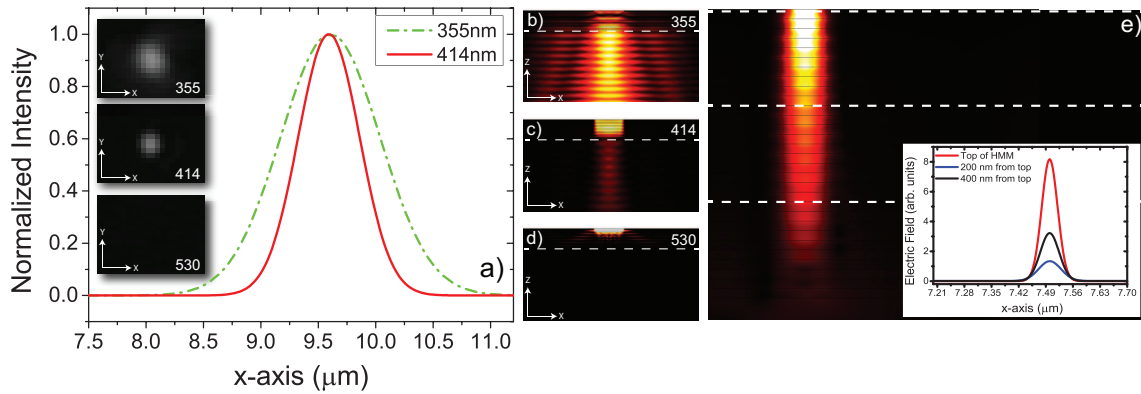
FIGURE 3.8: **a** Cuts of the transmitted beams acquired in confocal regime at three different incident wavelengths (355 (red solid line), 414nm (gree dashed line), and 530nm). Transversal profile intensity at 530nm results almost zero. Insets are the experimental spots obtained through the 5 ITO/Ag bilayers. **b-d** FEM simulations of the transmitted field from a 500nm width slit on the top of a 5 bilayer HMM at the same excitation wavelengths. Maximum of transmission is reached at 355 nm, but no collimation is visible (**b**). For 414 nm, transmission decreases, but a supercollimation effect takes place (**c**). At $\lambda = 530$ nm no field intensity is detected, but the typical cone profile is appreciable (**d**). We measured a reduction of about 40% in FWHM in the case of 414 nm as compared to 355 (from 1 micron to 0,610 microns). **e** represents the FEM analysis of the confinement of light coming from a 40nm slit placed at the top of the structure, that propagaes as a waveguide for more than 100 Rayleigh lengths.

The transmitted light spots reported in the insets of Fig. 3.8**a** have been acquired by means of a confocal analysis (see Methods). The red (solid) and the green (dashed) curves represent the normalized transversal intensity profiles of the incident pulsed beams at 414 and 355 nm, respectively. Transversal profile of the confocal image at 530nm is not reported because transmitted intensity resulted almost zero at this wavelength. It is well evident that the full width at half maximum (FWHM) of

the spot at 414 nm is much narrower than that one at 355 nm, thus confirming a supercollimation behavior. Figures 3.8**b**-3.8**d** represent the 2D FEM simulation related to the propagation of a plane wave at three different wavelengths, corresponding to type I (355 nm), canalization wavelength (414 nm) and type II region (530 nm). Light coming from a 500 nm slit placed at top of the first layer propagates through the realized HMM. It is clear that a maximum of transmission is reached at 355 nm, but no collimation is visible. For 414 nm transmission decreases, but a supercollimation effect takes place, corresponding to a "solitary wave" - having the size of the slit - propagating through the HMM structure. At $\lambda = 530$ nm no field intensity is detected neither in the experiments nor in the simulations, but the typical resonance cone intensity profile is clearly appreciable, providing a strong signature of the type II metamaterial behavior.

3.7 Subwavelength Waveguide and Perfect Lens

The ability of the proposed HMM to confine the light with a resolution given by the step of the structure[28] is also investigated by means of FEM simulations. As shown in Fig. 3.8**e**, the proposed metamaterial is able to confine the light coming from a 40nm slit placed at the top of the structure for more than 100 Rayleigh lengths. As a result, this device is the perfect candidate for plasmonic, deep-subwavelength bulk waveguides. As previously mentioned, in the "canalization regime" the same HMM structure can be used as a perfect lens. A subwalength sized object placed in close contact with this device can be easily resolved at its bottom with almost no changing in phase for all the Fourier components, because for $\varepsilon_\parallel = 0$ and $\varepsilon_\perp = \infty$, k_z results always equal to zero.[30]. In 2003 Ramakrishna et. al. have demonstrated the possibility of using an extremely anisotropic medium to achieve this condition,[30] under which the medium shows $\varepsilon_\parallel = 0$ and $\varepsilon_\perp = \infty$ simultaneously, proposing such a structure as a perfect lens. In this work we point out a quite different mechanism, by exploiting the unconventional refraction conical pattern that light undergoes inside

the HMM and by forcing the resonance cone angle to be zero, thus allowing to obtain an extreme resolution limited only by the spatial period of the multilayer. As shown in Fig. 3.1**b**, in such a regime losses along the extraordinary optical axis ($z-$axis) constitute the main obstacle toward a real device. The possibility of exploiting this structure as a perfect lens is demonstrated by the FEM simulation showed in Fig. 3.9.
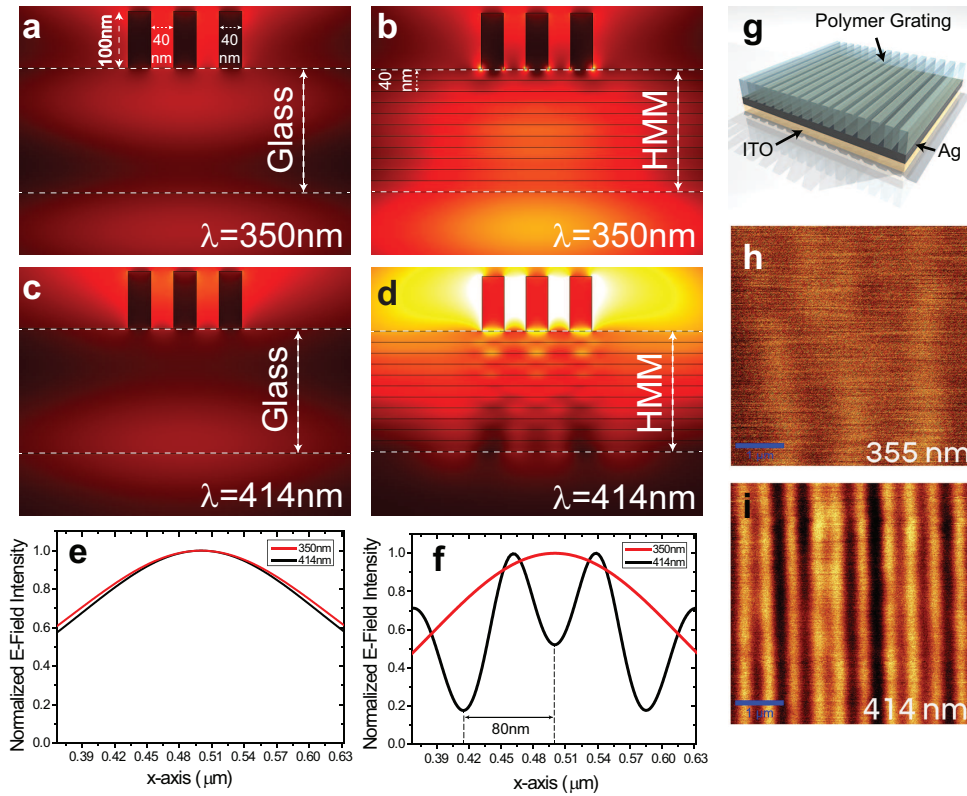
FIGURE 3.9: **a** and **c** represent the FEM simulations of a plane wave propagating from a slit of 500nm at the top of a three PMMA nanometric elements (100nm width, 10nm separation distance) through a glass slab of thickness 280nm, at two wavelengths (355 and 414nm). **b** and **d** represent the FEM simulations with the glass slab replaced by the HMM made of 5 bilayers (Ag-ITO 20-20nm). As appreciable from the transversal intensity profiles made at the exit of the glass/HMM (**e** and **f**), the system is able to resolve the nanometric structure with a resolution comparable to the step of the metamaterial.[28]

In the presented simulation, three PMMA ($n_{PMMA} = 1.49, k_{PMMA} = 0$) nanometric rectangular elements ($h = 100nm, w = 40nm$), separated by 40nm, have been positioned on top of the HMM and illuminated by a plane wave at two different excitation

wavelengths, 355 and 414 nm. Figures 3.9**a** and 3.9**c** represent the 2D FEM simulations in which the HMM has been replaced with a glass layer of the same thickness. In Fig. 3.9**e** the transversal intensity profile at the exit of the glass slab for the two wavelengths is reported. It is well evident that information about the nanometric elements is completely lost for both wavelengths. According to our study, by replacing the glass with the ε_{NZP} HMM, the behavior reveals a dramatic change (see 2D map in Fig. 3.9**b** and 3.9**d**). At the excitation wavelength of 355 nm (Fig. 3.9**f**, black dashed curve) the propagation through the HMM structure does not bring any information of the three objects separated by subwavelength distances, as expected for type I - HMM. By exciting exactly at the "canalization wavelength" (414nm, Fig. 3.9**f**, red solid curve), the image of the three nanometric objects is transferred to the exit of the HMM. Being the separation distance between two adjacent objects of only 40nm, we can ensure that it is possible to distinguish two objects with a resolution down to $\lambda/10$. In Fig. 3.9**g** we propose an experimental proof of concept of a real system. In order to keep the transmissivity of the device suitably high, a single ITO/Ag bilayer with a fill fraction of 50% has been realized. We want to stress out that it is well known that even a single bilayer can work as a hyperbolic medium.[31] Figure 3.9**g** shows a sketch of the proposed experiment. On the top of the bilayer a simple grating consisting of 250nm stripes separated by 250nm gaps has been written by a sophisticated two photon absorption lithography method (see Methods). This grating has been used as the subwavelength image, on the top of the HMM, to be resolved at its bottom. By means of a confocal experiment we tried to resolve the subwavelength grating by illuminating it with the same wavelengths used in the simulation. Results showed in Fig. 3.9**h** clearly demonstrate how the information about the subwavelength structure is completely lost for $\lambda = 355nm$ (even though this wavelength is shorter than the canalization one) while the grating is completely visible at the canalization wavelength $\lambda = 414nm$, demostrating the possibility of using such a medium as a near field superlens.

3.8 Methods

As a first step we engineered the metamaterial by means of the widely accepted EMT analysis.[32] It is worth noting that the optical constants used in this step have been extracted ellipsometrically directly from the original deposited layers. The final multilayer structure has been realized by means of a Physical Vapour Deposition (PVD) technique, by alternating 5 bilayers, each of which made of a transparent oxide and a metal. In particular a 20 nm thick layer of Indium Tin Oxide (ITO) has been deposited on a glass substrate by means of a DC Magnetron sputtering system (Edwards Auto 306), with a power of 40W for 2 minutes at a distance of 7.2cm between the substrate and the ITO target. Then, an Ag layer (20 nm thick) has been deposited on the ITO using 10W of power for 3 minutes. This constitutes the bilayer. For each deposition session a control sample has been placed side by side with the main one, allowing to check the optical properties of each sputtered layer, as well as its thickness and uniformity, at the end of each deposition. Spectroscopic ellipsometry has been used to perform this analysis by means of a V-VASE Ellipsometer (Woollam Co.). By setting up a multistep deposition procedure we were able to realize the complete multilayered metamaterial (see Fig. 3.11a, inset). Its good morphology has been investigated by means of the scanning electron microscopy analysis (SEM). Indeed, ellipsometry has been used as a powerful tool to perform angular transmission and reflection characterizations, as well as the Brewster angle evaluation.

An ultrafast optical set up has been used to measure the lifetimes of the samples. The optical set up consists of a Ti: Sapphire tunable femtosecond laser (Chameleon Ultra II, by Coherent Inc.), Pulse Picker (by Coherent), Second Harmonic Generator (by Coherent), and a spectrofluorometer for time-correlated single photon counting (TCSPC) instrument (by Edinburgh instruments). The time resolution of the TCSPC instrument is ≤ 5 ps. In the experiments, the Coumarin 460 dye was excited at 370 nm wavelength by using a pulsed laser with a pulse width of about 120 fs and a repetition rate of 4 MHz. Here the emission wavelengths were varied using a

monochromator that belongs to the TCSPC instrument.

A confocal analysis allowed us to verify the supercollimation properties of the HMM. The experiment has been carried out on a WITec alpha 300S Scanning Near Optical Microscope (SNOM), in confocal configuration. For both the excitation wavelengths (355nm and 414nm) a Ti:Sapphire tunable femtosecond external pulsed laser (Chameleon Ultra II, by COHERENT Inc.) has been duplicated in frequency (by second harmonic generation) and focused on the sample through a Zeiss 100x objective (0.75 of numerical aperture (NA)) confocal with a Leica 50x objective (0.5 NA), used at the bottom for collection. We ensured that both the energy and polarization of the external beam was the same for the two excitation wavelengths. Final detection was performed by means of a CCD camera.

In order to perform transmission and reflection simulations, we set up a classic Transfer and Scanning matrix method (TMM and SMM) code, implemented in MATLAB. Our code automatically takes into account the contribution of air, as an incoming medium and glass as an outgoing medium. Supercollimation and Perfect Lens simulation were performed by means of a Finite Element Method based code.

The 1D polymer grating on the top of the HMM structure, used to prove the perfect lens behavior of the obtained device, was obtained by a direct writing process based on a laser lithography system (by Nanoscribe GmbH) that enables true 3D micro- and nanofabrication via two-photon polymerization. The instrument (a Photonic Professional GT) combines two writing modes in one device: an ultra-precise piezo mode for arbitrary 3D trajectories and the high-speed galvo mode for fastest structuring in a layer-by-layer fashion.

3.9 Conclusions

In conclusion, in chapter 1, it has been demonstrated the design and fabrication of a hyperbolic metamaterial in which the coexistence of two extreme and opposite dielectric anisotropies is verified. The presence of the so-called *Ferrel-Berreman*

mode has been both theoretically and experimentally verified, confirming either the *epsilon-near-zero* regime and the *dielectric/type I* transition. The simultaneous presence of a zero and a pole (respectively in the in-plane and out-of-plane dielectric permittivities (ε_{NZP}) HMM) at $\lambda = 414nm$, has been theoretically predicted and experimentally observed. At this frequency the obtained dielectric singularity provides suitable conditions to experimentally achieve the so-called *canalization regime*, thus enabling the super-collimation effect precisely at this wavelength. Moreover, here we show how were able to exploit the properties coming from this regime to realize many fascinating devices, such as a HMM-based band-pass filter, manifesting performances far better than the commercial ones. We explain that, within this regime, it is possible to reach previously unpredictable light confinement in the bulk of a hyperbolic metamaterial, forcing a light beam with suitable frequency to propagate through the structure as a solitary wave. Therefore, a bulk nano-waveguide, on micron depths has been properly designed at this particular wavelength. The same device can be exploited as a near field "perfect lens", capable to reach a super-resolution down to $\lambda/10$, limited only by the step of the metamaterial structure.

Chapter 4

Metal-Semiconductor-Oxide Extreme Hyperbolic Metamaterials for Selectable Canalization Wavelength

As expressed in the previous chapter, for a classic two materials based HMM, the expressions for $\tilde{\varepsilon}_\parallel$ and $\tilde{\varepsilon}_\perp$ can be derived in the framework of the well known Effective Medium Theory (EMT). By imposing that $\tilde{\varepsilon}_\parallel \approx 0$ (ε_{NZ}) and, at the same time, $\tilde{\varepsilon}_\perp \approx \infty$ (ε_{NP}), the so-called *canalization regime* occurs for a precise wavelength, causing the effective cancellation of the intermediate gap region between the type I and type II regions. For a metal/dielectric building block the canalization regime can be obtained if the so-called epsilon near zero and pole (ε_{NZP}) condition is verified, that is, neglecting losses, $Re(\tilde{\varepsilon}_d) = -|Re(\tilde{\varepsilon}_m)|$ and $t_d = t_m$, being $\tilde{\varepsilon}_d$ and $\tilde{\varepsilon}_m$ the dielectric permittivities of the dielectric and metallic medium respectively and t_d and t_m their thicknesses. Unfortunately, once the materials are selected, there is no way to move the canalization wavelength by keeping the same components, thus limiting the design possibilities for a plethora of new metamaterials devices, based on this concept. In this chapter it is shown how to overcome this limit and open a whole visible wide design tunability window by introducing an HMM based on a building block made by three different materials, without the need to change them and just by carefully engineering their fill fractions. In particular, five trilayers based on a

metal-semiconductor-oxide building block are considered. Silicon has been chosen as the high index material also because its correspondent oxide possesses the suitable low refractive index for the proposed system. Therefore, SiO_2 represents the natural choice as the low index dielectric. As a metal we have chosen silver, because of its low losses and excellent plasmonic properties in the visible range. The choice of three materials as building blocks permits to have three variables, i.e. thicknesses of the two dielectrics and metal; by fixing one of them, it is possible to act on the other two to design the *type I/type II* transition wavelength at the desired position into the allowed range.

4.1 Effective Medium Theory extended to a three materials building block HMM

In the particular case of a three materials HMM (TM-HMM), that means a HMM based on a three materials building block, the full expressions for $\tilde{\varepsilon}_\parallel$ and $\tilde{\varepsilon}_\perp$ derived from the general forms given in [33] are expressed in equations 4.1 and 4.2

$$\tilde{\varepsilon}_\parallel = \frac{\tilde{\varepsilon}_{d_1} t_{d_1} + \tilde{\varepsilon}_{d_2} t_{d_2} + \tilde{\varepsilon}_m t_m}{t_{d_1} + t_{d_2} + t_m} \tag{4.1}$$

$$\tilde{\varepsilon}_\perp = \frac{\tilde{\varepsilon}_{d_1} \tilde{\varepsilon}_{d_2} \tilde{\varepsilon}_m (t_{d_1} + t_{d_2} + t_m)}{t_{d_1}(\tilde{\varepsilon}_{d_2} \tilde{\varepsilon}_m) + t_{d_2}(\tilde{\varepsilon}_{d_1} \tilde{\varepsilon}_m) + t_m(\tilde{\varepsilon}_{d_1} \tilde{\varepsilon}_{d_2})} \tag{4.2}$$

Where d_1, d_2 and m indicate respectively the first and the second dielectric and metal, whereas t_{d_1}, t_{d_2} and t_m are their thicknesses. From equations 4.1 and 4.2 it turns out that, in order to obtain simultaneously $\tilde{\varepsilon}_\parallel = 0$ and $\tilde{\varepsilon}_\perp = \infty$ the numerator of equation 4.1 and the denominator of equation 4.2 have to be sent to zero at the same time, so that two analytic expressions can be extracted for the two dielectrics thicknesses:

$$\begin{cases} t_{d_1} = -\frac{\tilde{\varepsilon}_{d_2} t_{d_2} + \tilde{\varepsilon}_m t_m}{\tilde{\varepsilon}_{d_1}} \\ t_{d_2} = -t_m \frac{\tilde{\varepsilon}_{d_1}^2 - \tilde{\varepsilon}_m^2}{\tilde{\varepsilon}_{d_1}^2 - \tilde{\varepsilon}_{d_2}^2} \frac{\tilde{\varepsilon}_{d_2}}{\tilde{\varepsilon}_m} \end{cases} \tag{4.3}$$

4.1. Effective Medium Theory extended to a three materials building block HMM 37

By contemporary imposing the conditions $t_{d_1} > 0$ and $t_{d_2} > 0$ in system **??** (we are only interested in positive thicknesses, that correspond to feasible devices), we find $\tilde{\varepsilon}_{d_1} < |\tilde{\varepsilon}_m|$ and $\tilde{\varepsilon}_{d_2} > |\tilde{\varepsilon}_m|$. By merging these two conditions it is possible to reach the design relation for a three materials based ε_{NZP} HMM:

$$\tilde{\varepsilon}_{d_2} > |\tilde{\varepsilon}_m| > \tilde{\varepsilon}_{d_1} \tag{4.4}$$

We choose silver as metal and a semiconductor (*Si*) as first dielectric, while we consider as second dielectric two different oxides: TiO_2 and SiO_2. As shown in Fig. 4.1**a** the design relation **??** can be also intuitively derived in order to have positive values for t_{d_1} and t_{d_2}. Clearly, the two points in which $|\tilde{\varepsilon}_m|$ intersects the two dielectric curves have not to be considered, because here a thickness equal to zero for the remaining dielectric is required, actually reducing to the case of a two materials ε_{NZP}. Below and above these values, negative thickness of at least one of the two dielectrics is required (see Fig. 4.1**a**), reaching a non-physical condition. In this work we will focus on real cases, considering values of $\tilde{\varepsilon}_m$ reasonably far from these two points, in order to not be forced to use too thin thicknesses of the two dielectrics, that are both too difficult to obtain with classical physical vapour deposition techniques and to consider in simulations. As shown in Fig. 4.1, the three-material combination with the higher design flexibility is the $SiO_2/Si/Ag$ triplet, showing a 255nm design range in the visible. Figure 4.1b reports the thicknesses of the two dielectrics to be used to obtain an ε_{NZP} HMM in the whole tuning range, as extracted by equation **??**. At 365nm the trilayer system becomes an Ag/SiO_2 HMM, while at 620nm the system to an Ag/Si bilayer HMM. Out of this range non physical solutions are found. In order to demonstrate the tunability of the trilayer system we designed two different systems, one showing an ε_{NZP} condition at $\lambda_{tr} = 450nm$ and the other at $\lambda_{tr} = 550nm$. Thickness of the silver layer is kept fixed at $t_{Ag} = 20nm$ for both the devices. By solving the system in equation **??** for $\lambda = 450nm$ the two dielectric layers thicknesses have to be dimensioned as follows: $t_{SiO_2} = 6.5nm$ and $t_{Si} = 5nm$,
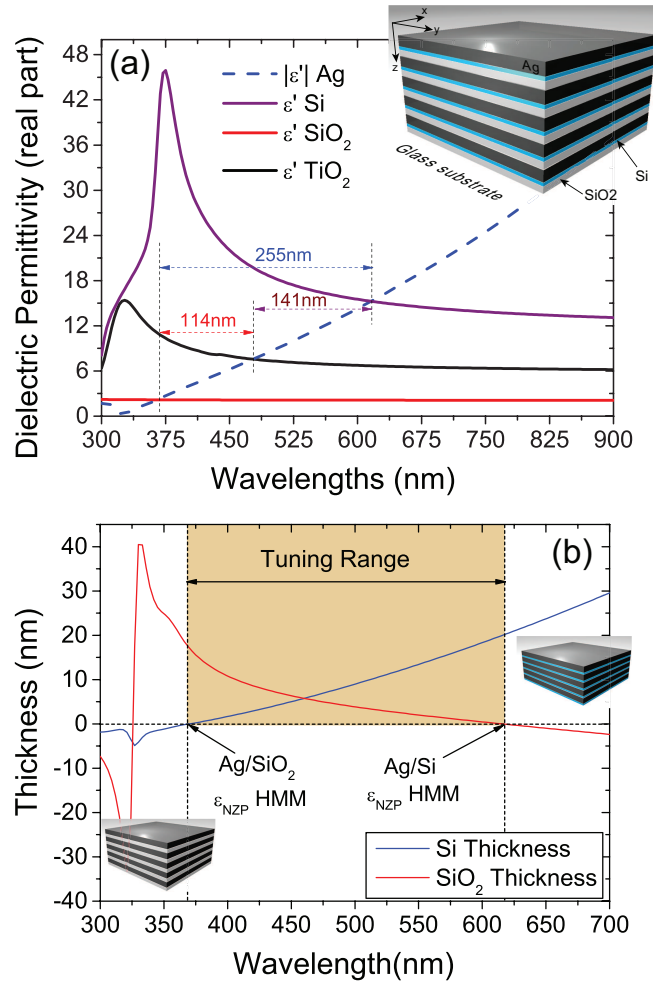
FIGURE 4.1: (a)Absolute value of the real part of *Ag* dielectric permittivity (dashed blue curve) in comparison with that one of *Si*,*SiO*2 and *TiO*2. Three triplets are possible. In the inset, a realistic sketch of the $SiO_2/S_i/Ag$ HMM considered in this work. (b) *Si* and SiO_2 thicknesses as extracted by equation 4.3. At 365nm the system becomes an Ag/SiO_2 HMM, while at 620nm system falls down in the Ag/Si bilayer HMM. Below 365nm and above 620nm solutions are not physical
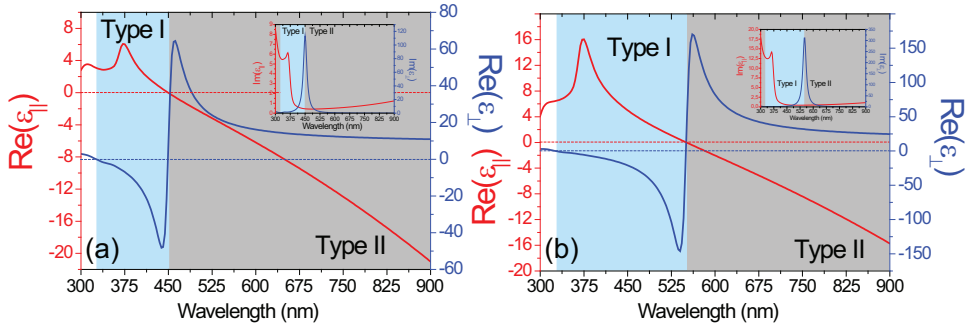
FIGURE 4.2: Effective Medium Theory (EMT) design of the two systems with transition wavelength between the two coexisting anisotropies at 450nm (a) and at 550nm (b). Imaginary parts showing the typical Lorentzian shape, peaked exactly at the transition wavelengths, are reported in the insets.

while for $\lambda = 550nm$ it results that $t_{SiO_2} = 2nm$ and $t_{Si} = 13.5nm$. In Fig. 4.2 the Effective Medium Theory design of the two samples is reported. In Fig. 4.2**a** the designed ε_{NZP} HMM behaves as a highly anisotropic dielectric in the deep UV range until 327nm, wavelength at which it undergoes its first phase transition, showing the behavior of a *type I* HMM. Recently Hoffman et. al. [19] demonstrated that a signature of such a phase transition (dielectric to *type I* HMM) is the presence of a narrow absorption peak exactly at the transition wavelength, detectable in reflection for a p-polarized impinging light wave close to the Brewster angle (next paragraph). At $\lambda = 450nm$ the HMM undergoes an additional dramatic phase change. At this wavelength the ε_{NZP} condition is satisfied, manifesting as a strong Drude like resonance, both in the real and imaginary parts of the $\varepsilon_\perp$. Indeed, at this inversion point of coexisting anisotropies $\varepsilon_\perp$ is forced to pass from a very high negative value (ideally equal to $-\infty$) to a very high positive one (ideally equal to $+\infty$). A sharp Lorentzian peak in the imaginary part of $\varepsilon_\perp$ in correspondence to the transition wavelength, confirms the resonant behaviour (see inset of Fig. 4.2**a**). Many fascinating properties arise exactly at this point, among which perfect lensing constitutes one of the most intriguing [30]. From $\lambda = 450nm$ on, the HMM shows the the so called *type II* HMM anisotropy. The considerations made for Fig. 4.2**a** are still valid for Fig. 4.2**a**, in which a new HMM is designed, with transition wavelength moved at $\lambda = 550nm$ just by changing the dielectric and semiconductor fill fractions.
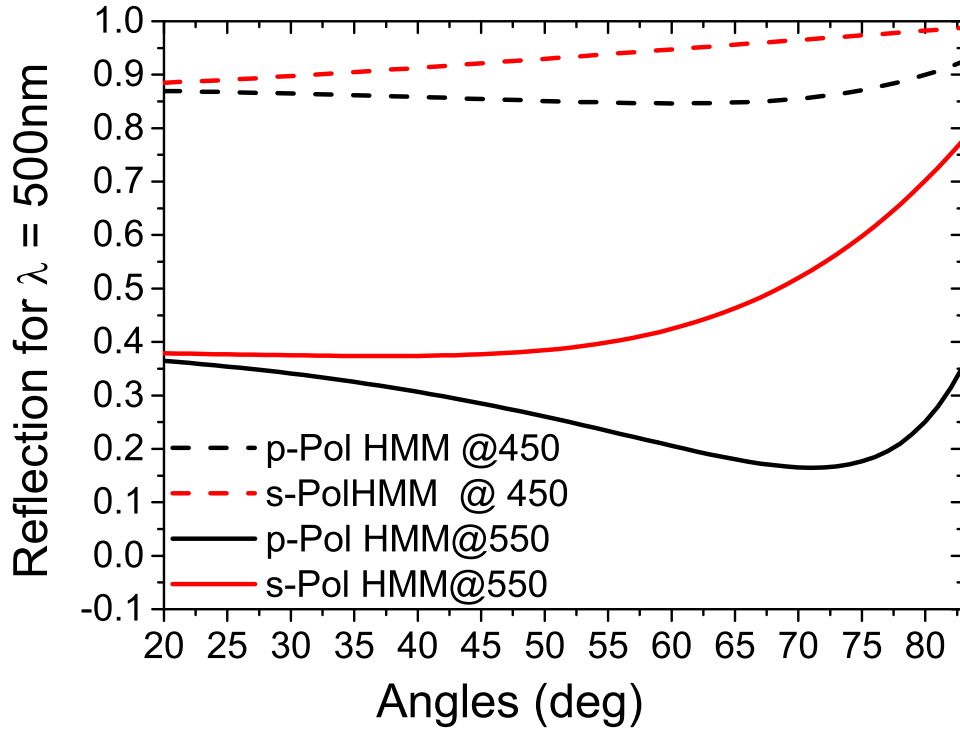
FIGURE 4.3: SMM based Brewster angle analysis carried at 500nm of the two HMM systems for excitation wavelength $\lambda = 500nm$. For the HMM with $\lambda_{trans} = 450nm$ no Brewster angle is detected for both polarizations p- and s- (dashed black and red curves, respectively), while for that one with $\lambda_{trans} = 550nm$ the Brewster angle is clearly visible (continuous black line, p-pol).

4.2 Brewster angle, Transmission and Reflection characterization

As a signature of the *type I* and *type II* regions, we calculated the Brewster angle for $\lambda = 500nm$, by using the scattering matrix method, taking into account also the glass substrate parameters on which the sample should be fabricated. It is evident that $\lambda = 500nm$ lies within the *type II* region for the device with $\lambda_{tr} = 450nm$. In this case no Brewster angle is expected. In the case of $\lambda_{tr} = 550nm$, $\lambda = 500nm$ lies in the *type I* region, and a Brewster angle is expected. Results are shown in Fig. 4.3, demonstrating that the two devices have been correctly designed.

Transmission and reflection spectra have been also calculated for different angles (0,
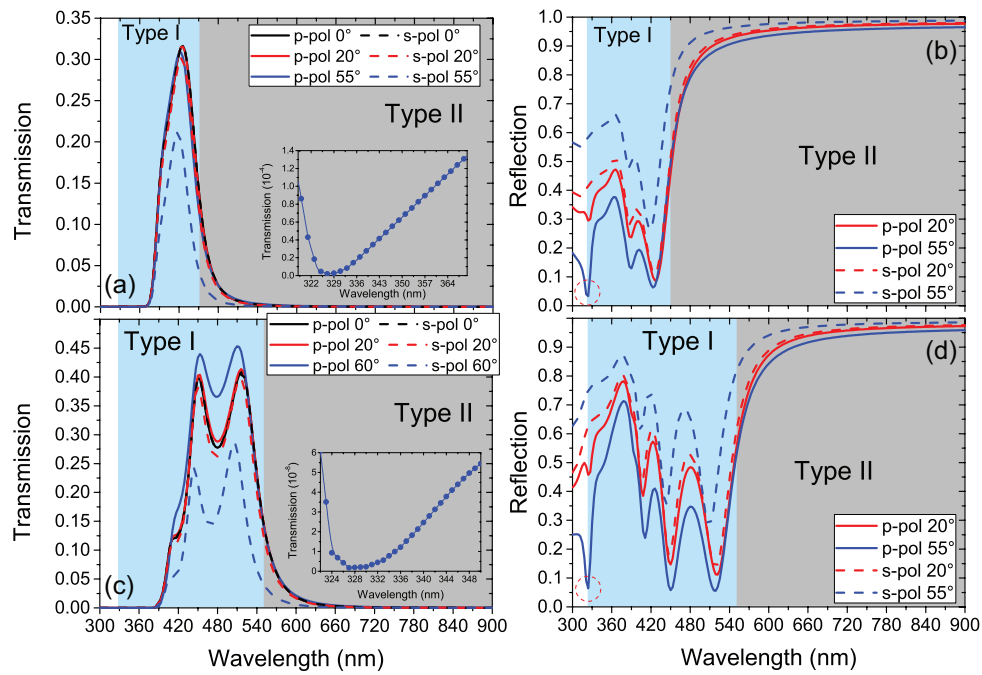
FIGURE 4.4: Transmission and Reflection spectra of the HMM with transition wavelength at $\lambda_{trans} = 450nm$ (a,b) and $\lambda_{trans} = 550nm$ (c,d) showing a range of transparency within the *type I* region and high reflectivity within the *type II* range. Insets of (a) and (c) correspond to a zoom of the dips present at 327nm, confirming the dielectric/type I transition, due to the presence of Ferrel-Berreman modes inside the structure.

20 and 55 degrees) by using a Transfer Matrix and Scattering Matrix Method (TMM and SMM, respectively), taking into account a glass substrate. Results are shown in Fig. 4.4. As predictable,[34] for both systems a strong reflectivity is achieved in the *type II* region. *Type I* region, instead, shows a typical high transmittivity window accompanied by many dips in the reflection curve, as shown in Fig. 4.4**b** and 4.4**d**. This modes can be interpreted as plasmonic bandgaps, as reported in literature. Moreover, a confirmation of the effective *dielectric/type I* transition (occurring at 327nm) comes from the so called Ferrel-Berreman modes, that appear in correspondence to an epsilon near zero medium. [22] Insets of Fig. 4.4**a** and 4.4**c** represent the transmission dips obtained for a p-polarized beam at an imping angle of $55°$, not visible in the main figures due to the high absorption of *Si* layers. Same dips at 327nm are well evident in reflection (red dashed circles in Fig. 4.4**b** and 4.4**d**).

4.3   Resonance Cone Angle and Finite Element Method analysis at the two transition wavelengths

Propagation of light waves is still allowed within the two hyperbolic regions *type I* and *type II*, following a preferred direction tilted at some angle, better known as *resonance cone* (RC)[24, 25, 26, 23, 27]. This respects the condition $\tilde{\varepsilon}_{\parallel} sin^2(\theta) + \tilde{\varepsilon}_{\perp} cos^2(\theta) > 0$, where $\theta_{RC} = atan(\sqrt{-[Re(\tilde{\varepsilon}_{\parallel})/Re(\tilde{\varepsilon}_{\perp})]})$ is the half angle between the two lobes of the resonance cone. From the last relation it is evident that both $\varepsilon_{\parallel} \approx 0$, or $\varepsilon_{\perp} \approx \infty$, implies θ_{RC} equal to zero, forcing the light to propagate as a single straight beam, highly confined inside the structure. In 2003 Ramakrishna et. al. demonstrated the possibility of using an indefinite medium operating at the canalization regime to design the near field perfect lens.[24, 28, 30] Figure 4.5 shows the spectroscopic behaviour of the resonance cone angle for the two systems. RC angle for each of the two HMMs approaches zero exactly at the respective transition wavelength: $\lambda = 450nm$ and $550nm$. A Finite Element Method (FEM) analysis shows that
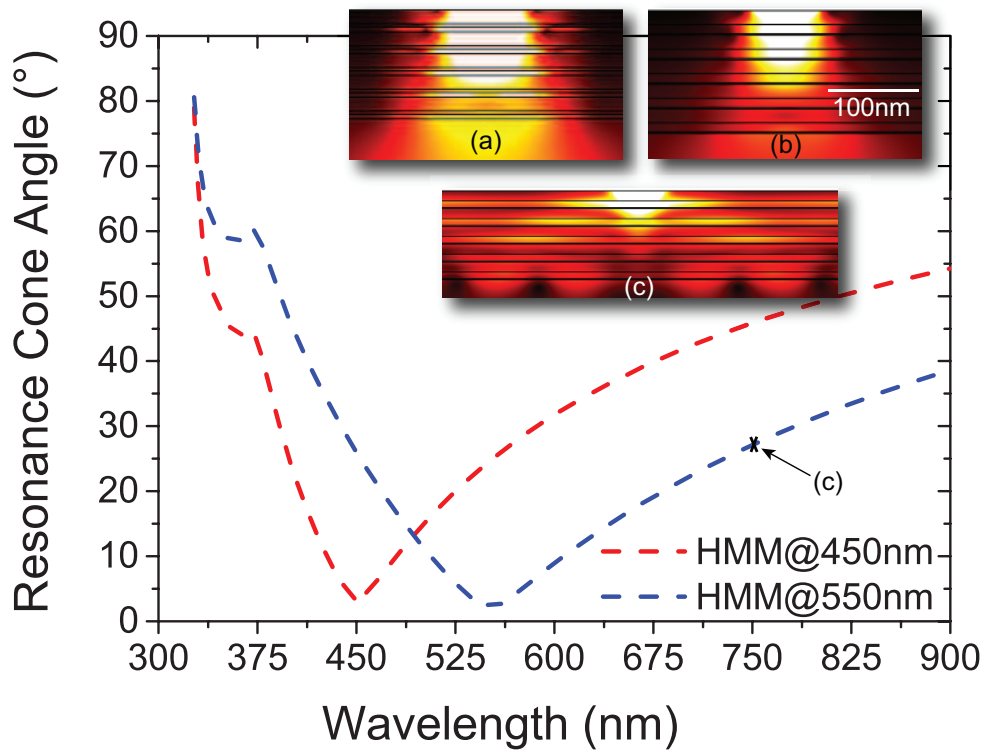
FIGURE 4.5: Resonance cones angle calculation for both the HMM systems showing a minimum very close to zero in correspondence of the two transition wavelengths. In the insets a FEM simulation of the electric field propagation inside the structures showing a canalization effect at the respective canalization wavelengths, manifested as a straight subwavelength confined light beam.

the electric field propagation within the HMM, coming from a 90nm aperture on the top of the stack, degenerates in one single straight and well collimated solitary beam when $\tilde{\varepsilon}_{\parallel}$ approaches zero and, contemporary, $\tilde{\varepsilon}_{\perp}$ reaches infinite values. This condition happens at the two transition wavelengths for the different HMM systems ((a) for HMM@450nm and (b) for HMM@550nm, respectively). Inset (c) of Fig. 4.5 represents the electric field propagation within the HMM structure with $\lambda_{trans} = 550nm$, simulated for a propagation wavelength $\lambda = 750nm$, showing the typical cone shape of the propagating field once we move from the transition wavelength.

4.4 Conclusions

In conclusion, in this chapter we demonstrated the possibility of overcoming the lack of design tunability of classic stack HMMs by introducing a third material in the 1D periodic multilayer lattice. In order to achieve an accurate design of the desired devices, a three element effective medium theory has been set up and two different systems have been studied, showing the transition wavelength at 450nm and 550nm, respectively. Both are based on the same three fundamental elements: silver as a metal, silicon as a high refractive index dielectric and SiO_2 as a low refractive index dielectric. By means of a SMM and a TMM we calculated the transmission and reflection spectra of the two different systems. Moreover we calculated the Brewster angle at $\lambda = 500nm$, wavelength that lies within the *type II* region for the first system, while in the *type I* for the second structure. Obtained results represent a clear signature of the nature of the two different HMMs. Also the Ferrel-Berreman mode, occurring at $\lambda = 327nm$ have been found confirming the effective dielectric/type I transition. Finally we explored the spectroscopic behavior of the resonance cone angle for the two HMM systems, showing values close to zero at the two transition wavelengths. The field propagation inside these structures, investigated by means of a FEM based simulation, confirms the presence of a "canalization regime" occurring

at the transition wavelength of the two structures. The presented method constitutes a simple but powerful tool to open the way to the fabrication of metamaterial based devices, like perfect lenses, super lenses, subwavelength super collimators and biosensors, in the whole visible range and, most importantly, for a specific desired wavelength in this range.

Chapter 5

Thermally-Reconfigurable Active Hyperbolic Metamaterials

By carefully analyzing equation 2.6, it turns out that $\varepsilon_\parallel$ can vanish at a specific wavelength where $\frac{\varepsilon_d}{\varepsilon_m} = -\frac{t_m}{t_d}$ and, in the resulting regime known as epsilon-near-zero (ε_{NZ}), many fascinating phenomena can occur. Unfortunately, once the fundamental components of an HMM are assembled, there is no way to tune the ε_{NZ} wavelength, unless a modification of their thicknesses and/or refractive indices is somehow induced. [35, 36, 37, 38, 39, 40, 41, 42] In this chapter, a simple method is presented to overcome the intrinsic lack of tunability and reconfigurability manifested by HMMs, thanks to a specifically engineered thermochromic dielectric material providing a thermally tunable response in the visible range. The introduction of a dye within the dielectric matrix allows a visual detection of the thermal reconfiguration, endowing the HMM with the capability of working as a chromatic temperature sensor. We demonstrate a temperature-induced, reversible tuning of the HMM ε_{NZ} wavelength and of both its transmission and reflection response. Such HMM may also be totally and irreversibly reconfigured, switching from an "effective metal" to an "effective dielectric".

5.1   Design and characterization of the new dielectric component

Due to its high refractive index and transparency in the visible range, TiO_2 was chosen as the basic component of the dielectric matrix. A fine tuning of the overall effective refractive index was accomplished by mixing TiO_2 with Polyvinylpyrrolidone (PVP) and the Coumarin C522B organic dye, both lossless dielectrics. PVP was selected because of its low refractive index and its solubility in ethanol, while C522B because of the good overlap of its emission band with the designed ε_{NZ} wavelength. An ellipsometric characterization of the TiO_2-PVP-Dye (TPD) dielectric was carried out on thin layers deposited on glass substrates by spin coating, (see experimental section). Figure 5.1 shows the real (n, Figure 5.1**a**) and imaginary (k, 5.1**b**) components of the refractive index of TPD, together with the same parameters for pure sintered TiO_2, unsintered TiO_2+PVP (TP), unsintered TiO_2+Dye (TD) and pure PVP. Undergoing a sintering process, TiO_2 approaches the crystalline phase of anatase, leading to its highest refractive index, as showed in figure **??**. Anyway, unsintered TiO_2 still manifests a suitably high refractive index. The absorption of the dye in TD and TPD is responsible for the Lorentzian peak of k (see Figure 5.1**b**) centered at $\lambda = 422$ nm. The presence of PVP acting as a favorable host for the dye in the TPD layer induces an increase of k (Figure 5.1**b**). A reduction of the thickness between unsintered (82 nm) and sintered (63 nm) TiO_2 of about 20 nm is ellipsometrically detected, demonstrating that the heating process is able to contract the layers containing TiO_2. This is the key mechanism conferring a thermally tunable response to the final HMM structure. Such a contraction results reversible within the typical application range from room temperature to 80°C. The same contraction has been observed in the TPD layer that, when prepared following the details described in the experimental section, at room temperature results of about 83 nm thick. A color switch from yellow to bright orange is gradually observed as the TPD layer is heated, highlighting how unsintered titania can act as a thermally reconfigurable

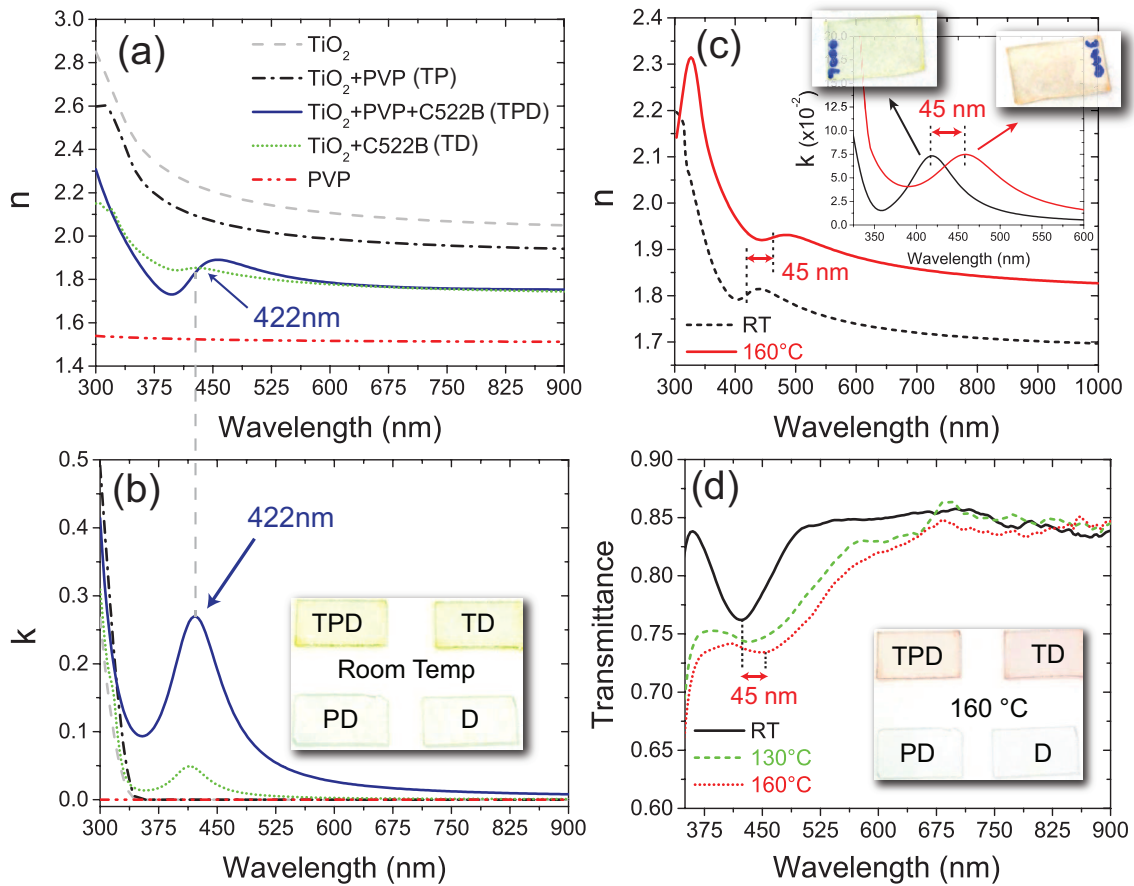FIGURE 5.1: Ellipsometric results for the real (a) and imaginary (b) refractive indices for pure sintered TiO_2 (dashed gray curve), TP (dot-dashed black curve), TPD (solid blue curve), TD (dotted green curve) and pure PVP (dash-dot-dot red curve). c) n and k (inset) of the TPD measured at room temperature (black dashed curve) and at 160 ÂřC (red curve). d) The transmittance of TPD, illustrating the 45 nm thermal shifting.
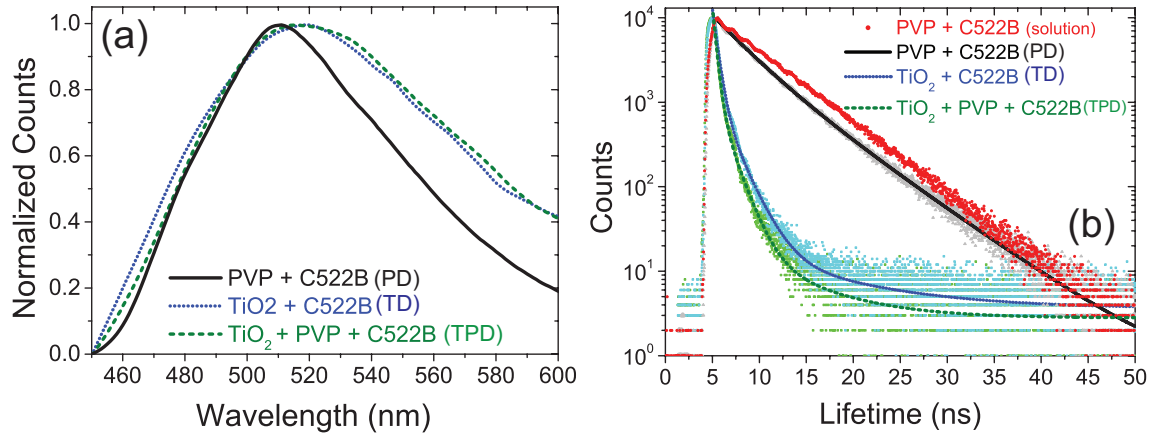
FIGURE 5.2: Luminescence spectra (a) and fluorescence intensity decay, recorded at the emission maximum (b) of examined samples.

template to finely tune the absorption properties of the embedded dye. The inset of Figure 5.1 demonstrates that a color change can be achieved only in the presence of TiO_2. In addition, ellipsometric measurements reveal an increase of the real refractive index of TPD towards the values of the sintered TiO_2 when TPD is heated up to 160°C (compare Figure 1**a** with Figure 5.1c). These optical and morphological variations lead to a marked temperature dependence of the absorption properties of the embedded dye, with a red-shift of the TPD Lorentzian absorption peak by about 45 nm between room temperature and $T = 160$°C, as shown in Figures 5.1c,d. The temperature induced reversible contraction responsible for the color change can be attributed to water absorption/desorption. In fact, when a yellow TPD layer kept at room temperature is introduced in a nitrogen atmosphere (less than 1 ppm H_2O), it immediately becomes bright orange, reproducing the effect observed upon heating. The yellow color is recovered as soon as the film is exposed again to ambient atmosphere.

The emission properties of TPD are illustrated in Figures 5.2a,b. The emission wavelength is red-shifted when compared with both PD (8 nm) and TD (1 nm): this points out the role played by TiO_2 in the emissive behavior of the dye embedded in TPD. Time-correlated single photon counting (TCSPC) measurements confirm the TiO_2 role on the dye photophysics (Figure 5.2a). While the luminescent intensity decays in the PD solution and in PD films are in the same time range (see red and

black curves in Figure 5.2a), those obtained from the TD and TPD films are remarkably faster. In particular, in the PD solution a single lifetime τ_1 of about 4.83 ns is present, while in the PD films two lifetimes are obtained: a longer one of 4.57 ns, that can be attributed to isolated dye molecules, and one of 1.8 ns, attributed to aggregated molecules. In both the TD and TPD films, two faster decay times were evidenced, $\tau_1, TD = 0.46ns, \tau_1, TPD = 0.31ns, \tau_2, TD = 1.89ns$ and $\tau_2, TPD = 1.65ns$. The very short τ_1 observed in both TD and TPD can be attributed to an energy transfer process to the TiO_2.

5.2   Design, realization and characterization of the thermally tunable HMM

An HMM-based on such a dielectric layer was engineered choosing silver as the metal. Figure 5.3 shows the real (a) and imaginary (b) effective dielectric permittivities of the HMM, calculated via EMT,[14] choosing thicknesses of 20 nm for Ag and 83 nm for TPD, with an ε_{NZ} condition at $\lambda_{trans} = 560nm$. Above this wavelength, the system behaves as a type II HMM. A three-bilayers HMM was fabricated as described in the experimental section and its reflection response was investigated (Figure 5.3c). As expected, the system manifests very low reflectivity below λ_{trans} while it becomes highly reflective above such wavelength. The same figure shows as these results are very well reproduced by Scattering Matrix Method (SMM) based simulations. The hyperbolic nature of the HMM was numerically confirmed by means of Finite Element Method (FEM) simulations. The inset of Figure 5.3b shows the simulated propagation of the incident field through a cross section of the multilayer structure. A resonance cone pattern, typical of an HMM working in the type II region, is clearly evident. Moreover, two dips in reflection corresponding to bulk plasmon polaritons (BPPs) modes, [43] are present in the effective dielectric range (see white area of Figure 5.3c). The thermal reconfigurability of the HMM has been
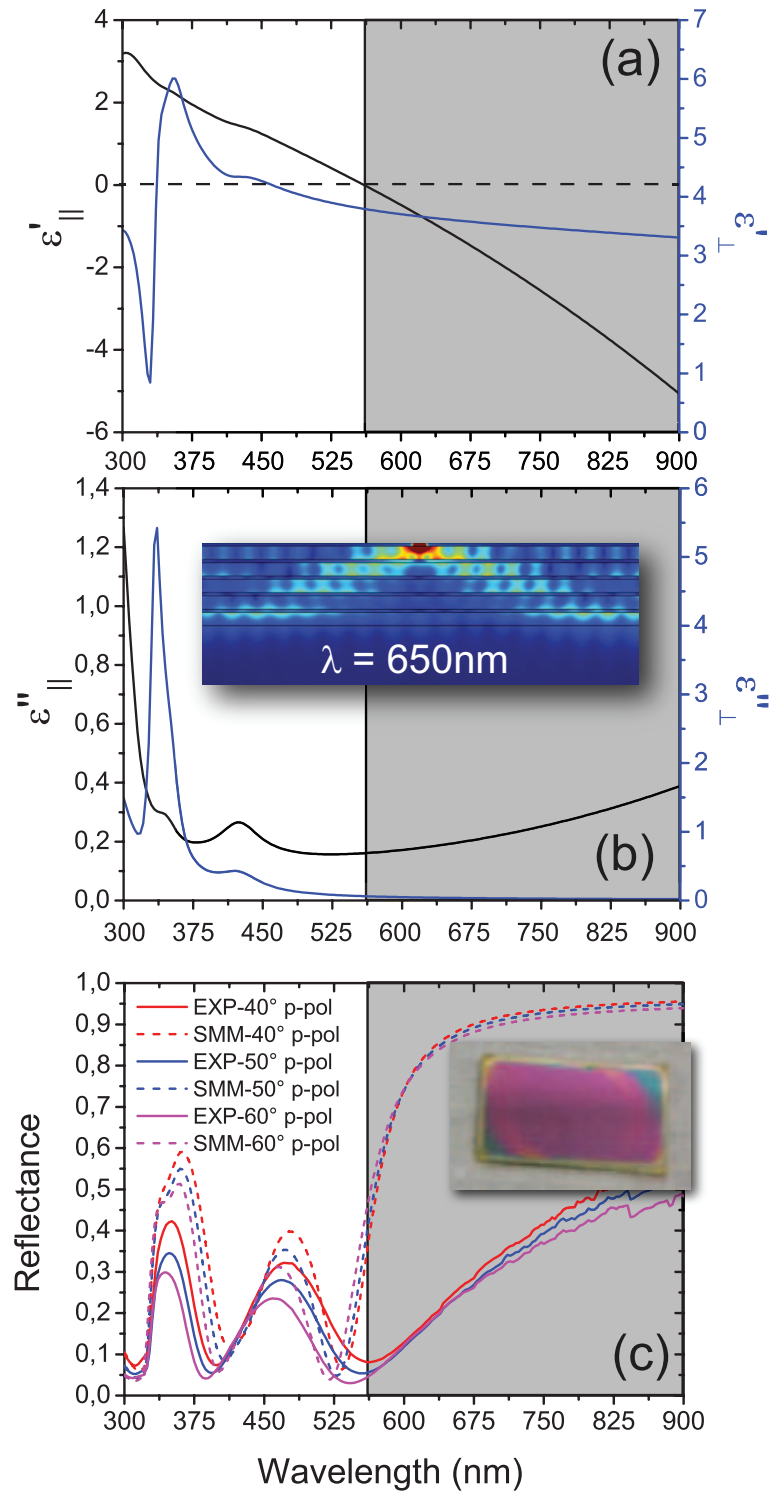
FIGURE 5.3: Effective medium design of the real (a) and imaginary (b) effective dielectric permittivities of the complete HMM. In the inset of (b) the typical resonance cone propagation pattern is evident. c) Experimental (solid curves) and SMM simulated (dashed curves) reflectance of a three-bilayers TPD-based HMM. The inset is a picture of the TPD-based HMM, showing a bright magenta color.
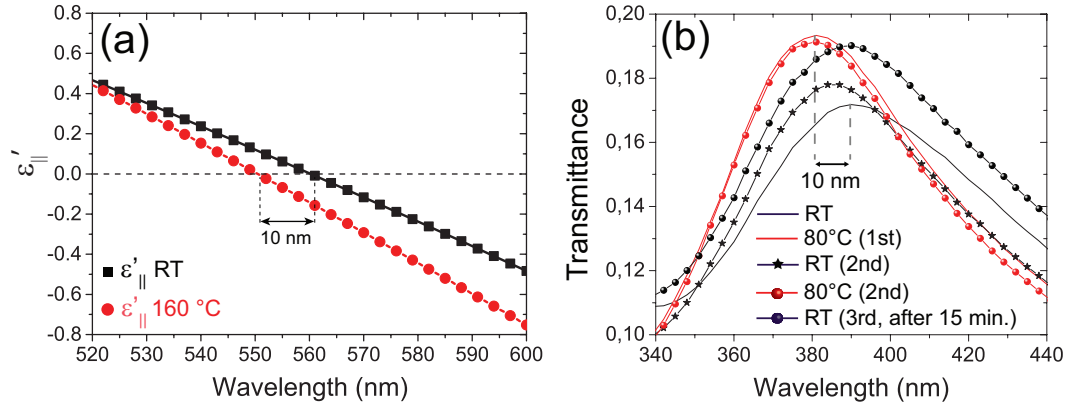
FIGURE 5.4: a) EMT calculated thermally induced blue shift of the HMM ε_{NZ} transition. Experimentally detected reversible thermal tuning of the transmission (b).

ellipsometrically investigated, revealing a reversible 10 nm blue shift in both the transmission and the reflection response by increasing the temperature from 20°C to 80°C. As shown in Figure 5.4a, thanks to both the dielectric layer contraction and the refractive index change, the ε_{NZ} wavelength blue shifts by about 10 nm.

The EMT calculation of the HMM $\varepsilon_{\parallel}$ has been indeed calculated by taking into account the optical constants and the thickness of the heated TPD layer, ellipsometrically measured. From the experiments, it turns out that the variation of the thickness of the TPD layer plays a major role in tuning the ε_{NZ} wavelength. The experimentally measured transmission (Figure 5.4b) and reflection (Figure 5.5a) reveal a similar trend, also after three heating cycles from room temperature (RT) to 80°C, underlining the reversibility of the phenomenon. Exactly as expected, indeed, the 10 nm blue shifting of the ε_{NZ} wavelength, makes the type-II anisotropy occur 10 nm before. It follows that a proportional blue shift of the reflection dip is expected (at the same wavelength the type-II HMM has to be more reflective). Such a consideration is perfectly confirmed by the experiments in figure 5.5a and reproduced by the SMM simulations shown in Figure 5.5b, that are also in excellent agreement with the experimental results.

In order to confirm the hyperbolic nature of the HMM and, at the same time, to investigate the capability of the system to modify the decay lifetimes of the embedded fluorophores, TCSPC measurements have been conducted. Figure 5.6 shows that the
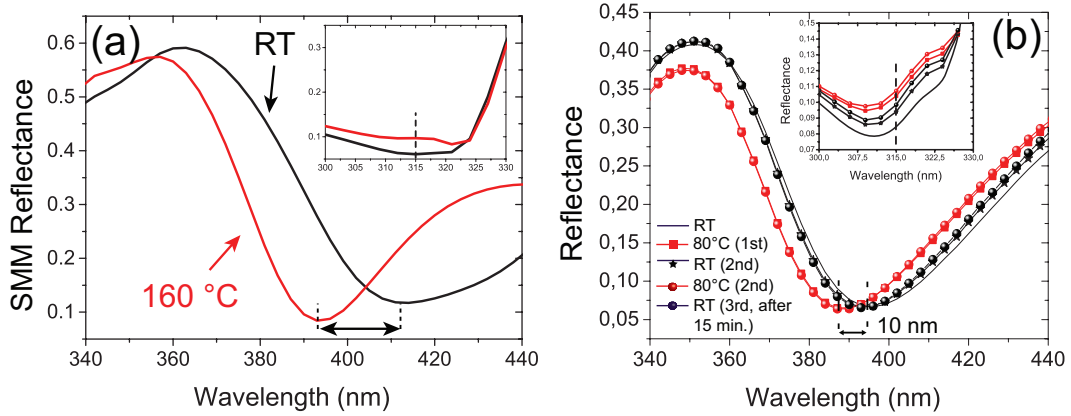
FIGURE 5.5: reflection (a) response of the HMM, in excellent agreement with the SMM simulations (b).

fluorescence lifetime (τ_1) of the dye in the HMM exhibits a flat trend as a function of the emission wavelength within the dielectric frequency range. Remarkably, in the case of the HMM, the lifetime results insensitive to the emission wavelength also in the type II region, in contrast with the increase detected at higher wavelengths in the pure PD layer, taken as a reference. Such an effect is due to the presence of the so-called high-k modes, typical of the HMM, providing a faster relaxation channel for the excited electronic levels, [31, 44, 45] and it demonstrates the possibility to reach very short fluorescence lifetimes.

The employment of the dye also represents the required condition for reaching a particular, recently theorized [46] emissive regime called "resonant gain epsilon near zero and pole HMM" in which the HMM can behave as a self-collimated nano-LASER or a self-amplifying perfect lens. A proof of concept of the possibility of inducing a complete inversion of the optical nature of the HMM system is illustrated in Figure 5.7a, where the Pseudo-Epsilon has been reported for a single bilayer. When the temperature is increased up to 160°C, a major irreversible morphological reconfiguration of the bilayer is induced.

Figures 5.7b and 5.7c show the AFM topography of the surface of the single bilayer measured at room temperature, which is much rougher after heating. This is reflected by a drastic change of the effective medium properties, switching from an effective metal to an effective dielectric, as detected ellipsometrically and shown
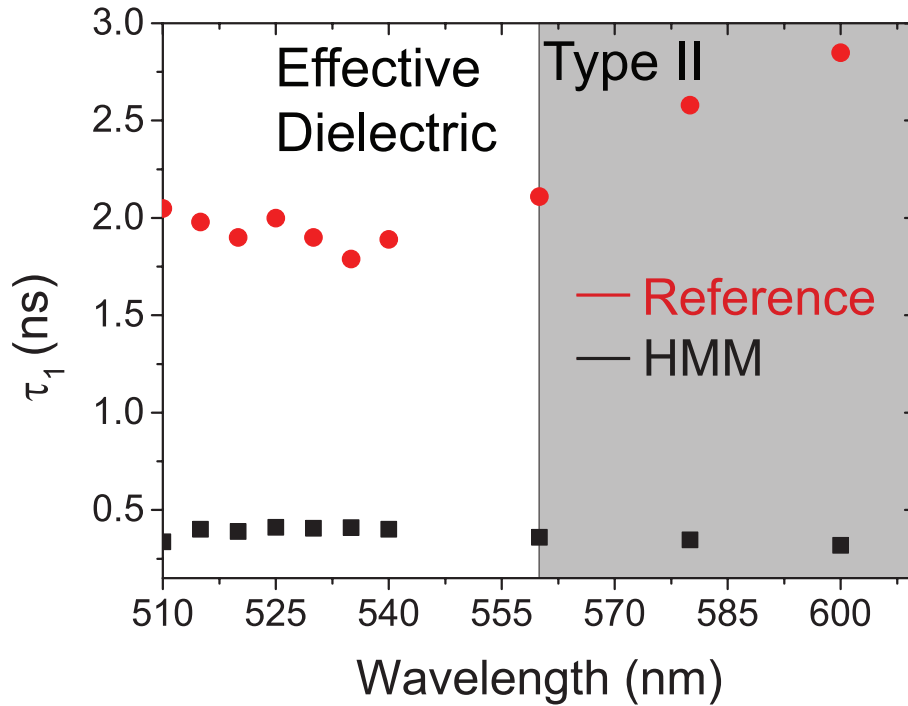
FIGURE 5.6: TCSPC measurements of the fluorescence lifetime of the fluorophores embedded in the HMM (black dots) and of the fluorophores embedded in a single TPD layer.

in Figure 5.7a. Such irreversible effect is probably connected with the reconfiguration of the titania structure due to a partial crystallization at $T = 160°C$ and to the consequent variation of the morphology of the Ag layer.

5.3 Materials and Methods

TiO_2 thin films were prepared by a sol-gel method, starting from titanium tetraisopropoxide $(Ti(OC_3H_7)_4)$ as a precursor. The process involved two steps: first, an acidic solution of ethanol was prepared by adding HCl 2M to the pure solvent $(14\mu L/1mL)$; $Ti(OC_3H_7)_4$ and anhydrous ethanol were then mixed $(140\mu L/1mL)$ and added dropwise to the first solution while stirring. For PVP and/or dye-doped solutions, 2% w/w of PVP 10.000 and/or 3% w/w of Coumarin 522B (with respect to $Ti(OC_3H_7)_4$) were added to the HCl/Ethanol solution. The final TPD solution was spread on a clean glass substrate by using a 0.45 μ_m Polytetrafluoroethylene (PTFE) syringe filter and then spun at 3000 RPM for one minute. TD and TPD samples were not sintered. Ag
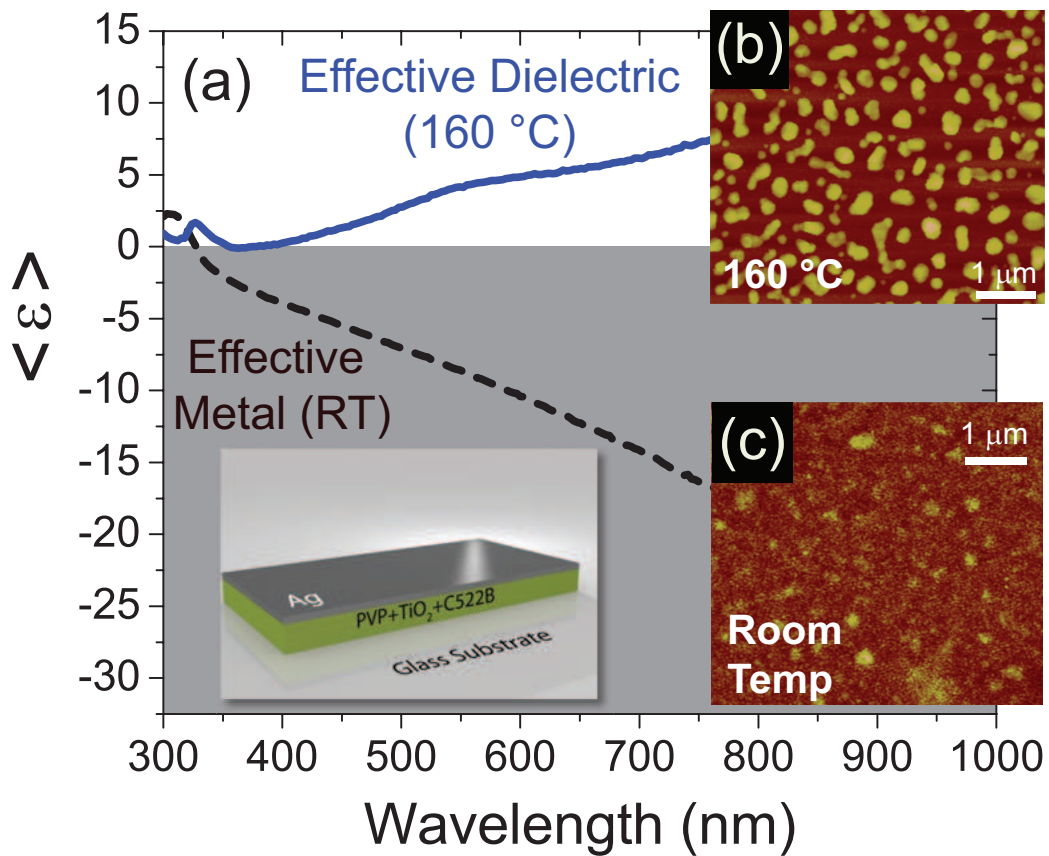
FIGURE 5.7: (a) Thermal conversion from a metallic to a dielectric behavior for a hyperbolic medium consisting of a single TPD/Ag bilayer. The thermal switching is revealed by ellipsometric measurements of the single bilayer pseudo-epsilon at different temperatures. AFM measurements on the surface of the single bilayer at room temperature (b) and after a 160°C (c) heating.

layers were thermally evaporated. The thickness of the evaporated layer was measured by means of a quartz balance during evaporation and double checked ellipsometrically. In order to fabricate the metamaterial, a multi-step process was followed, alternating spin coated TPD and Ag layers. Ellipsometry was used to characterize all of the optical properties of the TPD compound (absorbance, reflectance, transmittance and optical constants) together with its thickness and the optical properties of the overall metamaterial. A hot plate was mounted on the ellipsometer sample stage in order to perform measurements at different temperatures. Steady-state emission

spectra were recorded on an HORIBA Jobin-Yvon Fluorolog-3 FL3-211 spectrometer equipped with a 450 W xenon arc lamp, double-grating excitation and single-grating emission monochromators (2.1 nm/mm dispersion; 1200 grooves/mm), and a Hamamatsu R928 photomultiplier tube. To prevent the detection of second-order diffraction light from the source, cut/off filters were used. Time-resolved measurements were performed by using the time-correlated single-photon counting (TCSPC) option on the Fluorolog 3. A NanoLED at 379 nm, FWHM $< 200ps$ with repetition rate at 1 MHz, was used to excite the samples. The excitation source was mounted directly on the sample chamber at 90°C to a single grating emission monochromator ($2.1nm/mm$ dispersion; 1200 grooves/mm) and collected with a TBX-04-D single-photon-counting detector. The photons collected at the detector were correlated to the excitation pulse by a time-to-amplitude converter (TAC). Signals were collected using an IBH Data Station Hub photon counting module, and data analysis were performed using the commercially available DAS6 software (HORIBA Jobin Yvon IBH). The quality of fits was assessed by minimizing the reduced Chi-squared function (χ^2) and visual inspection of the weighted residuals.

5.4 Conclusions

In conclusion, in this chapter it has been shown how it is possible to endow a classic HMM with a reversible, thermally tunable response, thus overcoming one of the main limitations preventing such systems to express their full potential in practical applications. Lying in the visible range, the wide tunability range ($\approx 10nm$) of the ε_{NZ} wavelength, together with the overall optical response, represents a noticeable result, compared with the ones obtained with other methods. The key for achieving such a goal resides in the specifically designed dielectric layer (TPD), based on sol-gel, unsintered TiO_2, with morphological and optical properties highly sensitive to any temperature change and detectable as bright color changes. The addition of PVP and of the organic dye Coumarin C522B allows a fine design of the suitable

refractive index and provides remarkable emissive properties. The TPD layer itself is able to act as a reconfigurable template, where the absorption properties of the embedded dye can be thermally tuned within a noticeable 45 nm window. Due to the hyperbolic nature of the HMM, an increase of the decay rate of the embedded fluorophores was recorded. We also demonstrated the possibility of a total reconfiguration of the tunable HMM, irreversibly switching from an effective dielectric to an effective metal. The reported thermally tunable nature of the ε_{NZ} response is highly relevant for a wide range of applications, among which tunable supercoupling, energy squeezing, fine temperature sensing, one-time reconfigurable optical memories and anti-counterfeit nano-tags are noticeable examples.

Chapter 6

Resonant Gain Singularities in 1D and 3D Metal-Dielectric Multilayered Nanostructures

Even though, as shown since here, the application range of HMMs and, more generally, in plasmonic nanoresonators, due to the presence of the metal, one of the main drawbacks such structures bring along is constituted by their intrinsic ohmic losses right in correspondence to the resonant frequencies. In order to address the problem, the coupling with emitting (gain) media has been extensively studied. In this framework, Lawandy proposed a simple system constituted by a single metallic nanoparticle in a semi-infinite gain medium in which the point of view can be reversed.[47] By using a steady state complex description for the gain permittivity, he demonstrated the possibility not only to compensate the absorptive losses but also to exploit the typical resonant behavior of the nanostructure in order to provide a critical singularity in the particle polarizability, whose dependence on the gain quantity has then been investigated in this work.[48] Here, a steady state solution for the gain permittivity has been used, suggesting that the singularity can be linked to the transition between absorption and emission. Proof of this has been recently given in this paper.[49] Moreover, it has been reported that the use of a gain medium in presence of a so called "meta-structure" (a structure manifesting properties different

from those ones of its fundamental components) can provide a large effective amplification effect due to the strong local field enhancement inside the metamaterial,[50, 51] meaning that the collective effects due to the interaction of many fundamental nano-objects, would probably lower the amount of gain needed to produce amplification.

Positive net gain (*i.e.*, the gain that overcomes losses) has been in fact, experimentally found over macroscopic distances in a dielectric/metal/dielectric plasmonic waveguide, where the gain has been provided by an optically pumped layer of fluorescent conjugated polymer adjacent to the metal surface.[52] Furthermore, optical loss compensation effects have been recently observed in randomly dispersed nanoshell particles,[53, 54] where different fluorescent dyes were encapsulated into the dielectric part of core-shell nanoparticles.

In this chapter, we demonstrate how to achieve an extreme dielectric singularity in both the real and imaginary parts of the optical constants of a 1D nanoresonator system and in the imaginary part of the polarizability of a particular 3D system. The proposed structures have been specifically selected and engineered in order to exploit their unusual properties in the visible range, to reach the desired amplifying effects. The first system belongs to the class of Hyperbolic Metamaterials (HMMs), and is obtained by alternating lossy metal layers to gain functionalized dielectric ones, as shown in Figure 6.1a. The particular design and choice of the constitutive materials make it a so called "epsilon-near-zero-and-pole" (ε_{NZP}) HMM, allowing extraordinary light confinement properties thanks to which a strong Resonant Gain (RG) singularity can be engineered due to the presence of pumped dye molecules. Therefore, we refer to this structure as RG-ε_{NZP} HMM. As the main application for the RG-ε_{NZP} HMM, an Amplifying Perfect Lens (APL) has been designed and simulated with a resolution of about $\lambda_{\varepsilon_{NZP}}/S$, being S the periodicity (single bilayer thickness) of the RG-ε_{NZP} HMM. We will show how such a configuration can constitute a step further in single molecule nanoimaging, being able to reproduce and, at the same time, amplify deeply subwavelength details of nanometric objects placed on the top of the

metamaterial.

The second system is a three dimensional (3D) nanoresonator consisting in a spherical folded version of the RG-ε_{NZP} HMM constituted by a metal-dielectric, onion like, spherical multi-shell, obtained starting from a dye-doped dielectric core and alternating metal and doped dielectric shells (see Figure 6.1b). The importance of considering such a system resides, for example, in the demonstrated possibility to use gold nanomatryoshkas with plasmon resonances in the near-infrared (NIR) region of the spectrum to efficiently convert light into heat, a property useful for the photothermal treatment of tumors.[55, 56, 57] Nanomatryoshkas, usually consisting of a gold core and shell, separated by an interstitial nanometric SiO_2 layer, can selectively provide either a strong enhancement or a quenching of the spontaneous emission of fluorophores dispersed within their internal dielectric layer.[58] Furthermore, nanomatryoshkas have been used as tags in Surface Enhanced Raman Spectroscopy (SERS) measurements.[59] These tags show great potential for SERS-based biosensing and bioimaging.

In the wide "zoo" of single nanoresonator designs, this multi-shell configuration stands out for its versatility, being able to produce two different resonances in the polarizability response, which can be tuned through small and easily realizable morphological changes. This feature allows a fine placement of the resonances within the whole visible range, making such a system ideal for applications like photo-thermal therapy. In the end, the common nature of the resonant gain phenomena taking place in the two systems is highlighted making them ideal candidates also for the study of 1D and 3D surface plasmon amplification by stimulated emission of radiation (SPASER) effect.
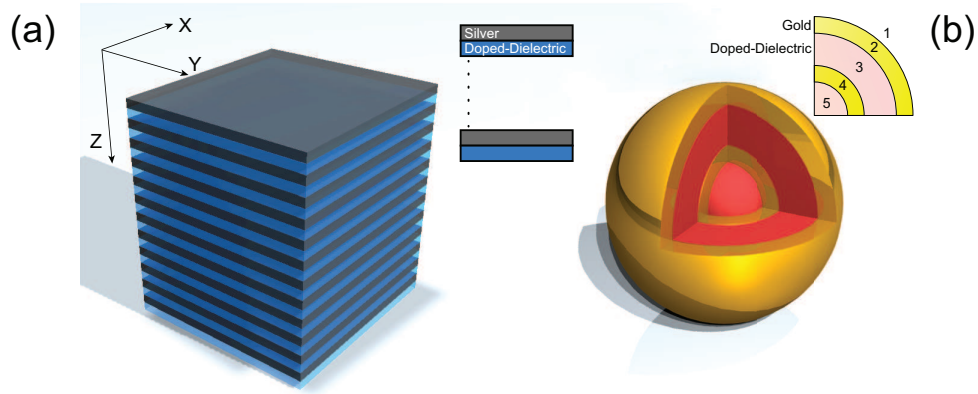
FIGURE 6.1: a,b) Sketch of the two gain functionalized multilayered systems. (a) A 1D nanoresonator based on a resonant gain ε_{NZP} hyperbolic metamaterial, obtained by alternating metal layers with dye doped dielectric ones. (b) A 3D nanoresonator constituted by a resonant gain multi-shell obtained starting from a dye doped dielectric core and alternating metal/dielectric shells.

6.1   Design of the Resonant Gain 1D nanoresonators

One of the most interesting one dimensional nanoresonators is represented by the so called Hyperbolic Metamaterial (HMM).[16, 23, 18] In general, HMMs are extremely anisotropic systems, whose simplest architecture consists of periodic, alternated metal/dielectric layers. If the size of the constitutive unitary cell (a single metal/dielectric bilayer) is designed to be deeply subwavelength and the total number of bilayers is high enough, then the complex optical constants of the overall effective HMM can be approximated by the well accepted Effective Medium Theory (EMT),[33] as shown in equation 2.6 and 2.7.

As expressed in chapter 3, at the canalization wavelength, the HMM undergoes a complete inversion of anisotropy, switching from a type I to a type II dielectric response. In 3, it has been also demonstrated that a wave at the canalization wavelength propagates through the HMM as a straight solitary beam, confined in a diameter comparable to the HMM period for more than 100 Rayleigh lengths.[45]

In the case losses cannot be neglected, the explicit form of equations 2.6 and 2.7 have to be considered (see equations 2.8 and 2.9), in which the real and imaginary

parts of the overall optical constants are considered. In this case losses play a fundamental role for an ε_{NZP} HMM, permitting to obtain many extraordinary optical phenomena connected to the amplification of self-confined evanescent waves.

It is well evident that both the real and imaginary parts of $\tilde{\varepsilon}_{\perp}$ manifest a pole if three conditions are simultaneously satisfied at the same wavelength (the canalization one):

$$t_d = t_m, \qquad \varepsilon'_m = -\varepsilon'_d \qquad and \qquad \varepsilon''_m = -\varepsilon''_d \qquad (6.1)$$

The first two conditions are easily obtainable by depositing same sized metal and dielectric layers, with opposite values of real permittivities (typical of the most common dielectrics and metals). We already discussed this case and how it is satisfied only at the canalization wavelength,[45, 28] referring to the obtained system as an ε_{NZP} HMM. As expressed above, the overall ε_{NZP} structure becomes able to collimate the canalization wavelength through the bulk, confining the light in a diameter comparable to the step $S = t_d + t_m$ of the HMM, leading to an ultra-subwavelength resolution in the order of $\lambda_{\varepsilon_{NZP}}/S$. The third condition requires a gain medium to be hosted in the dielectric layer and it is directly related to the fact that lossy materials have been considered. As proposed by Lawandy,[47] referring to an optically active nanoparticle system, a critical value of gain molecules can be identified, for which absorptive losses result completely compensated, a preliminary condition towards low threshold lasing action.[47] Here we demonstrate that the same behaviour can be found in the framework of lossy ε_{NZP} HMM, where, for a critical gain value and at the canalization wavelength, a strong resonance is detected both in the real and imaginary part of $\tilde{\varepsilon}_{\perp}$. We refer to this condition as "Resonant Gain epsilon-near-zero-and-pole" (RG-ε_{NZP}). Such an extreme behaviour constitutes an even more promising condition towards a low threshold lasing action. It is worth noting that the loss compensation dynamics in a general HMM has been theoretically [60] and experimentally [61] investigated considering a similar system constituted by a metal

and a dye doped dielectric, where a noticeable enhancement of the spontaneous emission rate of a fluorescent gain medium embedded in a HMM has been experimentally demonstrated.

In order to satisfy the third condition in equation 6.1 at the canalization wavelength, a suitable amount of gain molecules has to be embedded in the dielectric medium. Counter-intuitively, the exceeding of the resonant amount of gain molecules will cause a significant drop in the resonance amplitude. In general, when designing an ε_{NZP} HMM, in order to push the transition wavelength deep in the visible range, a high refractive index dielectric has to be considered. In this work TiO_2 will be considered as a high refractive index dielectric host matrix for the gain medium, because of both its relatively high index and transparency in the visible range. Therefore, choosing Ag as metal and TiO_2 as dielectric medium, it is possible to design an ε_{NZP} HMM at $\lambda = 426nm$.

The optical constants of the dye doped TiO_2 dielectric medium have been calculated as expressed in materials and methods section. Dielectric permittivities obtained for three different dye densities are plotted in Figure 6.2a (real parts) and Figure 6.2b (imaginary parts). The real part of the dielectric permittivity of undoped TiO_2 (black curve, Figure 6.2a) crosses that one of silver (absolute value, dashed blue curve Figure 6.1a) at $\lambda = 426nm$, thus fixing the transition wavelength for the ε_{NZP} condition. Once the canalization wavelength is fixed, a gain medium has been selected so that its emission peak coincides exactly with the canalization wavelength. As an example we can consider the Coumarin 500 dye, by Exciton, that possesses all the proper parameters if embedded in a HMM and pumped by a modelocked Ti:Sapphire pulsed laser (see materials and methods). Figure 6.2d reports the behavior of the imaginary part of the overall $\tilde{\varepsilon}_\perp$ as a function of the dye concentration ($\overline{N}_0$, see equation 6.2 in materials and methods) inside the TiO_2 matrix. A resonant amount of gain is found at the concentration of $\overline{N}_0 = 6.1 \times 10^{18} cm^{-3}$, showing a strong singularity that makes the ε_{NZP} HMM an extremely lossy system for immediately lower dye concentrations. Remarkably, concentration values lying in such an
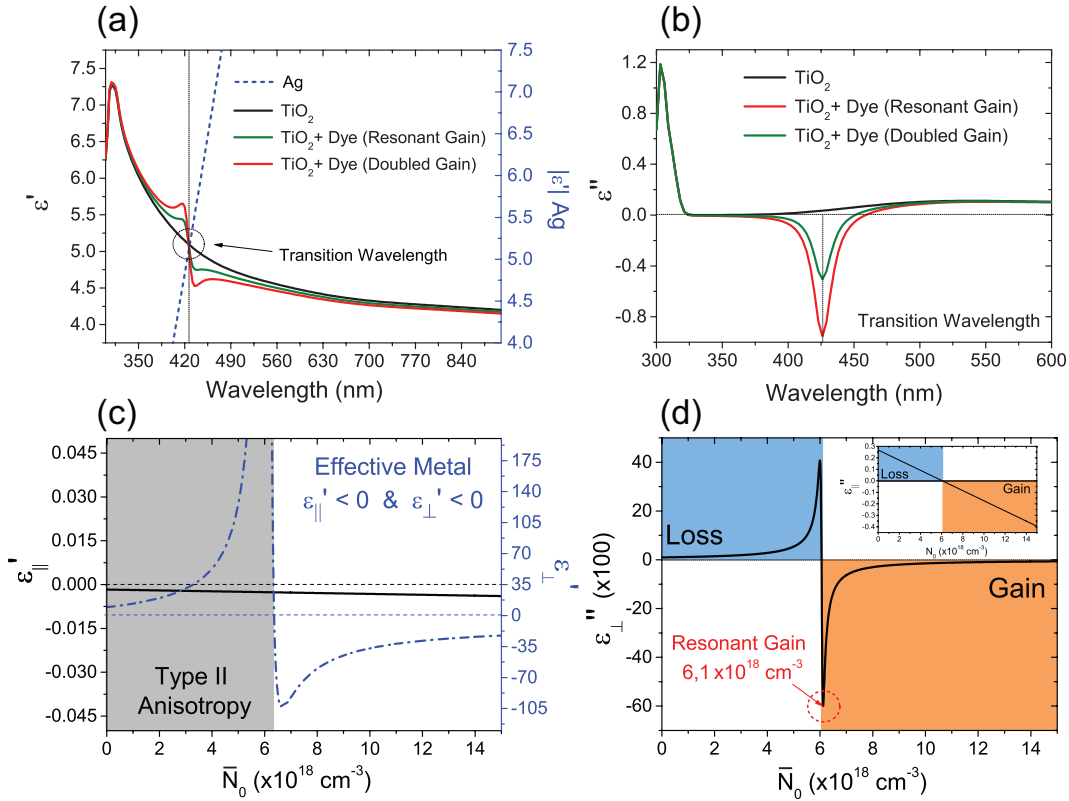
FIGURE 6.2: (a) Real and (b) Imaginary calculated dielectric permittivities of pure TiO_2 (black curve), TiO_2 doped with the resonant amount of gain molecules (green curve), overdoped TiO_2 (doubled amount of gain molecules, red curve). The crossing wavelength with that one of silver (absolute value, dashed blue curve) remains the same for all the three cases. (c) Effective Medium Theory calculation of the real part of $\varepsilon_\parallel$ (black) and $\varepsilon_\perp$ (dash-dot blue) as a function of $\overline{N}_0$. It is evident an effective metal behavior after the resonant gain value of $6.1x10^{18} cm^{-3}$ (d) Effective Medium Theory calculation of the resonant amount of gain molecules driving $\varepsilon_\perp$ to a singularity. In the inset, the linear behaviour of $\varepsilon_\parallel$ is reported.

order of magnitude are perfectly feasible and coincide with the most widely reported in literature.[47, 62, 63] The reason why a complete compensation of the losses can be reached without the need for enormous dye densities, resides in the fact that the single dye doped dielectric layer is not expected to overcompensate the losses of the metal layers, since the achievement of a resonance is ascribed to an overall contribution of the whole metamaterial. Inset of Figure 6.2d represents the linear decrease of the imaginary part of the $\tilde{\varepsilon}_\parallel$ as a function of $\overline{N}_0$. At this point, it is important to underline that changing the amount of the dopant agent does not modify the transition

wavelength. Indeed, by designing the system so that the emission peak of gain material coincides with the canalization wavelength of the ε_{NZP} HMM, the only effect of the introduction of a dopant in the dielectric layer, is the appearance of the typical resonant Drude like curve in the real part of the dye doped TiO_2 dielectric permittivity (see green curve in Figure 6.2a). As a consequence, exactly in correspondence of
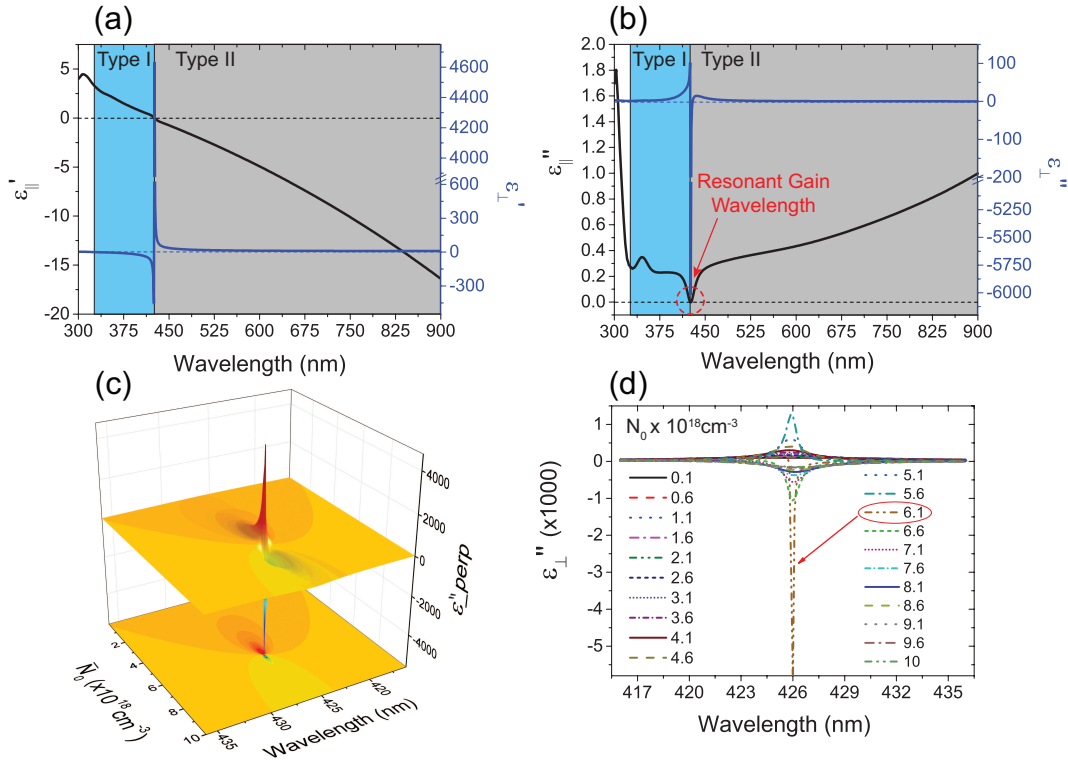
FIGURE 6.3: (a) Real and (b) imaginary part of the effective dielectric permittivities calculated by means of the Effective Medium Theory approximation considering the resonant amount of gain. The singularity is well evident exactly at the transition (type I/type II) wavelength, leading to an extremely high negative value of $\varepsilon''_\perp$. (c) Surface of the $\varepsilon''_\perp$ as a function of $\overline{N}_0$ and wavelength. The resonant behavior is well evident around 426nm and $\overline{N}_0 = 6.1 x 10^{18} cm^{-3}$. (d) Cuts of the previous surface for different values of $\overline{N}_0$. The strong negative value in correspondence of the resonant amount of gain is evidenced.

the flex of this curve, a negative Lorentzian peak in the corresponding imaginary part appears (see figure 6.1b). Increasing the amount of dopant has the double effect of increasing both the absolute value of the Lorentzian peak and, as a consequence, the amplitude between the relative maximum and the relative minimum in proximity of the real optical constant flex. Green and red curves of Figure 6.1a show the behavior

of ε' for TiO_2 doped with a resonant amount of gain (green) and a doubled value (red), respectively. It is worth noting that the two curves still cross the dashed blue one ($|\varepsilon\prime|$ of Ag) exactly at the same wavelength, in the sense that the ε_{NZP} wavelength does not change. Moreover, even if double dye doped TiO_2 layer manifests a higher imaginary dielectric permittivity (meaning that it gains more, see red curve in Figure 6.1b) with respect to the resonant doped dielectric (see green curve in Figure 6.1b), the absolute value of $\varepsilon_{\perp}^{''}$ moves towards zero (Figure 6.1d), while the absolute value of $\varepsilon_{\parallel}^{''}$ increases (inset of Figure 6.1d). Figure 6.1c shows the real parts of the effective optical parameters of the HMM, calculated at the canalization wavelength (426 nm) as a function of the number $\overline{N}_0$ of dye molecules embedded in the dielectric layers. These values play a crucial role in analysing the behavior of the double dye doped configuration. As said before, the resonant behaviour appears in both the imaginary and the real part of the effective dielectric permittivities. Such a feature induces, in correspondence of the resonance, a rapid passage from very high positive values to very high negative ones in the real part of $\tilde{\varepsilon}_{\perp}$, determining a topological transition of the overall HMM from a type II to an effective metal anisotropy (see Figure 6.1c). This means that, for values of $\overline{N}_0$ higher than the resonant one, the HMM behaves as an effective metal, becoming extremely reflective. This is the reason why, increasing the dye density above the resonant condition, results in an attenuation of the light propagating through the bulk of the metamaterial. Once the resonant amount of dye molecules has been detected, the dye doped dielectric has been designed and the complete HMM has been engineered by means of the well accepted Effective Medium Theory (EMT) (see Figures 6.3a and 6.3b), considering same thickness layers of 20 nm of alternatively Ag and dye doped TiO_2. The obtained RG-HMM shows a type I/type II transition at $\lambda = 426nm$. The resonant gain behavior is well evident in Figure 6.3b, where the imaginary part of $\tilde{\varepsilon}_{\perp}$ (blue curve) undergoes a strong singularity, reaching ideally infinite negative values. As a consequence, both the real and the imaginary parts of $\tilde{\varepsilon}_{\perp}$ are forced to manifest the same resonant feature. A synthesis of the $\varepsilon_{\perp}^{''}$ behavior as a function of $\overline{N}_0$ and λ is reported in the 3D map showed in

Figure 6.3c, while a systematic study of the resonant behaviour of the HMM has been reported in Figure 6.3d, in which a gain ($\varepsilon''_\perp$) per wavelength plot over the dye density is provided, highlighting the appearance of the resonance exactly at $\lambda = 426nm$ for $\overline{N}_0 = 6.1 \times 10^{18} cm^{-3}$.

6.2 Resonant optical response of the two multilayered structures

The amplification properties of the designed multilayered structures have been studied by means of different approaches. The 1D nanoresonator properties of the RG-ε_{NZP} HMM have been checked by means of a classic Transfer Matrix Method (TMM). As a first step, the ideal number of bilayers has been identified as the one which ensures the higher amplification. Figure 6.3a reports the calculated transmittance of the amplified wavelength ($\lambda_a = 426nm$) through the whole RG-ε_{NZP} HMM as a function of the HMM bilayers number. In particular, it is found that with a number of 12 bilayers, an enhancement of about 10 times in the transmitted light is obtained (transmittance value of 1 means hundred percentage). Such a behavior is not found with a lower or higher number of bilayers while, interestingly, a second peak in transmittance is detected in correspondence of 24 bilayers. This can be explained by considering the entire HMM structure as a resonant cavity with a gain modulation. It has been demonstrated that the balanced interplay between losses and gain may give rise to many light-matter interaction effects that extend far beyond the merely intuitive loss (over) compensation effects, including, for instance, absorption-transmission enhancement [64] and spectral singularities,[65] with perspective applications to new-generation optical amplifying devices. In optics and photonics, such nonlinear gain/loss periodic systems are routinely encountered in laser configurations or in nonlinear active cavities.[66, 67, 64, 68, 69, 70, 71] As shown in the inset of

Figure 6.3a, by stacking 12 bilayers of 40 nm thickness, a 420 nm thick cavity between the first and the last *Ag* layer is formed, and the RG-HMM behaves as a self sustained cavity for the amplified transition wavelength ($\lambda_a = \lambda_{tr} = 426nm$). One of the main advantages is that being the HMM itself a resonant cavity, it automatically supplies the necessary feedback mechanism, selecting the resonating surviving mode. Moreover it has been reported by Ramakrishna et. al. [72] that for a medium fulfilling the ε_{NZP} conditions ($\varepsilon'_{\parallel} = 0 \wedge \varepsilon'_{\perp} = \infty$), it is always true that the only present wavevector shows $k_z = 0$. Such a consideration is straightforwardly derived from the typical dispersion relation of an hyperbolic medium: $\frac{k_x^2 + k_y^2}{\varepsilon_\perp} + \frac{k_z^2}{\varepsilon_\parallel} = \frac{\omega^2}{c^2}$. Therefore, under the ε_{NZP} condition, and even more for a RG-ε_{NZP} one, no lateral wavevectors survive, giving rise to a straight well collimated soliton propagation path. Moreover, the proposed RG-ε_{NZP} HMM system presents a periodic balanced gain/loss spatial modulation, assuming a behaviour similar to the structures analyzed in references,[73, 67] in which a lasing action has been already demonstrated. Once fixed the number of bilayers to 12, the behavior of the HMM at the transition wavelength has been investigated as a function of the amount of gain molecules embedded in the dielectric medium. Results are shown in Figure 6.3b. In particular we consider two scenarios, one with the resonant gain density ($6.1 \times 10^{18} cm^{-3}$, solid red curve) and another with a doubled one ($12.2 \times 10^{18} cm^{-3}$, solid green curve, multiplied by 5 to be clearly seen in the graph). Counter-intuitively but exactly as expressed before, when doubling the amount of gain molecules, a type II/effective metal transition is provided, the HMM becomes extremely reflective and the propagation inside the structure results extremely attenuated. An even worse behavior is obtained by considering a number of bilayers equal to six (see Figure 6.3b, black solid curve, same amount of resonant gain, 3 times increased to be visible in the graph). Monocromaticity of the RG-HMM has been confirmed by measuring a Full Width at Half Maximum (FWHM) of 1 nm, for the amplified transmission peak.
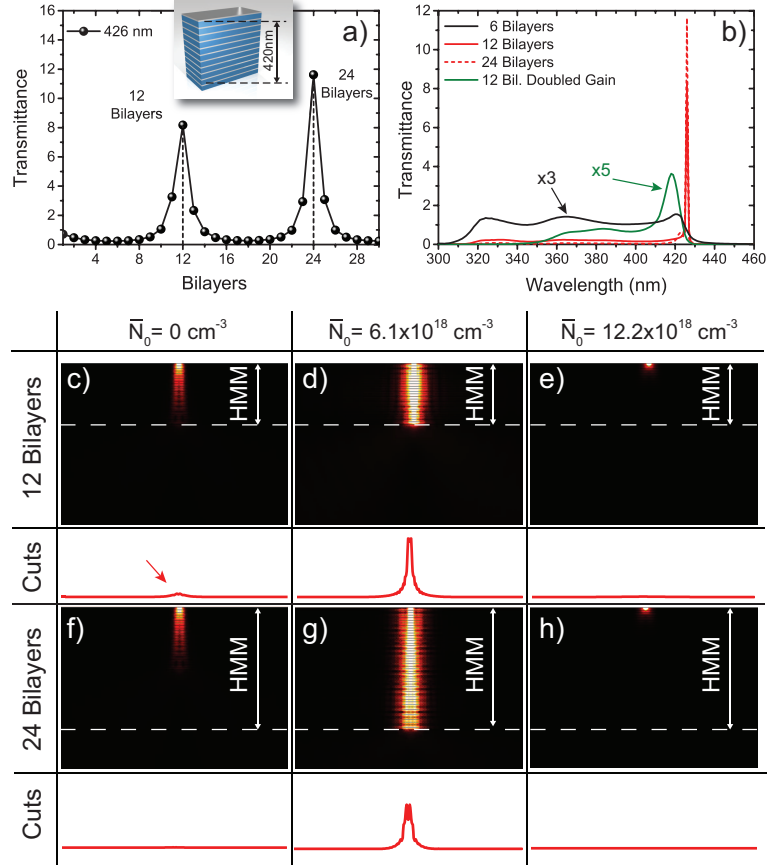
FIGURE 6.4: (a) TMM based engineering of the resonant number of metal/dielectric bilayers. It is found that at n = 12 bilayers the HMM behaves as a resonant cavity for the canalization wavelength. (b) TMM based simulation of the RG ε_{NZP} HMM. Structures with 12 and 24 bilayers manifest a giant enhancement of the transmitted light. (c,d,e) FEM based simulations of the 12 bilayer RG ε_{NZP} HMM and (f,g,h) of the 24 bilayers RG ε_{NZP} HMM, demonstrating the giant amplification obtained with the resonant amount of gain molecules (d,g) with respect to the simple passive ε_{NZP} HMM (c,f) and the doubled gain RG ε_{NZP} HMM (e,h).

As expressed above, one of the main, intrinsic features of the considered RG-ε_{NZP} HMM architecture, is the ultra-subwavelength collimation of the light propagating through the structure at the canalization wavelength. In order to confirm such a property, FEM based simulations have been performed, analysing the emission pattern through the 1D nanoresonator coming from a vertically oriented point dipole placed at the top of the HMM. Three different amounts of gain have been considered for the two different bilayers number (12 and 24) found to be the resonant ones. The first case is referred to the pure TiO_2 (gain molecules $\overline{N}_0 = 0 cm^{-3}$, see Figure 6.4c

and 6.4f): in this case the canalization wavelength is still detected in both the 12 and 24 bilayers systems but the absence of a gain material results in a very low light intensity at the output (see the cuts at the output of the HMM structure). The second case (Figure 6.4d and 6.4g) considers a HMM embedding the resonant gain amount in the dielectric layers ($\overline{N}_0 = 6.1 \times 10^{18} cm^{-3}$). The canalization effect is amplified by the presence of the resonant amount of gain, demonstrating that the frequency corresponding to the ε_{NZP} propagates through the structure as a well collimated solitary wave (soliton), with a diameter comparable to the step S of the HMM. Indeed, being S equal to 40 nm and being 426 nm the ε_{NZP} wavelength, a more than $\lambda/10$ collimation is reached. Moreover, due to the resonant gain condition, the increase of light intensity confined inside the structure is clearly visible as a well collimated, amplified soliton. Figure 6.4e and 6.4h show the case in which light propagates inside a HMM embedding a doubled amount of gain with respect to the resonant one. The behavior found with the TMM is confirmed and the light intensity propagating inside this third structure is extremely attenuated (see the cuts at the output of HMM). Then we considered a 3D nanoresonator composed by a four layer multi-shell system. As previously described, we started with a doped dielectric core of SiO_2, alternating gold shells and SiO_2 ones, ending with an *Au* metal shell (see sketch in Figure 6.1b).
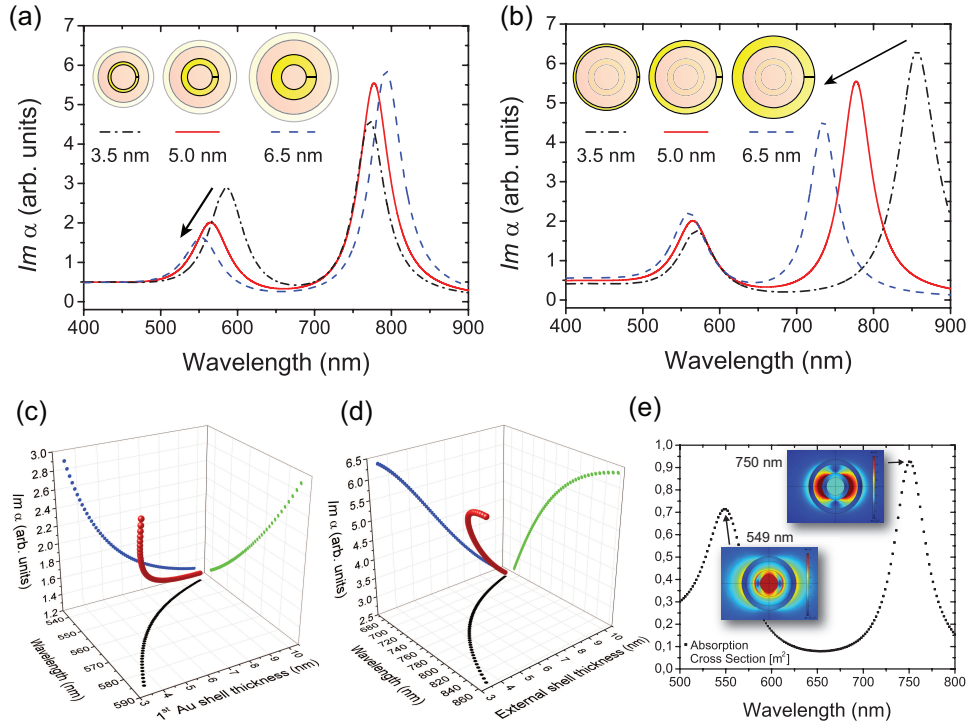
FIGURE 6.5: (a) Imaginary part of polarizability for 3 values of thickness of inner gold shell. (b) imaginary part of polarizability for 3 values of thickness of external gold shell (c) red curve is the plot of the imaginary part of polarizability as function of wavelength and thickness of the inner gold shell and related projections. (d) red curve is the plot of the imaginary part of polarizability as function of wavelength and thickness of the external gold shell and related projections. (e) FEM calculated absorption cross section (C_{abs}) for horizontal polarization. The insets show the electric field propagation pattern demonstrating that, at the first resonance light results confined inside the core while, at the second, in the first dielectric shell.

Radii of the different layers are 10 nm (SiO_2 core), 5 nm (Au shell), 10 nm (SiO_2 shell) and 5 nm of outer Au shell. Figures 6.5a and 6.5b represent the imaginary part of the polarizability α as a function of the wavelength for a multi-shell structure with such thicknesses (solid red curve). The total radius results of 30 nm, well below the operating wavelength and, thus, validating the quasi static approximation. It is worth noting that the plasmonic behaviour of a four layer multi-shell system (without gain) has already been studied in [74] (they refer to such a system with the name of "nano-matryoshka"), where it has been demonstrated that the interaction and hybridization

of the plasmons of the two individual metal shells give rise to two plasmonic resonances. In our system, as expected, two plasmonic resonances are clearly visible: the first one is placed around 565 nm while the second peak is centred at 777 nm. In order to study the high design flexibility properties of the presented multi-shell system, we analyzed the spectral behavior of $Im(\alpha)$ by varying the thicknesses r_{in} and r_{out} of the inner (Figure 6.5a) and the outer Au shell (Figure 6.5b). In the two analysis, a thickness variation of $\pm 1.5nm$ of the interested gold shell has been applied. It has been found that a fine control of the first plasmonic resonance is achieved by slightly varying the inner gold shell, while the second resonance peak can be tuned by acting on the thickness of the outer shell. Figure 6.5a shows the shift of the first plasmon peak as a function of the inner Au shell thickness. Three different cases have been considered:

1. $r_{in} = 5nm$, being the main system (red solid curve).

2. $r_{in} = 6.5nm$ (dashed blue curve).

3. $r_{in} = 4.5nm$ (dashed-dot black curve).

The sketches are representative for the thickness variation of the inner Au shell. The good design flexibility of the first resonance peak is demonstrated, with a total wavelength red shift of about 32 nm by moving from the higher to the lower r_{in} value (see black arrow). Moreover, a three dimensional plot of the imaginary part of the polarizability ($Im(\alpha)$ on z-axis) is reported as a function of the spectral position of the resonance peak (x-axis) and the thickness of the inner gold shell (y-axis) in Figure 6.5c, showing the corresponding trends by the projections on the two x-z and y-z planes. The x-y projection represents the relation between the wavelength position of the resonance peak and the inner gold shell thickness. The variation of shell thickness ranges from 3.5 to 10nm, constituting a fast engineering tool for the design of a multi-shell system. The same behavior can be observed on the second resonance peak (around 777nm) if the thickness r_{out} of the outer gold shell is varied. In the analysis reported in Figure 6.5b, three systems have been considered:

1. $r_{out} = 5nm$, being the main system (red solid curve).

2. $r_{out} = 6.5nm$ (dashed blue curve).

3. $r_{out} = 4.5nm$ (dashed-dot black curve).

It is well evident a blue shift of about 44 nm in the case of $r_{out} = 6.5nm$, while a red shift of about 78 nm is observed for $r_{out} = 4.5nm$, demonstrating, also for the second resonance peak, a very broad tunability range. Once more, a 3D plot of $Im(\alpha)$ (z-axis) as a function of the spectral position of the resonance peak (x-axis) and the thickness of the outer gold shell (y-axis) is reported in Figure 6.5d, showing the corresponding trends by the projections on the two x-z and y-z planes. The x-y projection represents the relation between the wavelength position of the resonance peak and the external gold shell thickness. In the end, Finite Element Method (FEM) based simulations of the electric field propagation inside the structure have been carried out (for details[75]). Results are shown in Figure 6.5.e, demonstrating how in the case of the first resonance, the electric field associated to the absorption cross section C_{abs} results almost completely confined to the dielectric core, while in the case of the second resonance, the field remains confined inside the first dielectric shell. Such a result is important as it gives precious information on the interaction between light and the multishell system, practically the two resonances can, indeed, be used in two separate ways, concept that will be underlined in the applications section.

In order to study the emission properties of this multi-shell system in a resonant gain condition, a suitable dye medium (*e.g.* LDS798 by Exciton) has been embedded in the dielectric shells and modelled as expressed in eq. 6.2 (see materials and methods). Typical emission peak values for this dye range from 762 nm to 818 nm, depending on the pump source type and/or on the used solvent. Therefore, also in this analysis, the emission peak has reasonably been chosen as coinciding with the second plasmonic resonance peak ($\lambda = 777nm$) of the main multi-shell system, with
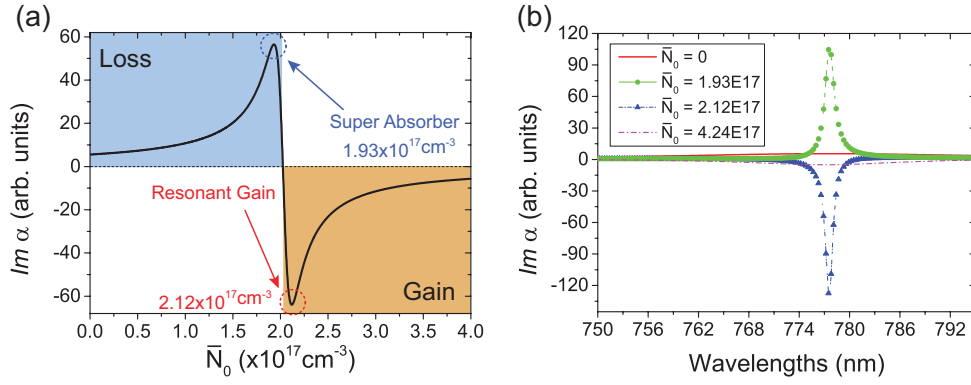
FIGURE 6.6: (a) calculated $Im(\alpha)$ as a function of the gain molecules amount showing a singularity for $\overline{N}_0 = 2.12 \times 10^{17} cm^{-3}$ molecules. (b) calculated $Im(\alpha)$ at different gain molecules concentration, as a function of the wavelength demonstrating both the resonant amplification

an emission bandwidth of about $56nm$. The resonant gain molecules amount is calculated by computing the imaginary part of α at the resonant wavelength of $\lambda = 777nm$ as a function of the gain molecules concentration $\overline{N}_0$ embedded in the SiO_2 matrix. The expected resonant behavior is illustrated in Figure 6.6a, where a resonant gain value is found for a concentration of $2.12 \times 10^{17} cm^{-3}$. Moreover, a noticeable super-absorbing behavior is detected for a gain concentration of $1.93 \times 10^{17} cm^{-3}$, value that could be used for specific applications. Four different configurations have been then considered in Figure 6.6b: the first three are referred to the original system with no gain (solid red curve), the super-absorber condition ($\overline{N}_0 = 1.93 \times 10^{17} cm^{-3}$, spline green curve) and the resonant emission condition ($\overline{N}_0 = 2.12 \times 10^{17} cm^{-3}$, dashed-dot blue curve with triangles).

As in the case of the planar multilayer configuration, also in the spherical multi-shell system it is found that by doubling the concentration of gain molecules embedded in the dielectric host, a significant lowering (in absolute value) of the imaginary part of α appears (see pink dashed-dot curve in Figure 6.6b), even if the single dye-doped dielectric shell presents an opposite gain effect. Such a behavior can be considered as lowering of the possible photons amplification inside the system.

6.3 Applications

One of the main applications of an ε_{NZP} HMM is the so called perfect lens. Its working principle has been theoretically explained and experimentally demonstrated in [45, 72] and in chapter 1. The main advantage of such a configuration is that the obtained resolution is limited only by the period of the designed HMM, making it an ideal candidate for application as single molecule imaging, deeply subwavelength laser-beam lithography, ultra-fine bio-sensing and so on. Anyway, two principal weaknesses have to be improved. The first one is inherent to the design of the ε_{NZP} HMM. Indeed, as it can be seen in equation 2.9, the sharpness of the resonance is directly connected to the amplitude of the denominator, that has to be as close as possible to zero. As shown previously, the RG-ε_{NZP} HMM configuration intrinsically solves the problem, providing an almost zero denominator, thus optimizing the collimation performances of the perfect lens. The second issue is inherent to the losses. A perfect lens based on a classic ε_{NZP} HMM introduces losses by definition, thus providing a limitation to the amount of light intensity detectable at the exit of the device. The amplification properties of the RG-ε_{NZP} HMM reveal once more useful and automatically fix this limitation. Figure 6.7 shows two simulated Amplifying Perfect Lenses (APLs), based respectively on the 12 and the 24 bilayers RG-ε_{NZP} HMM designed above. Three deeply subwavelength polymer (PMMA) elements are designed on the top of the structures. Illuminating at the ε_{NZP} wavelength (canalization wavelength), the three elements are clearly detectable at the exit of the RG-ε_{NZP} HMM. A comparison between a classic, non doped, perfect lens (Figure 6.7a for the 12 bilayers HMM and 6.7b for the 24 bilayers), the RG-ε_{NZP} version (Figure 6.7c for the 12 bilayers HMM and 6.7d for the 24 bilayers) and overdoped ε_{NZP} HMM (Figure 6.7e for the 12 bilayers HMM and 6.7f for the 24 bilayers) is reported, evidencing an increase of the output light intensity in the case of both the 12 and 24 bilayers APL with respect to both the classic ε_{NZP} HMM and the overdoped one. As expressed in the 1D nanoresonator section, the double-doped HMM undergoes a
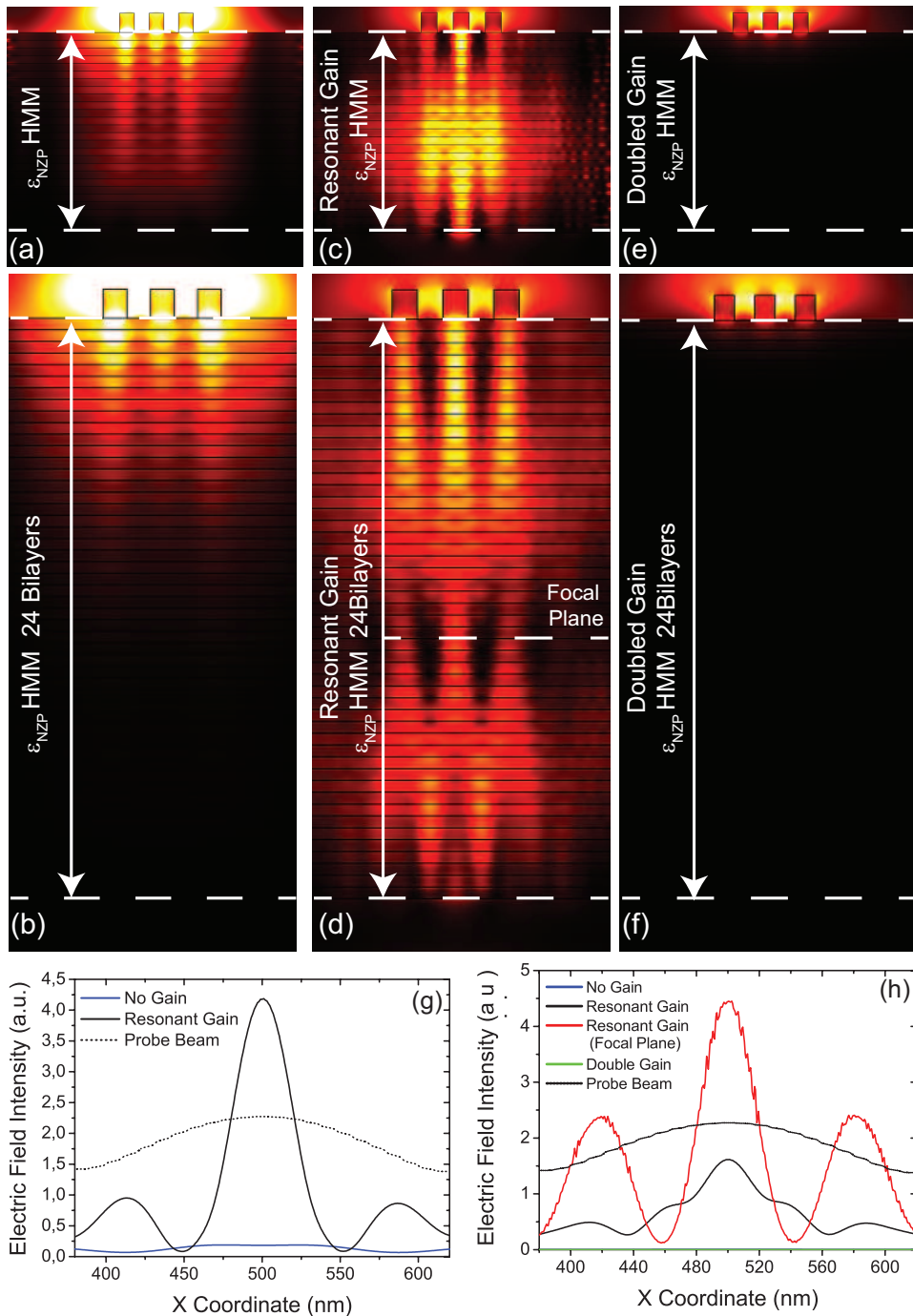
FIGURE 6.7: FEM based simulations of the electric field propagation pattern inside the 12 bilayers HMM in the case of (a) passive, undoped ε_{NZP} HMM, (c) RG ε_{NZP} HMM and (e) overdoped ε_{NZP} HMM. FEM based simulations of the electric field propagation pattern inside the 24 bilayers HMM in the case of (b) passive, undoped ε_{NZP} HMM, (d) RG ε_{NZP} HMM and (f) overdoped ε_{NZP} HMM. X-Coordinate cuts showing the electric field detected at the the exit layer of the (g) 12 bilayers and (h) 24 bilayers configurations.
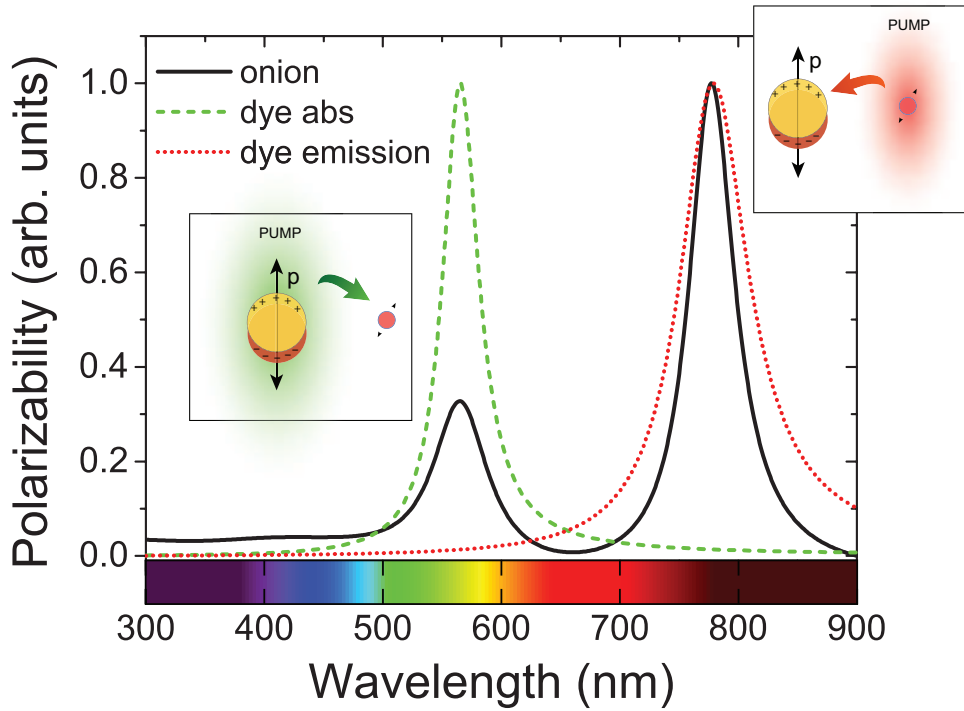
FIGURE 6.8: A sketch illustrating the Self Enhanced Loss Compensation (SELC) effect, achievable by means of the dual resonating nanoshell, being a promising configuration towards the SPASER effect.

topological transition, switching from a *type II* to an *effective metal* HMM. Such a transition leads the HMM to be extremely reflective and, as a consequence, the field inside the structure results extremely attenuated. X-coordinate cuts took at the exit layer of the HMM for the 12 bilayers HMM (Figure 6.7g) and for the 24 bilayers (Figure 6.7h) confirm this phenomenon. Moreover, it has been demonstrated in [13] that a classic HMM can focus a parallel light rays bundle inside the structure. Such a property can be find also in the proposed 24 bilayers APL. Exactly in the middle a focal plane can be identified, in which, not only the three nanometric elements posed on the top of the RG-ε_{NZP} HMM are perfectly resolved, but all of them result amplified with respect to the pump beam (see Figure 6.7g). In case of 3D nanoresonators, we can conceive a framework in which the system itself exploits its "nano-antenna" behavior [76, 77, 78, 79] to self enhance the "loss-compensation" properties.[80, 81] Indeed, the most interesting properties are showed by the simultaneous achievement of both the effects due to presence of two plasmonic resonances, with the possibility

of a spectral centerline fine tuning, thus leading to a self enhanced loss compensating (SELC) system (see Figure 6.8). If an external pump beam centred on the first plasmonic resonance is considered, an enhancement of the absorbed field confined inside the dielectric core can be achieved. By choosing the gain material absorption well overlapped with this resonance, an enhancement of the overall absorption can be induced, automatically improving the gain material emission response. At the same time, if the emission band of the selected dye is chosen in order to overlap the second plasmonic resonance, an overcompensation of the ohmic losses can be achieved, representing the fundamental requirement for a SPASER (Surface Plasmon Amplification by Stimulated Emission of Radiation) effect.[80, 81] Then, the capability to design nanostructures presenting two separate plasmonic resonances, with the possibility of a fine tuning of both the centerlines, could allow to have the best of two configurations, permitting the design of an optimized SPASER structure which can operate at very low pump powers, broadening the application range of such structures.

Figure 6.7i represents a sketch reporting the SELC system with the proper amount of gain material in the dielectric shells, presenting two distinct plasmonic resonances (see black curve) and gain absorption and emission bands well overlapped with the two resonances, respectively. The sketch shows the effect of this overlapping in producing contemporary a nano-antenna behavior in correspondence of the first plasmonic peak (green dashed curve) and a loss-compensation effect, towards a SPASER behavior, in correspondence to the second resonance (see red-dot curve in the NIR).

6.4 Materials and methods

6.4.1 Metal permittivity

In order to describe the permittivity ε_m of the metals, we used an interpolation of the experimental data we acquired by means of ellipsometric measures directly on 20

nm thick gold and silver layers we deposited by a classic DC sputtering technique. The so obtained refractive indices are plotted in Figure 6.9a and 6.9b and are the ones used in both the design and simulation process. Such a procedure ensures the design of the HMM to lie in a framework of experimental feasibility. When designing an HMM, a simple "free electron" Drude model fails to consider many crucial phenomena responsible for a drastic deviation of the real dielectric permittivity from the predicted one. One common example is that one of the effect of bound electrons,[33] whose crucial contribution to the Au dielectric permittivity is completely neglected in a simple free electron Drude model. A first improvement can be brought by adding a corrective parameter in the classic Drude model, taking into account the bound electrons resonant frequency. Anyway, even in this case, it has been demonstrated [33] that the theory still roughly fails to predict the optical parameters of the metal layers. Moreover, the interaction between light and nanometric metal layers has to be further improved due to the size effects. This is the reason why using the standard Johnson and Christy dataset can result in a slight modification of the optical constants values. The spectral and angular radiation properties of gold-silica-gold multilayer nanoshells are well described using extensions of Mie's theory for concentric multilayer spheres,[82, 83] the long wavelength approximation [84] or also the hybridization model of plasmons supported by metallic nanostructures quite similar to the molecular orbital hybridization.[74] This classical approach is valid until the nanomatryoshka shell thickness does not become sub-nanometric, when a quantum approach is necessary,[85] therefore in our case, assuming experimentally obtained data constitutes the most accurate choice.

6.4.2 Gain media permittivity

In presence of a gain material embedded in a dielectric layer, the overall resulting composite medium must be described in terms of homogenized effective permittivity. The approach we followed is reported in,[63] in which the gain material, made of
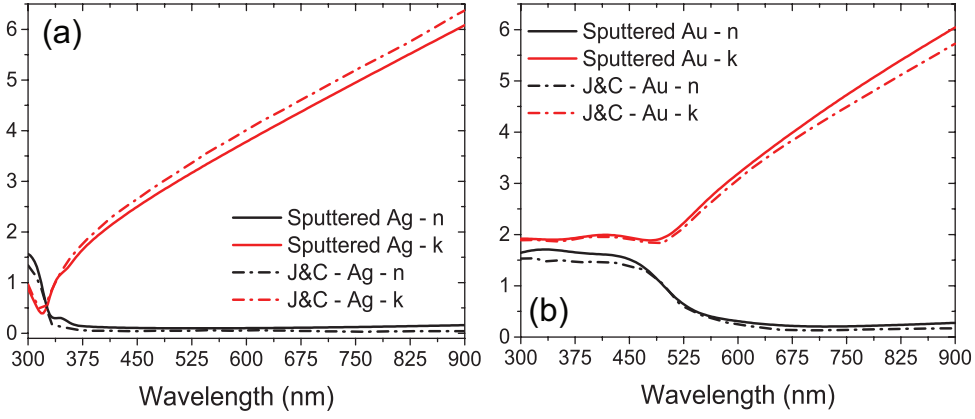
FIGURE 6.9: Ellipsometrically measured refractive index of (a) a 20
nm Ag layer and (b) a 20 nm Au layer, compared to the well known
Johnson and Christy dataset (dash-dotted curves)

fluorescent dye molecules, is associated with a four levels atomic system. Then, the
obtained real and imaginary parts of the optical constants are given by the following
relation:

$$\varepsilon_g = \varepsilon_0 \varepsilon_r + \frac{\sigma_a}{\omega^2 + i\Delta\omega_a\omega - \omega_a^2} \frac{(\tau_{21} - \tau_{10})\Gamma_{pump}}{1 + (\tau_{32} + \tau_{21} + \tau_{10})\Gamma_{pump}} \overline{N}_0 \qquad (6.2)$$

where ω is the angular frequency, ω_a is the emitting angular frequency, $\Delta\omega_a$ is the
bandwidth of the dye transition, ε_0 is the vacuum dielectric permittivity, $\varepsilon_r(\omega)$ is the
frequency dependent complex permittivity of the host dielectric and σ_a is a coupling
strength parameter (see [86]). $\overline{N}_0$ represents the total dye concentration expressed as
$\overline{N}_0 = N_0(r) + N_1(r) + N_2(r) + N_3(r)$, being $N_{i_{th}}$ the occupation density of the i_{th} state,
whereas Γ_{pump} the pump rate and $\tau_{i+1;i}$ the relaxation time during the $(i+1)_{th}$ to i_{th}
state transition. In our case, the following values have been considered:

- $\lambda = 2\pi c/\omega$ spanning from 300nm to 900nm, the enlarged UV-NIR range

- $\lambda_a = 2\pi c/\omega_a = 426nm$ (HMM) or 777nm (multi-shell) (possible organic dyes
  could be Coumarin 500 for HMM and LDS798 for multishell, both by Exciton)

- $\Delta\omega_a = 2\pi\Delta v_a = 2\pi c\Delta\lambda_a/\lambda_a^2 = 207.7$ THz (with $\Delta\lambda_a = 20nm$ in the case of
  C500), and 62 THz (with $\Delta\lambda_a = 56nm$ in the case of LDS798)

- $\sigma_a = 6\pi\varepsilon_0 c^3 \frac{\eta}{(\tau_{21}\omega_a^2 \sqrt{\varepsilon_r})} [C^2/kg]$.

- $\eta = 0.78$ (C500) and 0.48 (LDS798), is the Quantum Yield of the dye.

- $\tau_{10} = \tau_{32} = 100 fs$.

- $\tau_{21} = 110$ ps (C500) or 50 ps (LDS798).

- $\Gamma_{pump} = \frac{\sigma_{abs}I}{hf} s^{-1}$, where h is the Planck constant.

The intensity I is expressed as $I = \frac{P}{A} = \frac{E}{\tau_{pulse}A}$, in which the pump energy E and the repetition rate are referred to a modelocked Ti:Sapphire pulsed laser and results to be $E = 10\mu J$ and $f = 80MHz$. The pumped surface A is equal to πr^2 with $r = 2mm$, typical of an unfocused pump beam. The pump rate Γ_{pump} directly depends on the absorption cross section of the proposed dyes, that can be recovered in [86] and results to be $\sigma_{abs} = \frac{\gamma_{rad}\lambda_a^2}{2\pi\Delta\omega_a}$, depending on the radiative decay rate $\gamma_{rad} = \frac{\eta}{\tau_{21}}$ from level 2 to level 1. Therefore, the values of η and τ_{21} turn to be of crucial importance in the selection of the suitable dyes. In particular, it will be shown later that a lower concentration $\overline{N}_0$ of dye molecules can be used to reach the singularity if faster τ_{21} and/or higher η are adopted, that means more performing media. For Coumarin 500 dye embedded in a HMM multilayer, a typical value for τ_{21} is around 110 ps while η is about 0.78. The number $\overline{N}_0$ of dye molecules necessary to reach the gain singularity results in this case $6.1 \times 10^{18} cm^{-3}$, a value that is comparable with the most widely reported in literature. It is worth saying that the specific property of an HMM to speed up the decay rate of closely placed dye molecules has been demonstrated elsewhere.[31, 44] In particular, the possibility of reaching τ_{21} of 75 ps has been reported in [61] if the dye molecules are embedded in the dielectric layers of an HMM. Such value shows that the condition we consider here constitutes an upper limit for τ_{21}, so that even lower singular concentrations can be reasonably expected, improving the feasibility of the presented device. Furthermore, it has to be noted that, even though we described a feasible scenario for these two specific dyes, choosing different and more performing dyes is possible, since the conditions to be fulfilled in

order to obtain the gain singularities in both the two systems, does not depend on the specifically selected dye. In the end, while this model for the gain materials is largely used,[47, 48, 63, 87, 88] it is worth underlining that equation 6.2 is a steady state description and, consequently, results obtained in this regime have to be supported by a more detailed time-dependent analysis, that would eventually clarify the behaviour of the proposed systems as soon as the emission/amplification/SPASER regime is reached. Nonetheless, it has been demonstrated in ref. [49] that it works perfectly until the emission threshold is approached, allowing to predict the conditions and the critical gain amount for which this regime will occur.

6.5 Conclusion

In this chapter we demonstrate a resonant gain behavior in metal/dielectric multi-folded nanostructures. Following two different approaches, we demonstrate that the two architectures lead to the same results. A gain singularity is detectable both in the planar 1D nanoresonator and in the 3D spherical multishell one. As expected, this condition is fulfilled only for a specific amount of gain molecules, before which, a super absorber condition is found in both systems.

In the 1D HMM system the so called ε_{NZP} regime is demonstrated to be necessary to observe the typical confinement behavior and the collimation used to obtain the resonant gain behavior. Such a condition is responsible for the super-collimation effect through the HMM structure and poses the most favourable basis for a perfect directionality of the emitted light. EMT has been used to determine, as a first step, the ε_{NZP} wavelength and, consequently, to calculate resonant gain amount and to show the gain singularity appearing only for that specific gain molecules density. By means of a TMM based simulation, it has been demonstrated how the HMM itself behaves as a self sustained cavity, showing that an optimum number of bilayers is required in order to obtain a noticeable enhancement of the emitted light. TMM

confirms that doping the dielectric layers above the resonant amount, brings to a lowering of the emission properties. Furthermore, FEM based simulations confirm the supercollimation effect, as well as both the significant enhancement of the emitted light obtainable in the resonant gain condition. In the end, it has been reported the design and the simulation of an Amplifying Perfect Lens based on the RG-ε_{NZP} HMM, exploiting all of the extreme optical characteristics of the resonant amplification.

The investigation has been then moved on the 3D multishell structure and, more precisely, on the behavior of its effective polarizability α, being this quantity directly ascribable to the overall ε. The adoption of a metal/doped dielectric multishell configuration gives rise to a dual resonant system, showing two different plasmonic resonances. Such a system is, in principle, capable to work as and exploit the benefits of the two main typical behaviors, the "nano-antenna" and the loss-compensated "nano-emitter". This two features can be effectively exploited to reach a Self Enhanced Loss Compensating system. It has been demonstrated how it is possible to finely select the resonance wavelengths only by acting on the thickness of one of the two metal shells. A resonant gain behaviour is detected in correspondence of one of the these two plasmonic resonances, but only for a specific amount of gain molecules embedded in the dielectric shells.

The appearing of a resonance gain singularity in both systems, for a specific amount of gain identifies the threshold between the absorbing and the emissive regimes, representing an easy way to calculate the minimal molecular density to be included in these structures to achieve amplification. The occurring of the same resonant phenomenon in two different and complementary systems is of noticeable importance in all of those fields in which nano laser sources are required, since it allows to have both planar, self collimated nano-lasers and spherical, dispersable, nano-sources, making the proposed systems ideal candidates for 1D and 3D SPASER devices.

Appendix A

Simulation Codes

A.1 Effective Medium Theory

Effective Medium Theory based design of all of the proposed nanostructures has
been performed by means of the following Matlab code:

```
close all;
clc;
clear all;


%————————————————————————————————————————————————
%————————Input Parameters————————————————————————
%————————————————————————————————————————————————


[metal_name] = uigetfile('*.txt','Select the metal file name');
[diel_name] = uigetfile('*.txt','Select the dielectric file name');


prompt = { 'Thickness of metal layer (nm)'
           'Thickness of dielectric layer (nm)'};


title  = 'Insert material parameters';
```

```matlab
lines = 1;
def      = {'',''};
answer   = inputdlg(prompt, title, lines, def);
metal_thick = str2num(answer{1});
diel_thick = str2num(answer{2});


%-------Imports Metal and Dielectric Parameters---------

metal  = importdata(metal_name);
wavelengths = metal(:,1);
n_Metal = metal(:,2);
k_Metal = metal(:,3);
eps_metal  = (n_Metal - 1i*k_Metal).^2;
%Calculates real and imaginary part of metal epsilon.

diel  = importdata(diel_name);
n_Diel = diel(:,2);
k_Diel = diel(:,3);
eps_diel  = (n_Diel - 1i*k_Diel).^2;
%Calculates real and imaginary part of metal epsilon.


e1_diel = real(eps_diel);
e2_diel = imag(eps_diel);


%--------Calculates the Step and the Maximum Wavelength -----

step_metal = metal(2,1) - metal(1,1)
```

```
wave_max_metal = max( metal (: ,1));

step_diel = diel (2,1) − diel (1 ,1)

wave_max_diel = max( diel (: ,1));


length=size ( metal (: ,1));
% eps_parallel=zeros ( length );


%———— Verifies the sizes of the input files ————


if step_metal ~= step_diel
    error ('The steps of the optical constants files ...
                you inserted are not the same ');
end


if wave_max_metal ~= wave_max_diel
    error ('Maximum wavelengths are not the same ');
end


%———— Calculates Effective Medium Parameters ————


for s = 1:1: length

    eps_parallel(s) =(( eps_diel (s)* diel_thick )+...
    ( eps_metal (s)* metal_thick ))/( diel_thick+metal_thick );
    eps_perpendicular(s) = ( eps_diel (s)* eps_metal (s )*...
    ( diel_thick+metal_thick ))/(( diel_thick * eps_metal (s ))+...
    ( metal_thick * eps_diel (s )));
```

```
end


eps_parallel =  transpose(eps_parallel);

eps_perpendicular =  transpose(eps_perpendicular);

re_eps_par=real(eps_parallel);

im_eps_par=−imag(eps_parallel);

re_eps_perp=real(eps_perpendicular);

im_eps_perp=−imag(eps_perpendicular);




figure (1)

plotyy(wavelengths,real(eps_parallel),wavelengths,...

real(eps_perpendicular));

figure (2)

plotyy(wavelengths,−imag(eps_parallel),wavelengths,...

−imag(eps_perpendicular));


EMA_real = [wavelengths,  real(eps_parallel),...

 real(eps_perpendicular)];

EMA_imag = [wavelengths,  −imag(eps_parallel),...

 −imag(eps_perpendicular)];
```

In order the HMM design to be as much close as possible to the reality, the considered optical constants are those ones belonging to the effectively used layers, ellipsometrically measured.

A.2 Scattering and Transfer Matrix Method

In order to simulate the transmission and reflection behaviour of the designed and realized HMMs, a classic Transfer/Scattering Matrix Method (SMM and TMM) has been set up. The following code automatically returns both the transmission and reflection response of the sample, taking in consideration Air as an incoming medium and Glass as an outgoing one. Refractive indices of the considered layers, together with the glass ones have been directly ellipsometrically measured.

```
close all;
clc;
clear all;


% ———————— Input parameters ——————————
[metal_name] = uigetfile('*.txt','Select the metal file name');
[diel_name] = uigetfile('*.txt','Select the dielectric file name');
[glass_n_k] = uigetfile('*.txt','Select the glass (n_&_k) file name');

prompt = {'Number of bilayers',
    'Incident angle (in degree with respect to normal at //
     the substrate)'
    'Amplitude of TM polarization (0 or 1) corresponding to p−pol'
    'Amplitude of TE polarization (0 or 1) corresponding to s−pol'
    'Thickness of metal layer (nm)'
    'Thickness of dielectric layer (nm)'};
title   = 'Insert material parameters';
lines= 1;
def     = {'','','1','0','25','20'};
answer  = inputdlg(prompt,title,lines,def);
```

```
n_bilayers = str2num(answer{1});

incident_angle = str2num(answer{2});

TM_amp = str2num(answer{3});

TE_amp = str2num(answer{4});

metal_thick = str2num(answer {5});

diel_thick = str2num(answer {6});

bilayers = str2num(answer{1});
% ———————————— Input parameters end ————————————


%%%———————————— Start to import data from files (metal, //
%%%———————dielectric and glass) containing n & k for
%%%———————————— metal, dielectric and glass.
%%% The files are supposed to possess the same step //
%%% in wavelength (1, 3 or 5nm) //
%%% and all three columns (wavelength, n & k)


Ag = importdata(metal_name);
nAg = Ag(:,2);
kAg = Ag(:,3);


first_wave = Ag (1,1); %Read the first wavelength in nm
step = Ag (2,1)− Ag (1,1); %Calculate the step in nanometers
max_wave = (max (Ag (:,1))− min (Ag(:,1)))/step;
%Calculate the number of %wavelengths in the file


epgarray = (nAg − 1i∗kAg).^2;
%Calculates real and imaginary part of metal epsilon.
```

```matlab
ITO = importdata(diel_name);
nITO = ITO(:,2);
kITO = ITO(:,3);
epITO = (nITO - 1i*kITO).^2;
%Calculates real and imaginary part of dielectric epsilon.


glass = importdata(glass_n_k);
n_glass = glass(:,2);
k_glass = glass(:,3);
eps_glass = (n_glass - 1i*k_glass).^2;
%Calculates real and imaginary part of glass epsilon.



% UNITS
degrees = pi/180;


%————————————————————————————————————————————————————
%% DEFINE SIMULATION PARAMETERS
%————————————————————————————————————————————————————


for N = 2:2:(bilayers*2) %Loop on the number of layers


for Y = 1:1:max_wave+1
    % SOURCE PARAMETERS
    lam0(Y) = ((first_wave-step)+step*Y) * 10^-9;
    %free space wavelength
```

```
c       = 3 * 10^8;
w       = (2*pi*c)/lam0(Y);


%%Ag
epg  =  epgarray(Y);
%%air
ep0     = 1;
%%ITO
ep2     = epITO(Y);


k0=(2*pi)/lam0(Y);
theta = str2num(answer{2}) * degrees; %incident angle
phi = 0 * degrees; %azimuthal angle
ptm = str2num(answer{3}); %amplitude of TM polarization
pte = str2num(answer{4}); %amplitude of TE polarization
ni=1.0; % incident medium refractive index


% EXTERNAL MATERIALS
ur1 = 1.0; % permeability in the reflection region
er1 = 1.0; % permittivity in the reflection region
ur2 = 1.0; % permeability in the transmission region
%er2 = 1.0; % permittivity in the transmission region


er2  =  eps_glass(Y);
% Takes into account the glass as the exiting layer.



dg = str2num(answer{5}); %Metal thickness in nm
```

```
dA = str2num(answer{6}); %Dielectric thickness in nm
% DEFINE LAYERS


ER_base = [epg , ep2]; % array of permittivities in each layer
ER = repmat (ER_base, 1,N−1);
% repeat the array of permittivities for the numbers of bilayers
UR = ones (1,N); % array of permeabilities in each layer


L_base = [dg , dA].∗1e−9; % array of the %thickness of each layer
L = repmat (L_base,1,N−1);
%repeat the array of thicknesses for the numbers of bilayers



%————————————————————————————————————————————————
% IMPLEMENT TRANSFER MATRIX METHOD
%————————————————————————————————————————————————


Kx=ni∗sin(theta)∗cos(phi);
Ky=ni∗sin(theta)∗sin(phi);
Kzh=1+(Kx∗Kx)+(Ky∗Ky);


%————————————————————————————————————————————————
%——homogenous gap layer parameters
%————————————————————————————————————————————————


Wh=eye(2);
Qh=[ Kx∗Ky  1−(Kx∗Kx)  ;(Ky∗Ky)−1   −Kx∗Ky];
Omh=1i∗Kzh∗eye(2);
```

```
Vh=Qh*(Omh^−1);


    %−−initialize  global  scattering  matrix


    Sg11=zeros(2,2); Sg12=eye(2);Sg21=eye(2);Sg22=zeros(2,2);


    %−−−−−−−−−−−−−−−−−−−−−−−−−−−−−−−−−−−−−−−−−−−−−−−−−−
    % Reflection side−−−−−−−−−−−−−−−−−−−−−−−−−−−−−−−−−−
    %−−−−−−−−−−−−−−−−−−−−−−−−−−−−−−−−−−−−−−−−−−−−−−−−−−


    Krz=sqrt(ur1*er1 −(Kx*Kx)−(Ky*Ky));
    Pr=(1/er1)*[ Kx*Ky ur1*er1 −(Kx*Kx)  ;(Ky*Ky)−ur1*er1
−Kx*Ky];
    Qr=(1/ur1)*[ Kx*Ky ur1*er1 −(Kx*Kx)  ;(Ky*Ky)−ur1*er1
−Kx*Ky];
    Omr=1i*Krz*eye(2);
    Wr= eye(2);
    Vr=Qr*(Omr^−1);
    Ar=eye(2)+(Vh^−1)*Vr;
    Br=eye(2)−(Vh^−1)*Vr;


    Sref11=−(Ar^−1)*Br;
    Sref12=2*eye(2)*(Ar^−1);
    Sref21=0.5*eye(2)*(Ar−(Br*(Ar^−1)*Br));
    Sref22=Br*(Ar^−1);


% updating  global  scattering  matrices  by  Redheffer  star  product
```

```
SA11=Sref11 ;

SA12=Sref12 ;

SA21=Sref21 ;

SA22=Sref22 ;


SB11=Sg11 ;

SB12=Sg12 ;

SB21=Sg21 ;

SB22=Sg22 ;


SAB11=SA11+(SA12 *(( eye (2) −(SB11*SA22))^ −1)*SB11*SA21 );

SAB12=SA12 *(( eye (2) −(SB11*SA22))^ −1)*SB12 ;

SAB21=SB21 *(( eye (2) −(SA22*SB11))^ −1)*SA21 ;

SAB22=SB22+(SB21 *(( eye (2) −(SA22*SB11))^ −1)*SA22*SB12 );


Sg11=SAB11 ;

Sg12=SAB12 ;

Sg21=SAB21 ;

Sg22=SAB22 ;




%−−−updating  the  scattering  matrices  for  N  layers −−−−−−−


for  i =1:N

    Kz=sqrt (UR( i )*ER( i )−(Kx*Kx)−(Ky*Ky ));

    Q=(1/UR( i ))*[  Kx*Ky  UR( i )*ER( i )−(Kx*Kx)  ;
```

```
(Ky*Ky)−UR( i )∗ER( i )    −Kx∗Ky ] ;
Om=1 i ∗Kz∗eye ( 2 ) ;
V=Q∗(Om^ − 1);
A=eye ( 2 )+((V^ − 1)∗Vh ) ;
B=eye ( 2 ) − ((V^ − 1)∗Vh ) ;
X=expm(−Om∗k0∗L( i ) ) ;
S11 = ( ( A−((X∗B∗(A^ − 1)∗X∗B) ) )^ − 1 )∗( ( X∗B∗(A^ − 1)∗X∗A)−B)  ;
S22=S11 ;
S12 = ( ( ( A−((X∗(B/A)∗X∗B) ) )^ − 1 )∗X)∗(A–B∗(A^ − 1)∗B ) ;
S21=S12 ;


% updating  global  scattering  matrices  by  Redheffer  star  product


SA11=Sg11 ;
SA12=Sg12 ;
SA21=Sg21 ;
SA22=Sg22 ;


SB11=S11 ;
SB12=S12 ;
SB21=S21 ;
SB22=S22 ;


SAB11=SA11+(SA12 ∗ ( ( eye ( 2 ) −(SB11∗SA22))^ − 1 )∗SB11∗SA21 ) ;
SAB12=SA12 ∗ ( ( eye ( 2 ) −(SB11∗SA22))^ − 1 )∗SB12 ;
SAB21=SB21 ∗ ( ( eye ( 2 ) −(SA22∗SB11))^ − 1 )∗SA21 ;
SAB22=SB22+(SB21 ∗ ( ( eye ( 2 ) −(SA22∗SB11))^ − 1 )∗SA22∗SB12 ) ;
```

```
          Sg11=SAB11;

          Sg12=SAB12;

          Sg21=SAB21;

          Sg22=SAB22;

     end




%————————————————————————————————————

% Transmission side—————————————————————————

%————————————————————————————————————



     Ktz=sqrt(ur2.*er2−(Kx*Kx)−(Ky*Ky));

     Pt=(1/er2)*[ Kx*Ky  ur2.*er2−(Kx*Kx)  ;(Ky*Ky)−ur2.*er2
−Kx*Ky];

     Qt=(1/ur2)*[ Kx*Ky  ur2.*er2−(Kx*Kx)  ;(Ky*Ky)−ur2.*er2
−Kx*Ky];

     Omt=1i*Ktz*eye(2);

     Wt=eye(2);

     Vt=Qt*(Omt^−1);

     At=eye(2)+(Vh^−1)*Vt;

     Bt=eye(2)−(Vh^−1)*Vt;



     St11=Bt*(At^−1);

     St12=0.5*eye(2)*(At−(Bt*(At^−1)*Bt));

     St21=2*(At^−1);

     St22=−(At^−1)*Bt;


% updating global scattering matrices by Redheffer star product
```

```
SA11=Sg11 ;
SA12=Sg12 ;
SA21=Sg21 ;
SA22=Sg22 ;


SB11=St11 ;
SB12=St12 ;
SB21=St21 ;
SB22=St22 ;


SAB11=SA11+(SA12 *(( eye (2) −(SB11*SA22))^ −1)*SB11*SA21 );
SAB12=SA12 *(( eye (2) −(SB11*SA22))^ −1)*SB12 ;
SAB21=SB21 *(( eye (2) −(SA22*SB11))^ −1)*SA21 ;
SAB22=SB22+(SB21 *(( eye (2) −(SA22*SB11))^ −1)*SA22*SB12 );


Sf11 =SAB11 ;
Sf12 =SAB12 ;
Sf21 =SAB21 ;
Sf22 =SAB22 ;




Kinc=k0 * ni *[ sin ( theta )* cos ( phi )  sin ( theta )* sin ( phi )  cos ( theta )];
    nsn =[0  0  −1]; % surface  normal


    if  ( theta ==0)
        aTE =[0  1  0];
```

```
else
    aTE=cross(Kinc,nsn)./norm(cross(Kinc,nsn));
end


aTM=cross(aTE,Kinc)./norm(cross(aTE,Kinc));


P=pte*aTE+ptm*aTM;


cinc=[P(1); P(2)];
Er=Sf11*cinc;
Et=Sf21*cinc;
Erx=Er(1);
Ery=Er(2);
Etx=Et(1);
Ety=Et(2);


Erz=-(Kx*Erx+Ky*Ery)/Krz;
Etz=-(Kx*Etx+Ky*Ety)/Ktz;


Er=[Erx;Ery;Erz];
Et=[Etx;Ety;Etz];


R=abs(Erx)^2+abs(Ery)^2+abs(Erz)^2;
T=(abs(Etx)^2+abs(Ety)^2+abs(Etz)^2)*real((ur1*Ktz)/(ur2*Krz));


Tx(Y,N/2)=abs(T);
Rx(Y,N/2)=abs(R);
```

```
end
prova1 = N/2;
prova2 = N/2;
hold all
figure(1)
plot (lam0,Tx(:,N/2), 'DisplayName', ['bilayer-' num2str(prova1)])

xlabel('\lambda','fontsize',20)
ylabel('Transmittance','fontsize',20)
absorption=1-(Rx+Tx);

hold all
figure(2)
plot(lam0,Rx(:,N/2), 'DisplayName', ['bilayer-' num2str(prova2)])
xlabel('\lambda','fontsize',20)
ylabel('Reflectance','fontsize',20)

figure(3)
plot(lam0,1-(Rx(:,N/2)+Tx(:,N/2)))

% hold on


end
%%————————————————————————
%% ——————————— Plots ———————————
legend show
```

```
lam0 = transpose (lam0);
T_total = [lam0,Tx];
%generates a matrix of trasmission including wavelengths
R_total = [lam0,Rx];
%generates a matrix of reflection including wavelengths



fh1 = figure (1);
set(fh1, 'color', 'white');
fh2 = figure (2);
set(fh2, 'color', 'white');
%————————————————————————————————————————
```

A.3 Brewster Angle Code

In order to calculate and simulate the Brewster angle of the analyzed HMMs, a specific code has been set up. Indeed it constitutes a variation of the previews SMM code, in which the wavelength is fixed at the one chosen by the user and spans the degrees.

```
close all;
clc;
clear all;


% ————————————— Input parameters ————————————
[metal_name] = uigetfile ('*.txt','Select the //
metal file name');
[diel_name] = uigetfile ('*.txt','Select the //
```

```
dielectric file name');
[glass_n_k] = uigetfile('*.txt','Select the glass //
(n_&_k) file name');

prompt  = {'Number of bilayers',
 'Incident angle (in degree with respect to //
 the normal at the substrate)'
 'Amplitude of TM polarization (0 or 1) corresponding to p-pol'
 'Amplitude of TE polarization (0 or 1) corresponding to s-pol'
 'Thickness of metal layer (nm)'
 'Thickness of dielectric layer (nm)'
 'Lambda (nm)'
 'angolo minimo(deg - NON METTERE ZERO)'
 'angolo massimo(deg - FINO A 90Âř)'
 };

title    = 'Insert material parameters';
lines= 1;
def      = {'5','50','1','0','20','20','341','20','84'};
answer   = inputdlg(prompt,title,lines,def);

n_bilayers = str2num(answer{1});
incident_angle = str2num(answer{2});
TM_amp = str2num(answer{3});
TE_amp = str2num(answer{4});
metal_thick = str2num(answer {5});
diel_thick = str2num(answer {6});
bilayers = str2num(answer{1});
```

```matlab
lambda = str2num(answer{7});
ang_min = str2num(answer{8});
ang_max = str2num(answer{9});
ang_step = 1;
% ——————————— Input parameters end ———————————


%%%——— Start to import data from files
%%%———(metal, dielectric and glass) containing n & k for
%%%——— metal, dielectric and glass
%%%% We are supposing that the three files possess the same step
%%%% in wavelength (1, 3 or 5nm)
%%%% and all three columns (wavelength, n & k)


Ag  = importdata(metal_name);
nAg = Ag(:,2);
kAg = Ag(:,3);


first_wave = Ag(1,1); %Read the first wavelength in nm
step = Ag(2,1)− Ag(1,1); %Calculate the step in nanometers
max_wave = (max(Ag(:,1))− min(Ag(:,1)))/step;
%Calculate the number of wavelengths present in the file
%(it has to be equal in all files)
epgarray  = (nAg − 1i∗kAg).^2;
%Calculates real and imaginary part of metal epsilon.


ITO = importdata(diel_name);
nITO = ITO(:,2);
kITO = ITO(:,3);
```

```matlab
epITO = (nITO − 1i*kITO).^2;
%Calculates real and imaginary part of dielectric epsilon.


 glass = importdata(glass_n_k);
 n_glass = glass(:,2);
 k_glass = glass(:,3);
 eps_glass = (n_glass − 1i*k_glass).^2;
%Calculates real and imaginary part of glass epsilon.
Y=lambda−299;


 lam0 = lambda * 10^−9;%free space wavelength
 c    = 3 * 10^8;
 w    = (2*pi*c)/lam0;
 index=round((lambda−299)/step);
%%Ag
    epg = epgarray(index);
%%air
    ep0    = 1;
%%ITO
    ep2    = epITO(index);


k0=(2*pi)/lam0;


% UNITS
degrees = pi/180;
phi = 0 * degrees; %azimuthal angle
ptm = str2num(answer{3}); %amplitude of TM polarization
pte = str2num(answer{4}); %amplitude of TE polarization
```

```
ni =1.0; % incident medium refractive index


% EXTERNAL MATERIALS
    ur1 = 1.0; % permeability in the reflection region
    er1 = 1.0; % permittivity in the reflection region
    ur2 = 1.0; % permeability in the transmission region
    %er2 = 1.0; % permittivity in the transmission region


    er2 = eps_glass(index);
    % Takes into account the glass as the exiting layer.



dg = str2num(answer{5}); %Metal thickness in nm
dA = str2num(answer{6}); %Dielectric thickness in nm




%————————————————————————————————————————————————————
%% DEFINE SIMULATION PARAMETERS
%————————————————————————————————————————————————————


for N = 2:2:(bilayers*2) %Loop on the number of layers


    for Y = 1:1:(ang_max−ang_min)


    % DEFINE LAYERS


    ER_base = [epg , ep2];
```

```
% array of permittivities in each layer
ER = repmat (ER_base, 1,N-1);
% repeat the array of permittivities
% for the numbers of bilayers
UR = ones (1,N); % array of permeabilities in each layer


 L_base = [dg , dA].*1e-9;
%array of the %thickness of each layer
L = repmat (L_base,1,N-1);
%repeat the array of thicknesses
%for the numbers of bilayers


%————————————————————————————————————————————————————
% IMPLEMENT TRANSFER MATRIX METHOD
%————————————————————————————————————————————————————
 theta = (ang_min+Y-1)*degrees;
 Theta(Y) = (ang_min+Y-1);
Kx=ni*sin(theta)*cos(phi);
Ky=ni*sin(theta)*sin(phi);
Kzh=1+(Kx*Kx)+(Ky*Ky);


%————————————————————————————————————————————————————
%———homogenous gap layer parameters
%————————————————————————————————————————————————————


Wh=eye(2);
Qh=[ Kx*Ky 1-(Kx*Kx) ;(Ky*Ky)-1  -Kx*Ky];
Omh=1i*Kzh*eye(2);
```

```
Vh=Qh*(Omh^−1);



%−−initialize  global  scattering  matrix

Sg11=zeros (2 ,2);  Sg12=eye (2);Sg21=eye (2);Sg22=zeros (2 ,2);


%−−−−−−−−−−−−−−−−−−−−−−−−−−−−−−−−−−−−−−−−−−−−−−−−−−−−−−−−−−−−
% Reflection  side −−−−−−−−−−−−−−−−−−−−−−−−−−−−−−−−−−−−−−−−
%−−−−−−−−−−−−−−−−−−−−−−−−−−−−−−−−−−−−−−−−−−−−−−−−−−−−−−−−−−−−


Krz=sqrt ( ur1 *er1 −(Kx*Kx)−(Ky*Ky ) ) ;
Pr =(1/er1 )*[  Kx*Ky  ur1 *er1 −(Kx*Kx)  ;(Ky*Ky)−ur1 *er1
−Kx*Ky ] ;
Qr =(1/ur1 )*[  Kx*Ky  ur1 *er1 −(Kx*Kx)  ;(Ky*Ky)−ur1 *er1
−Kx*Ky ] ;
Omr=1 i *Krz *eye (2);
Wr=  eye (2);
Vr=Qr*(Omr^−1);
Ar=eye (2)+(Vh^−1)*Vr ;
Br=eye (2) −(Vh^−1)*Vr ;


Sref11=−(Ar^−1)*Br ;
Sref12 =2*eye (2)*( Ar^−1);
Sref21 =0.5*eye (2)*( Ar−(Br *(Ar^−1)*Br ) ) ;
Sref22 =Br *(Ar^−1);


% updating global scattering matrices by Redheffer star product
```

```
SA11=Sref11 ;

SA12=Sref12 ;

SA21=Sref21 ;

SA22=Sref22 ;


SB11=Sg11 ;

SB12=Sg12 ;

SB21=Sg21 ;

SB22=Sg22 ;


SAB11=SA11+(SA12*((eye(2)-(SB11*SA22))^-1)*SB11*SA21);

SAB12=SA12*((eye(2)-(SB11*SA22))^-1)*SB12;

SAB21=SB21*((eye(2)-(SA22*SB11))^-1)*SA21;

SAB22=SB22+(SB21*((eye(2)-(SA22*SB11))^-1)*SA22*SB12);


Sg11=SAB11 ;

Sg12=SAB12 ;

Sg21=SAB21 ;

Sg22=SAB22 ;




%——updating  the  scattering  matrices  for  N  layers ———

for  i =1:N

    Kz=sqrt(UR(i)*ER(i)-(Kx*Kx)-(Ky*Ky));
```

```
        Q=(1/UR(i))*[ Kx*Ky UR(i)*ER(i)−(Kx*Kx)  ;(Ky*Ky)−UR(i)*ER(i)
−Kx*Ky];

        Om=1i*Kz*eye(2);

        V=Q*(Om^−1);

        A=eye(2)+((V^−1)*Vh);

        B=eye(2)−((V^−1)*Vh);

        X=expm(−Om*k0*L(i));

        S11=((A−((X*B*(A^−1)*X*B)))^−1)*((X*B*(A^−1)*X*A)−B) ;

        S22=S11;

        S12=(((A−((X*(B/A)*X*B)))^−1)*X)*(A−B*(A^−1)*B);

        S21=S12;


% updating global scattering matrices
% by Redheffer star product


        SA11=Sg11;

        SA12=Sg12;

        SA21=Sg21;

        SA22=Sg22;


        SB11=S11;

        SB12=S12;

        SB21=S21;

        SB22=S22;


        SAB11=SA11+(SA12*((eye(2)−(SB11*SA22))^−1)*SB11*SA21);

        SAB12=SA12*((eye(2)−(SB11*SA22))^−1)*SB12;

        SAB21=SB21*((eye(2)−(SA22*SB11))^−1)*SA21;
```

```
        SAB22=SB22+(SB21 *(( eye (2) −(SA22*SB11))^ −1)*SA22*SB12 ) ;


        Sg11=SAB11 ;
        Sg12=SAB12 ;
        Sg21=SAB21 ;
        Sg22=SAB22 ;
    end




    %———————————————————————————————
    % Transmission side —————————————————————————
    %———————————————————————————————


    Ktz=sqrt ( ur2 . ∗ er2 −(Kx∗Kx) −(Ky∗Ky ) ) ;
    Pt =(1/ er2 ) ∗[ Kx∗Ky ur2 . ∗ er2 −(Kx∗Kx)  ; ( Ky∗Ky)−ur2 . ∗ er2
−Kx∗Ky ] ;
    Qt =(1/ ur2 ) ∗[ Kx∗Ky ur2 . ∗ er2 −(Kx∗Kx)  ; ( Ky∗Ky)−ur2 . ∗ er2
−Kx∗Ky ] ;
    Omt=1 i ∗Ktz∗eye (2) ;
    Wt=eye (2) ;
    Vt=Qt ∗(Omt^ −1);
    At=eye (2)+(Vh^ −1)∗Vt ;
    Bt=eye (2) −(Vh^ −1)∗Vt ;


    St11=Bt ∗(At^ −1);
    St12 =0.5 ∗ eye (2) ∗( At −(Bt ∗(At^ −1)∗Bt ) ) ;
    St21 =2 ∗(At^ −1);
    St22=−(At^ −1)∗Bt ;
```

% updating global scattering matrices by Redheffer star product

```
    SA11=Sg11;
    SA12=Sg12;
    SA21=Sg21;
    SA22=Sg22;


    SB11=St11;
    SB12=St12;
    SB21=St21;
    SB22=St22;


    SAB11=SA11+(SA12*((eye(2)-(SB11*SA22))^-1)*SB11*SA21);
    SAB12=SA12*((eye(2)-(SB11*SA22))^-1)*SB12;
    SAB21=SB21*((eye(2)-(SA22*SB11))^-1)*SA21;
    SAB22=SB22+(SB21*((eye(2)-(SA22*SB11))^-1)*SA22*SB12);


    Sf11=SAB11;
    Sf12=SAB12;
    Sf21=SAB21;
    Sf22=SAB22;




    Kinc=k0*ni*[sin(theta)*cos(phi) sin(theta)*sin(phi) cos(theta)];
    nsn=[0 0 -1]; % surface normal
```

```
if  (theta ==0)
    aTE=[0  1  0];
else
    aTE=cross(Kinc,nsn)./norm(cross(Kinc,nsn));
end


aTM=cross(aTE,Kinc)./norm(cross(aTE,Kinc));


P=pte*aTE+ptm*aTM;


cinc=[P(1);  P(2)];
Er=Sf11*cinc;
Et=Sf21*cinc;
Erx=Er(1);
Ery=Er(2);
Etx=Et(1);
Ety=Et(2);


Erz=-(Kx*Erx+Ky*Ery)/Krz;
Etz=-(Kx*Etx+Ky*Ety)/Ktz;


Er=[Erx;Ery;Erz];
Et=[Etx;Ety;Etz];


R=abs(Erx)^2+abs(Ery)^2+abs(Erz)^2;
T=(abs(Etx)^2+abs(Ety)^2+abs(Etz)^2)*real((ur1*Ktz)/(ur2*Krz));
```

```
    Tx(Y,N/2)=abs(T);
    Rx(Y,N/2)=abs(R);


    end


proval  = N/2;
prova2  = N/2;
hold  all


figure(1)
plot  (Theta,Tx(:,N/2),  'DisplayName',  ['bilayer −'  num2str(proval)])


xlabel('Angle(degrees)','fontsize',20)
ylabel('Transmittance','fontsize',20)


hold  all


figure(2)
plot(Theta,Rx(:,N/2),  'DisplayName',  ['bilayer −'  num2str(prova2)])
xlabel('Angle(degrees)','fontsize',20)
ylabel('Reflectance','fontsize',20)


end
%——————————————————————————
legend  show
```

```matlab
%% ——————— Plots ———————

fh1 = figure(1);
set(fh1, 'color', 'white');
fh2 = figure(2);
set(fh2, 'color', 'white');
%————————————————————
```

Bibliography

[1]   V. G. Veselago. "The Electrodynamics of Substances with Simultaneously Negative Values of Eps and Mu". In: *Sov. Phys. Usp.* 10 (1968), p. 509.

[2]   D. R. Smith, D. Schurig, and P. Kolinko. "Negative refraction in indefinite media". In: *J. Opt. Soc. Am. B* 21 (2004), p. 1032.

[3]   J. Yao et al. "Optical Negative Refraction in Bulk Metamaterials of Nanowires". In: *Science* (2008).

[4]   A.ee Veltri. "Designs for Electromagnetic Cloaking a Three-Dimensional Arbitrary Shaped Star-Domain". In: *Opt.Express* 17 (2009), pp. 20494–20501.

[5]   S. Xi et al. "Experimental Verification of Reversed Cherenkov Radiation in Left-Handed Metamaterial". In: *Physical Review Letters* 103 (2009).

[6]   Na Liu et al. "Three-dimensional photonic metamaterials at optical frequencies". In: *Nat Mater* 7.1 (Jan. 2008), pp. 31–37.

[7]   J. B. Pendry. "Negative Refraction Makes a Perfect Lens". In: *Phys. Rev. Lett.* 85 (2000), pp. 3966–3969.

[8]   R. A. Shelby, D. R. Smith, and S. Schultz. "Experimental Verification of a Negative Index of Refraction". In: *Science* 292.5514 (2001), pp. 77–79.

[9]   Shumin Xiao et al. "Loss-free and active optical negative-index metamaterials". In: *Nature* 466.7307 (Aug. 2010), pp. 735–738.

[10]   Jason Valentine et al. "Three-dimensional optical metamaterial with a negative refractive index". In: *Nature* 455.7211 (Sept. 2008), pp. 376–379.

[11] Lukas Novotny and Niek van Hulst. "Antennas for light". In: *Nat Photon* 5.2 (Feb. 2011), pp. 83–90.

[12] W. Cai et al. "Optical Cloaking with Metamaterials". In: *Nature Photon.* 1 (2007), pp. 224–227.

[13] Dylan Lu and Zhaowei Liu. "Hyperlenses and Metalenses for Far-Field Super-Resolution Imaging". In: *Nat Commun* 3 (Nov. 2012), pp. 1205–.

[14] Mathieu L Juan, Maurizio Righini, and Romain Quidant. "Plasmon nano-optical tweezers". In: *Nat Photon* 5.6 (June 2011), pp. 349–356.

[15] Zhaowei Liu et al. "Far-Field Optical Hyperlens Magnifying Sub-Diffraction-Limited Objects". In: *Science* 315.5819 (2007), p. 1686.

[16] Alexander Poddubny et al. "Hyperbolic Metamaterials". In: *Nat Photon* 7.12 (2013), pp. 948–957.

[17] Andrea Alù et al. "Epsilon-near-zero metamaterials and electromagnetic sources: Tailoring the radiation phase pattern". In: *Phys. Rev. B* 75 (15 2007), p. 155410.

[18] Prashant Shekhar, Jonathan Atkinson, and Zubin Jacob. "Hyperbolic Metamaterials: Fundamentals and Applications". English. In: *Nano Convergence* 1.1, 14 (2014).

[19] A. J. Hoffman et al. "Negative refraction in semiconductor metamaterials". In: *Nature Materials* 6 (2007), pp. 946–950.

[20] Mário G. Silveirinha and Nader Engheta. "Transformation electronics: Tailoring the effective mass of electrons". In: *Phys. Rev. B* 86 (16 2012), p. 161104.

[21] R. M. A. Azzam and N. M. Bashara. *Ellipsometry and Polarized Light*. Elsevier Science Pub Co, 1987.

[22] Ward D. Newman et al. "Ferrell-Berreman Modes in Plasmonic Epsilon-near-Zero Media". In: *ACS Photonics* 2.1 (2015), pp. 2–7.

[23] Andrey S. Potemkin et al. "Green Function for Hyperbolic Media". In: *Phys. Rev. A* 86 (2 2012), p. 023848.

[24] Domenico de Ceglia et al. "Second-harmonic double-resonance cones in dispersive hyperbolic metamaterials". In: *Phys. Rev. B* 89 (7 2014), p. 075123.

[25] Huikan Liu and Kevin J. Webb. "Resonance cones in cylindrically anisotropic metamaterials: a Green's function analysis". In: *Opt. Lett.* 36.3 (2011), pp. 379–381.

[26] X. Ni et al. "Effect of metallic and hyperbolic metamaterial surfaces on electric and magnetic dipole emission transitions". English. In: *Applied Physics B* 103.3 (2011), pp. 553–558.

[27] Satoshi Ishii et al. "Sub-wavelength interference pattern from volume plasmon polaritons in a hyperbolic medium". In: *Laser & Photonics Reviews* 7.2 (2013), pp. 265–271.

[28] Pavel A. Belov and Yang Hao. "Subwavelength Imaging at Optical Frequencies Using a Transmission Device Formed by a Periodic Layered Metal-Dielectric Structure Operating in the Canalization Regime". In: *Phys. Rev. B* 73 (11 2006), p. 113110.

[29] R.B. Nielsen et al. "Toward superlensing with metal-dielectric composites andămultilayers". In: *Applied Physics B* 100.1 (2010).

[30] S. Anantha Ramakrishna et al. "Imaging the Near Field". In: *Journal of Modern Optics* 50.9 (2003), pp. 1419–1430.

[31] K. V. Sreekanth, A. De Luca, and G. Strangi. "Experimental Demonstration of Surface and Bulk Plasmon Polaritons in Hypergratings". In: *Scientific Reports* 3 (2013), p. 3291.

[32] C. L. Cortes et al. "Quantum nanophotonics using hyperbolic metamaterials". In: *Journal of Optics* 14 (2012), p. 063001.

[33] W. Cai and V. Shalaev. *Optical Metamaterials: Fundamentals and Applications*. Ed. by Springer. Springer, 2009.

[34] K V Sreekanth, A De Luca, and G Strangi. "Excitation of volume plasmon polaritons in metal-dielectric metamaterials using 1D and 2D diffraction gratings". In: *Journal of Optics* 16.10 (2014), p. 105103.

[35] H. N. S. Krishnamoorthy et al. "Topological transitions in metamaterials". In: *Science* 336 (2012), pp. 205–209.

[36] Mohamed A. K. Othman, Caner Guclu, and Filippo Capolino. "Graphene-based tunable hyperbolic metamaterials and enhanced near-field absorption". In: *Opt. Express* 21.6 (2013), pp. 7614–7632.

[37] Nader Engheta. "Pursuing Near-Zero Response". In: *Science* 340.6130 (2013), pp. 286–287.

[38] Mário Silveirinha and Nader Engheta. "Tunneling of Electromagnetic Energy through Subwavelength Channels and Bends using ε-Near-Zero Materials". In: *Phys. Rev. Lett.* 97 (15 2006), p. 157403.

[39] Alexandra Boltasseva and Harry A. Atwater. "Low-Loss Plasmonic Metamaterials". In: *Science* 331.6015 (2011), pp. 290–291.

[40] Brian Edwards et al. "Experimental Verification of Epsilon-Near-Zero Metamaterial Coupling and Energy Squeezing Using a Microwave Waveguide". In: *Phys. Rev. Lett.* 100 (3 2008), p. 033903.

[41] Justus C. Ndukaife, Vladimir M. Shalaev, and Alexandra Boltasseva. "Plasmonics—turning loss into gain". In: *Science* 351.6271 (2016), pp. 334–335.

[42] Alexandra Boltasseva and Vladimir M. Shalaev. "All that glitters need not be gold". In: *Science* 347.6228 (2015), pp. 1308–1310.

[43] Ivan Avrutsky et al. "Highly confined optical modes in nanoscale metal-dielectric multilayers". In: *Phys. Rev. B* 75 (24 2007), p. 241402.

[44] Kandammathe Valiyaveedu Sreekanth et al. "Large Spontaneous Emission Rate Enhancement in Grating Coupled Hyperbolic Metamaterials". In: *Sci. Rep.* 4 (Sept. 2014), pp. –.

[45] V. Caligiuri et al. "Dielectric Singularity in Hyperbolic Metamaterials: the Inversion Point of Coexisting Anisotropies". In: *Scientific Reports* (2016).

[46] Vincenzo Caligiuri et al. "Resonant Gain Singularities in 1D and 3D Metal/Dielectric Multilayered Nanostructures". In: *ACS Nano* 11.1 (2017). PMID: 28009498, pp. 1012–1025.

[47] N. M. Lawandy. "Localized Surface Plasmon Singularities in Amplifying Media". In: *Appl. Phys. Lett.* 85 (2004), pp. 5040–5042.

[48] A. Veltri and A. Aradian. "Optical Response of a Metallic Nanoparticle Immersed in a Medium with Optical Gain." In: *Phys. Rev. B* 85 (2012), pp. 1–5.

[49] A. Veltri, A. Aradian, and A. Chipouline. "Multipolar, Time-Dynamical Model for the Loss Compensation and Lasing of a Spherical Plasmonic Nanoparticle Spaser Immersed in an Active Gain Medium". In: *Scientific Reports* 6.September (2016), p. 33018.

[50] D. J. Bergman and M. I. Stockman. "Surface Plasmon Amplification by Stimulated Emission of Radiation: Quantum Generation of Coherent Surface Plasmons in Nanosystems". In: *Phys. Rev. Lett.* 90 (2003), p. 027402.

[51] M.I. Stockman. "Spasers Explained". In: *Nature Photon.* 2 (2008), pp. 327–329.

[52] M. C. Gather et al. "Net Optical Gain in a Plasmonic Waveguide Embedded in a Fluorescent Polymer". In: *Nat. Photonics* 4 (2010), pp. 457 –461.

[53] G. Strangi et al. "Gain Induced Optical Transparency in Metamaterials". In: *Appl. Phys. Lett.* 98 (2011), p. 251912.

[54] A. De Luca et al. "Dispersed and Encapsulated Gain Medium in Plasmonic Nanoparticles: a Multipronged Approach to Mitigate Optical Losses". In: *ACSNano* 5 (2011), pp. 5823–5829.

[55] Ciceron Ayala-Orozco et al. "Au Nanomatryoshkas as Efficient Near-Infrared Photothermal Transducers for Cancer Treatment: Benchmarking Against Nanoshells". In: *ACS nano* 8.6 (2014), pp. 6372–6381.

[56] Ciceron Ayala-Orozco et al. "Sub-100nm Gold Nanomatryoshkas Improve Photo-Thermal Therapy Efficacy in Large and Highly Aggressive Triple Negative Breast Tumors". In: *Journal of Controlled Release* 191 (2014), pp. 90–97.

[57] Rajib Ghosh Chaudhuri and Santanu Paria. "Core/Shell Nanoparticles: Classes, Properties, Synthesis Mechanisms, Characterization, and Applications". In: *Chemical reviews* 112.4 (2011), pp. 2373–2433.

[58] Ciceron Ayala-Orozco et al. "Fluorescence Enhancement of Molecules Inside a Gold Nanomatryoshka". In: *Nano letters* 14.5 (2014), pp. 2926–2933.

[59] Li Lin, Hongchen Gu, and Jian Ye. "Plasmonic Multi-Shell Nanomatryoshka Particles as Highly Tunable SERS Tags with Built-in Reporters". In: *Chemical Communications* 51.100 (2015), pp. 17740–17743.

[60] Xingjie Ni et al. "Loss-Compensated and Active Hyperbolic Metamaterials". In: *Opt. Express* 19.25 (2011), pp. 25242–25254.

[61] K. H. Krishna, K. V. Sreekanth, and G. Strangi. "Dye-Embedded and Nanopatterned Hyperbolic Metamaterials for Spontaneous Emission Rate Enhancement". In: *J. Opt. Soc. Am. B* 33.6 (2016), pp. 1038–1043.

[62] Sebastian Wuestner et al. "Overcoming Losses with Gain in a Negative Refractive Index Metamaterial". In: *Phys. Rev. Lett.* 105 (12 2010), p. 127401.

[63] Salvatore Campione, Matteo Albani, and Filippo Capolino. "Complex Modes and Near-Zero Permittivity in 3D Arrays of Plasmonic Nanoshells: Loss Compensation Using Gain". In: *Opt. Mater. Express* 1.6 (2011), pp. 1077–1089.

[64] A. Guo et al. "Observation of PT-Symmetry Breaking in Complex Optical Potentials". In: *Phys. Rev. Lett.* 103 (9 2009), p. 093902.

[65] Ali Mostafazadeh. "Spectral Singularities of Complex Scattering Potentials and Infinite Reflection and Transmission Coefficients at Real Energies". In: *Phys. Rev. Lett.* 102 (22 2009), p. 220402.

[66] M. Wimmer et al. "Observation of Optical Solitons in PT-Symmetric Lattices". In: *Nature Communications* (2014).

[67] Stefano Longhi. "$\mathscr{PT}$-Symmetric Laser Absorber". In: *Phys. Rev. A* 82 (3 2010), p. 031801.

[68] K. G. Makris et al. "Beam Dynamics in PT-Symmetric Optical Lattices". In: *Phys. Rev. Lett.* 100 (10 2008), p. 103904.

[69] Shachar Klaiman, Uwe Günther, and Nimrod Moiseyev. "Visualization of Branch Points in PT-Symmetry-Symmetric Waveguides". In: *Phys. Rev. Lett.* 101 (8 2008), p. 080402.

[70] Christian E. Rüter et al. "Observation of Parity-Time Symmetry in Optics". In: *Nat Phys* 6.3 (Mar. 2010), pp. 192–195.

[71] Alois Regensburger et al. "Parity-time Synthetic Photonic Lattices". In: *Nature* 488.7410 (Aug. 2012), pp. 167–171.

[72] S. Anantha Ramakrishna et al. "Imaging the near field". In: *J. Mod. Opt.* 50.9 (2003), pp. 1419–1430.

[73] Giuseppe Castaldi et al. "PT Metamaterials via Complex Coordinate Transformation Optics". In: *Phys. Rev. Lett.* 110 (17 2013), p. 173901.

[74] E. Prodan et al. "A Hybridization Model for the Plasmon Response of Complex Structures". In: *Science* 302 (2003), pp. 419–422.

[75] D J Bergman. "The Dielectric Constant of a Simple Cubic Array of Identical Spheres". In: *Journal of Physics C: Solid State Physics* 12.22 (1979), p. 4947.

[76] Xiang Meng et al. "Engineering Metal-Nanoantennae/Dye Complexes for Maximum Fluorescence Enhancement". In: *Optics express* 22.18 (2014), pp. 22018–22030.

[77] Anika Kinkhabwala et al. "Large Single-Molecule Fluorescence Enhancements Produced by a Bowtie Nanoantenna". In: *Nature Photonics* 3.11 (2009), pp. 654–657.

[78] Vincenzo Giannini et al. "Plasmonic Nanoantennas: Fundamentals and their Use in Controlling the Radiative Properties of Nanoemitters". In: *Chemical reviews* 111.6 (2011), pp. 3888–3912.

[79] Reuben M Bakker et al. "Enhanced Localized Fluorescence in Plasmonic Nanoantennae". In: *Applied Physics Letters* 92.4 (2008), p. 043101.

[80] M. A. Noginov et al. "Demonstration of a Spaser-Based Nanolaser". In: *Nature* 460 (2009), pp. 1110–1113.

[81] B. Peng et al. "Fluorophore-Doped Core-Multishell Spherical Plasmonic Nanocavities: Resonant Energy Transfer toward a Loss Compensation". In: *ACS Nano* 6 (7) (2012), pp. 6250–6259.

[82] Michael Quinten. *Optical Properties of Nanoparticle Systems: Mie and Beyond*. John Wiley & Sons, 2010.

[83] Ying Hu, Ryan C Fleming, and Rebekah A Drezek. "Optical Properties of Gold-Silica-Gold Multilayer Nanoshells". In: *Optics express* 16.24 (2008), pp. 19579–19591.

[84] HY Chung et al. "Accurate Description of the Optical Response of a Multilayered Spherical System in the Long Wavelength Approximation". In: *Physical Review B* 82.16 (2010), p. 165440.

[85] Li Lin et al. "Nanooptics of Plasmonic Nanomatryoshkas: Shrinking the Size of a Core-Shell Junction to Subnanometer". In: *Nano letters* 15.10 (2015), pp. 6419–6428.

[86] A. E. Siegman. *Lasers*. Ed. by University Science Books. 1986.

[87]   A. De Luca et al. "Gain Functionalized Core-Shell Nanoparticles: the Way to Selectively Compensate Absorptive Losses". In: *J. Mater. Chem.* 22 (2012), pp. 8846–8852.

[88]   Melissa Infusino et al. "Loss-Mitigated Collective Resonances in Gain-Assisted Plasmonic Mesocapsules". In: *ACS Photonics* 1.4 (2014), pp. 371–376.

UNIVERSITÀ DELLA CALABRIA

UNIVERSITA' DELLA CALABRIA

Dipartimento di Fisica

Dottorato di Ricerca in

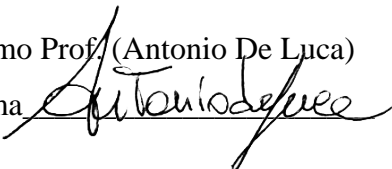SCIENZE E TECNOLOGIE FISICHE, CHIMICHE E DEI MATERIALI

CICLO

XXIX

Dielectric and Resonant Gain Singularities in Multilayered Nanostructures

Settore Scientifico Disciplinare FIS/03 – FIS/07

Coordinatore: Ch.mo Prof. (Vincenzo Carbone)

Firma _____

Supervisore/Tutor: Ch.mo Prof. (Antonio De Luca)

Firma _____

Dottorando: Dott. (Vincenzo Caligiuri)

Firma _____